

PET imaging of PARP expression using ¹⁸F-olaparib

Thomas C. Wilson¹ †, Mary-Ann Xavier² †, James Knight², Stefan Verhoog¹, Julia Baguña Torres², Michael Mosley², Samantha L. Hopkins², Sheena Wallington², Phillip D. Allen², Veerle Kersemans², Rebekka Hueting², Sean Smart², Véronique Gouverneur^{*1}, Bart Cornelissen^{*2}

¹ Department of Chemistry, University of Oxford, Oxford, UK

² CRUK/MRC Oxford Institute for Radiation Oncology, Department of Oncology, University of Oxford, Oxford, UK

† These authors contributed equally to the study

Word count: 3,884

Running title: ¹⁸F-Olaparib PET imaging

Key words: PET, olaparib, PARP, cancer, molecular imaging

Financial Support: This research was supported by Pancreatic Cancer UK, Pancreatic Cancer Research Fund, CRUK through the Oxford Institute for Radiation Oncology and the CRUK Oxford Centre, and the CRUK/EPSRC Imaging Centre in Oxford, the EPSRC (EP/L025604/1, NS/A000024/1) and CRUK (C5255/A16466).

The authors disclose no potential conflicts of interest

1st Author contact details

Thomas C. Wilson, University of Oxford
Department of Chemistry, Chemistry Research Laboratory
12 Mansfield Road,
Oxford OX1 3TA, UK
thomas.wilson@chem.ox.ac.uk

* To whom correspondence should be addressed:

Professor Bart Cornelissen
University of Oxford
CRUK/MRC Oxford Institute for Radiation
Oncology, Department of Oncology
Old Road Campus Research Building
Off Roosevelt Drive
Oxford OX3 7LJ, UK
Tel: +44 (0)1865 857126
bart.cornelissen@oncology.ox.ac.uk

Professor Véronique Gouverneur
University of Oxford

Department of Chemistry
Chemistry Research Laboratory
12 Mansfield Road
Oxford OX1 3TA, UK
Tel: +44 (0) 1865 275644
veronique.gouverneur@chem.ox.ac.uk

Abstract

Poly (ADP-ribose) polymerase (PARP) inhibitors are increasingly being studied as cancer drugs, as single agents or as a part of combination therapies. Imaging of PARP using a radiolabeled inhibitor has been proposed for patient selection, outcome prediction, dose optimization, genotoxic therapy evaluation, and target engagement imaging of novel PARP-targeting agents. Here, *via* the copper-mediated ^{18}F -radiofluorination of aryl boronic esters, we accessed, for the first time, the ^{18}F -radiolabeled isotopologue of the Food and Drug Administration-approved PARP inhibitor olaparib. The use of the ^{18}F -labeled equivalent of olaparib allows direct prediction of the distribution of olaparib, given its exact structural likeness to the native, non-radiolabeled drug. ^{18}F -Olaparib was taken up selectively *in vitro* in PARP-1-expressing cells. Irradiation increased PARP-1 expression and ^{18}F -olaparib uptake in a radiation-dose-dependent fashion. PET imaging in mice showed specific uptake of ^{18}F -olaparib in tumors expressing PARP-1 ($3.2 \pm 0.36\% \text{ID/g}$ in PSN-1 xenografts), correlating linearly with PARP-1 expression. Two hours after irradiation of the tumor (10 Gy), uptake of ^{18}F -olaparib increased by 70% ($P = 0.025$). Taken together, we show that ^{18}F -olaparib has great potential for non-invasive tumor imaging and monitoring of radiation damage.

Immediate Open Access: Creative Commons Attribution 4.0 International License (CC BY) allows users to share and adapt with attribution, excluding materials credited to previous publications.

License: <https://creativecommons.org/licenses/by/4.0/>.

Details: <http://jnm.snmjournals.org/site/misc/permission.xhtml>.



INTRODUCTION

Genomic instability in tumor tissue results from oncogenic and replicative stress, exogenous genotoxic insults, and tumor-specific DNA repair defects (1). Manipulating this genomic instability provides numerous therapeutic opportunities, and inhibitors of DNA damage repair (DDR) enzymes have been explored as anti-cancer drugs (2). This includes inhibitors of Poly(ADP-ribose) Polymerase (PARP). PARP enzymes are part of a 17-member subfamily of enzymes with similar function. PARP-1-3 sense DNA damage by binding to nicked DNA via their zinc-finger domains and play important roles in Base Excision Repair (BER), with PARP-1 being the most studied. PARP inhibitors reduce the enzymes' catalytic activity (formation of poly-ADP-ribose [PAR] chains from NAD⁺) by binding to their NAD⁺ binding pocket and interfere with the ability of the PARP-enzyme-inhibitor complex to dissociate from damaged DNA (3,4). PARP inhibitors have been extensively studied as single agents and as radiation sensitizers, and are especially effective in tumors with BRCA mutations (5). Radiation sensitization using PARP inhibition is known to act via several mechanisms, including straightforward inhibition of DNA repair and synthetic lethality. Further mechanisms include inhibition of chromatin remodelling, vasodilatory effects, decreased hypoxia, contextual lethality in hypoxic cells, replication-dependent radiation sensitization, G2/M arrest leading to time cooperation (6), and a possible role for reduction of Treg cells (7). The first clinically approved and most studied PARP inhibitor is olaparib (ku-0059436, AZ2281, Lynparza®). It inhibits the catalytic activity of PARP isoforms 1 and 2, and, albeit to a lesser extent, PARP-3. At present, over 100 clinical trials are ongoing using olaparib as a single drug, or in combination with other chemotherapy, immunotherapy, or radiation therapies. Other PARP inhibitors in clinical use or clinical trial include the recently approved rucaparib (Clovis), niraparib (Tesaro) and talazoparib (Pfizer), as well as veliparib (AbbVie) (8).

Resistance to PARP inhibition, however, is common. It has been reported that 30-70% of patients with mutations in DDR machinery do not respond to therapies including PARP inhibitors (9). Apart from some molecular mechanisms (10), resistance is often due to low PARP enzyme expression; the inability of the drug to penetrate tumor tissue, or part of the tumor tissue, due to increased interstitial pressure and desmoplasia – especially relevant in pancreatic adenocarcinomas; or an intact blood-brain-barrier, in the case of brain tumors or brain metastases. Increased expression of drug efflux pumps may also prevent drug uptake in the tumor, most relevant for gastro-intestinal and pancreatic tumors (11).

Recently, several reports have suggested that accurately measuring and monitoring PARP expression *in vivo* provides critical information regarding disease prognosis (12), as it has been found to independently correlate with worse outcomes in breast, ovarian, and other tumors (13,14). Assessment of DDR signaling activation may also contribute to genotoxic treatment evaluation, following chemo- or radiotherapy. To date, PARP expression and BRCA-status in tumors can be determined by immunohistochemistry or genetic sequencing on biopsy samples. However, many tumors are known to be extremely heterogeneous – due to their increased genomic instability – yet this heterogeneity is overlooked when sampling tissue from a single biopsy site. Furthermore, acquisition of reliable and high-quality biopsies is a significantly invasive and non-trivial procedure in many disease sites, such as lung, brain, or pancreas.

Given these challenges, scientists have sought to utilize alternative methods to measure PARP expression *in vivo*, especially PARP-1. Of those molecular imaging techniques available, positron emission tomography (PET) has been shown to be ideal. PET allows for non-invasive, whole-body, repeatable visualization of olaparib delivery and its binding to PARP-1-3 (15). In recent years, molecules structurally related to olaparib labeled with positron emitting radionuclides such as ^{18}F or ^{124}I have been investigated for this purpose (see (15,16) for recent reviews). In 2011, Weissleder *et al.*, *via* an inverse electron demand Diels-Alder reaction, reported access to ^{18}F -BO, a molecule which binds PARP, yet deviates significantly from the parent molecule (Fig. 1, compound 2) (17). Subsequently, a range of fluorescently and radiolabeled derivatives have been reported, of which both PARPi-FL and ^{18}F -PARPi have been used to successfully measure uptake and distribution of PARP isoforms *in vivo*, or to perform molecular radionuclide therapy (Fig. 1) (16,18-21).

Alternatively, several radiolabeled compounds have been developed based on analogues of the PARP inhibitor rucaparib. Both radioiodinated (^{123}I , ^{125}I), ^{211}At , and ^{18}F -labeled versions have been described (19,22-24). One of these compounds, ^{18}F -FTT, has been evaluated clinically, demonstrating good correlation between PARP-1 expression and ^{18}F -FTT uptake (25). In 2015, Skydstrup *et al.*, reported an intricate three-component carbonylation of aryl palladium species with the positron emitting isotope carbon-11 in the form of ^{11}C -carbon monoxide (26). This gave the first direct, radiolabeled analogue of olaparib, ^{11}C -olaparib (Fig 1, compound 7). The unstable nature of the palladium precursor however, detracts from what is otherwise an elegant reaction. Moreover, ^{18}F -labeling would allow for a longer shelf life, and results in intrinsically better spatial resolution.

Gouverneur *et al.* have developed a wide range of novel radiofluorination reactions, enabling radiolabeling otherwise challenging motifs (27-29). Most significantly, a Cu-mediated aromatic nucleophilic ^{18}F -fluorination of aryl pinacol-derived boronic esters has enabled access to radioligands difficult to obtain applying alternative methodologies. Indeed, this method facilitated access to an isotopologue, ^{18}F -labeled olaparib itself, from an appropriately protected, bench stable, aryl boronic ester precursor (Fig. 2). Here, we demonstrate that, using ^{18}F -olaparib, measurement of the distribution, uptake, and PARP binding of olaparib using PET imaging in mouse models of pancreatic ductal adenocarcinoma could be achieved. Furthermore, we report the use of ^{18}F -olaparib for detecting DNA damage response following external beam irradiation, and its relationship with tumor hypoxia. To the best of our knowledge, this work represents the first radiosynthesis of ^{18}F -olaparib and its *in vivo* translation for PET imaging.

METHODS

Full materials and methods are presented in the supplementary material accompanying this manuscript.

Synthesis

^{18}F -Olaparib was obtained *via* the Cu-mediated ^{18}F -fluorodeboronation of the corresponding boronic ester precursor (Figs. 1, 2), using methodology previously described by Tredwell *et al.* (27).

In Vitro Methods

PARP-1 levels were determined in a limited selection of cell lines (PSN-1, MiaPaCa-2, and CAPAN-1) using Western blot and confirmed by immunofluorescence microscopy (see supplementary information for full details). STR profiling was used to authenticate all cell lines. CAPAN-1 cells used in this study did not match with the ATCC-held profile. However, low PARP enzyme expression was confirmed by Western blot and immunohistochemistry. Uptake of ^{18}F -olaparib in cells was determined by exposing aliquots of cells growing in 24-well plates to external beam radiation (0-10 Gy; using a ^{137}Cs irradiator (0.8 Gy/min)), letting the cells recover for 2, 24 or 48 h, after which the cells were incubated with ^{18}F -olaparib (50 kBq) for 30 min. Uptake was reported as a percentage of the total amount added, per mg of total protein recovered from the isolated cells, as determined by bicinchoninic acid assay (BCA). Specificity of uptake was determined by blocking olaparib binding sites using an excess of cold, unlabeled olaparib, or other PARP inhibitors (rucaparib, talazoparib; see supplementary information for full details).

In Vivo Methods

All animal procedures were performed in accordance with the UK Animals (Scientific Procedures) Act 1986 and with local ethical committee approval. Tumor xenografts or allografts were generated by subcutaneous injection of PSN-1 or Capan-1 cell suspensions in the hind flank of balb/c nu/nu animals. CaNT xenografts were generated by harvesting CaNT tumors from donor animals, and injecting a tumor homogenate subcutaneously in the flank of wild type CBA/Carl mice. A single tumor was implanted per animal. Tumors were irradiated (10 Gy, 2 Gy/min), or sham-irradiated, using a 300 kV X-ray device.

Dynamic PET images were acquired following an intravenous bolus administration of ^{18}F -olaparib. Biodistribution studies, where selected tissues were harvested, were performed 1 h post injection. Some animals were also administered an excess of cold, unlabeled olaparib for evaluating the specificity of tumor uptake (0.5 mg). EF5, a hypoxia-selective marker, was injected in some of the animals, 2 h before culling. The amount of ^{18}F uptake in selected tissue was determined and reported as a percentage of the injected dose per gram of tissue (%ID/g). Digital autoradiography was performed on tumor sections. PET image analysis was performed using PMOD (see supplementary information for full details).

All statistical analyses and nonlinear regression were performed using GraphPad Prism (GraphPad Software, San Diego, CA, USA). Data were tested for normality and analyzed either by 1-way analysis of variance (ANOVA), with Dunnet's post-tests to calculate significance of differences between groups for multiple comparisons. All data were obtained at least in triplicate and results reported as mean \pm standard deviation, unless indicated otherwise.

RESULTS

^{18}F -Olaparib Synthesis via Copper-mediated ^{18}F -Fluorodeboronylation of Aryl Pinacol Boronic Esters

^{18}F -Olaparib was prepared *via* copper-mediated ^{18}F -fluorodeboronation of a protected boronic pinacol ester precursor (Fig. 2, Supplemental Fig. 1) in an activity yield of $18\% \pm 3\%$ (non-decay corrected

radiochemical yield, $n = 5$, synthesis time = 135 min) with molar activities up to 25.7 GBq/ μ mol (27). In the case of ^{18}F -olaparib, additive preliminary screening experiments suggested that an unprotected boronic ester would be incompatible with the ^{18}F -fluorodeboronation (see Supplemental Figs. 1, 2), potentially due to interference of the phthalazone nitrogen with the Cu-complex catalyst (30). Protected boronic ester substrates bearing *N*-methyl or *N*-[2-(trimethylsilyl)ethoxy]methyl (SEM) protection, respectively, underwent successful ^{18}F -fluorodeboronation, as predicted by screening experiments (Supplemental Figs 3-5). The optimal catalyst for ^{18}F -fluorodeboronation of this substrate, out of those tested, was shown to be $\text{Cu}(\text{OTf})_2(\text{impy})_4$ (impy = imidazo[1,2-*b*]pyridazine), while the use of 1,3-dimethyl-2-imidazolidinone (DMI) proved to be the solvent that led to the most optimal radiochemical yield (Supplemental Figs. 4-7, Supplemental Table 1). Crucially, an unwanted side product due to protodeboronation of the precursor could be separated from the desired product (Supplemental Fig. 5, Supplemental Table 2), thus allowing for isolation of the pure labeled product (Supplemental Figs. 6, 7, Supplemental Table 3).

^{18}F -Olaparib is Taken up in PARP-1-Expressing Cell Lines *In Vitro*

To demonstrate PARP targeting, a set of pancreatic ductal adenocarcinoma cell lines with varying PARP1 expression was exposed to ^{18}F -olaparib *in vitro*. ^{18}F -Olaparib was taken up within 30 min with PSN-1 cells showing the highest uptake (Fig. 3). Results at 60 min after initial exposure of the cells to ^{18}F -olaparib were similar. These results were in concordance to the relative PARP-1 expression levels in these cells as observed by Western blot (Fig. 3B) and immunocytochemistry (Supplemental Fig. 8). Cell-associated uptake of ^{18}F -olaparib in all three cell lines could be blocked near completely (>99%) by addition of a large excess of cold, unlabeled olaparib ($P < 0.0001$), suggesting a highly specific interaction of ^{18}F -olaparib with its binding sites (on PARP-1, -2, and -3), with very little non-specific binding (Fig. 3A, C). In PSN-1 cells, efficient blocking was also achieved using an excess of three NAD^+ -pocket binding PARP inhibitors, olaparib ($\text{IC}_{50} = 20(16-25)$ nM, mean(95%CI)), talazoparib ($\text{IC}_{50} = 5.2(3.2-8.5)$ nM) and rucaparib ($\text{IC}_{50} = 12(8.2-18)$ nM; all $P < 0.001$) (Fig. 3C, Supplemental Fig. 9). Uptake in Capan-1 and MiaPaCa cells was significantly lower compared to PSN-1 cells, consistent with our findings that PARP-1 expression is lower as determined by Western blot and immunofluorescence (Fig. 3B, Supplemental Fig. 8).

^{18}F -Olaparib Shows Hepatobiliary Clearance in Naïve Mice

Biodistribution and kinetics of ^{18}F -olaparib was explored in wild type, tumor-naïve animals. *In vivo* dynamic PET imaging of wild type naïve CBA mice revealed fast pharmacokinetics and a hepatobiliary clearance pattern, following intravenous administration of 3 MBq ^{18}F -olaparib (Fig. 4A). Based on volume-of-interest analysis of ^{18}F signal originating from a region drawn around the heart, the blood clearance of ^{18}F -olaparib followed a biphasic pattern (Supplemental Fig. 10), with fast and slow half-lives of 2.8 min (44%; 95%CI: 2.1-4.0 min) and 32.3 min (56%; 95% CI 27.6-39.1 min), respectively, resulting in a weighted half-life of 19.3 min. Given the very small injected dose of compound (0.0065 mg/kg), the blood half-life of ^{18}F -olaparib was markedly shorter than the previously reported half-life of 58 min (in female mice) after intravenous administration of a bolus of 20 mg/kg of olaparib, but slower than the 5.5 min for an ^{18}F -labeled olaparib-based PARP inhibitor reported by Carney et al. (31). Removal of selected tissues after imaging and measurement of their ^{18}F content confirmed the results obtained though image-based

quantification (Fig. 4B), showing low blood retention and high intestinal uptake of ^{18}F -olaparib at 1 h post injection.

^{18}F -Olaparib is Taken up in PARP-1-Expressing Xenografts *In Vivo*

To study PARP targeting in tumor tissue, subcutaneous tumor-bearing mice were injected intravenously with ^{18}F -olaparib. The biodistribution and clearance pattern in xenograft-bearing animals was similar to that in naïve wild type mice (Fig. 5). Uptake in tissues expressing PARP-1, -2, and -3 such as the spleen, bone, and the pancreas was observed, and this uptake could be blocked by co-injection of an excess of cold, unlabeled olaparib, demonstrating the specificity of PARP-targeting. Uptake of ^{18}F -olaparib in PARP-1 expressing PSN-1 xenografts amounted to $3.16 \pm 0.36\% \text{ID/g}$, measured by biodistribution experiments at 1 h after intravenous bolus injection. This correlated with PARP-1 expression measured by Western Blot and immunohistochemistry (Supplemental Figs. 11, 12). The specificity of this uptake was demonstrated by a significant decrease in tumor uptake following co-injection of an excess of cold, unlabeled olaparib, where uptake dropped to $1.20 \pm 0.17 \% \text{ID/g}$ ($P = 0.0016$). Coronal and transverse sections through the tumor are shown in Supplemental Fig 13. Full details of *ex vivo* biodistribution results are presented in Supplemental Tables 4-7.

In contrast to PSN-1 tumors, Capan-1 xenografts expressed lower levels of PARP-1, as determined by Western blot and immunohistochemistry (Fig. 5D, Supplemental Figs. 11-13). Consistent with lower tumor PARP-1 levels, and consistent with lower *in vitro* uptake of ^{18}F -olaparib, intravenous administration resulted in lower average uptake of ^{18}F -olaparib in these tumors ($2.59 \pm 0.32\% \text{ID/g}$), although this was not statistically significant. Uptake in Capan-1 xenografts could be blocked (to 1.00 ± 0.17 ; $P = 0.015$), indicating specific uptake of the tracer. CaNT tumors, also expressing low amounts of murine PARP-1 (Supplemental Figs. 14, 15) significantly lower uptake of ^{18}F -olaparib compared to PSN-1 xenografts ($1.71 \pm 0.59 \% \text{ID/g}$; $P = 0.03$), and again this uptake could also be blocked by an excess of cold, unlabeled olaparib (to $0.80 \pm 0.19 \% \text{ID/g}$). Overall, correlation between PARP-1 expression, as measured by Western Blot, correlated well with the uptake of ^{18}F -olaparib in xenograft tissues ($R=0.84$, $P<0.0001$, Supplemental Fig. 16).

^{18}F -Olaparib Uptake in PSN-1 Cells and Xenografts Is Increased after External Beam Irradiation

PARP-1 and 2 are essential for proficient base excision repair. In an effort to explore whether ^{18}F -olaparib, which targets PARP, could be used to measure the effects of DNA damaging therapies such as external beam radiotherapy, we irradiated a panel of cell lines, and evaluated PARP-1 expression as well as uptake of ^{18}F -olaparib at several time intervals later. *In vitro*, 2 h after gamma-irradiation (10 Gy) of cells, Western blot analysis revealed an increase in PARP-1 expression in MiaPaCa-2 and PSN-1 cells (Fig. 3B). PARP-1 expression in Capan-1 cells proved low (Fig. 3B), although immunofluorescence microscopy suggested some expression of PARP-1 (Supplemental Fig. 8). In line with these results, ^{18}F -olaparib uptake was increased in all cells after gamma-irradiation, in a radiation dose-dependent manner, which was more pronounced at later times after irradiation, and more pronounced in PSN-1 cells (Fig. 3D).

In vivo, 2 h after irradiation of PSN-1 xenografts (10 Gy), uptake of ^{18}F -olaparib in the tumor tissue was increased by 70%, from 3.16 ± 0.36 to $5.35 \pm 1.16 \% \text{ID/g}$ ($P = 0.025$) (Fig. 5). This result was consistent

with earlier data reported by Kossatz et al. (32), who used a fluorescently labeled version of olaparib, visualized using *in vivo* optical fluorescence imaging, or *ex vivo* confocal microscopy. The increased expression of PARP-1 in PSN-1 xenografts was confirmed *ex vivo* using Western blot (Fig. 5D, Supplemental Fig. 11).

Relationship between Hypoxia and PARP-1 Expression

It is well known that genomic stability in tumor tissue is greatly increased in hypoxic regions (33). In an effort to investigate the relationship between hypoxia and PARP-1 expression *in vivo* in tumor xenografts we compared PARP-1 signal intensity with EF5 staining, which is known to accumulate in regions of clinically relevant hypoxia. A clear correlation between PARP-1 staining and EF5 uptake could be observed in all of the samples (a representative example is shown in Supplemental Fig. 17), both irradiated and non-irradiated. This observation, in combination with the increased delivery of ¹⁸F-olaparib to tumors with increased PARP-1 content suggests that olaparib and other PARP inhibitors will be more effective in hypoxic tumor tissue. This prediction is consistent with previous observations by Jiang et al. who demonstrated contextual synthetic lethality for hypoxia and PARP inhibition, where hypoxic cells and tumors are up to a third more sensitive to PARP inhibition compared to fully oxygenated controls (34).

DISCUSSION

PARP inhibitors are being intensively studied following the elucidation of the role of PARylation enzymes in DNA damage repair, and the identification of the PARP enzyme, now known as PARP-1, (one of 17 in the PARP enzyme superfamily). Clinical trials were set up to study the effects of a wide variety of compounds, including olaparib (AZD2281, KU0059436), rucaparib (AG-014699, PF-01367338), veliparib (ABT-888), niraparib (MK-4827), talazoparib (BMN-673), or CEP-9722, all of which have been designed to compete for binding to the NAD⁺ binding pocket of the PARP enzymes. Most of these inhibitors are selective for PARP-1 and -2, with PARP-3 also being inhibited by some, although to a lesser degree. PARP inhibition is largely successful, especially when used in synthetic lethal combination settings, such as in pre-selected tumors with BRCA-ness signatures (35).

Nonetheless, resistance to PARP inhibitor treatment is common. Aside from some genetic mechanisms, the failure to deliver therapeutically adequate amounts of drug to the tumor tissue has been suggested as a likely cause, especially in brain and pancreatic tumors {Carney, 2018 #16}. It has been argued that this may occur due to: low systemic doses (for example, as a result of poor oral availability); Rapid clearance or metabolism; Non-specific sequestration by non-target organs rapid export by drug transporter – olaparib is known substrate of p-glycoprotein (PGP); Lack of the target enzyme, or mutations in the binding pocket reducing drug affinity (36). For all of these reasons, using a radiolabeled form of the drug will reveal if drug accumulation in the tumor is therapeutically limiting. Imaging of PARP expression using radiolabeled PARP inhibitors, and imaging the delivery of a radiolabeled version of the drug, will assist in identifying those patients that will or will not respond to the treatment.

A variety of radiolabeled PARP inhibitors have been developed in recent years, all based on either olaparib (Reiner et al (17,18,20,31,32), Pimlott et al (37), Skydstrup et al. (26), He et al. (38), this study) or rucaparib-like (Makvandi, Mach et al. (19,23-25)) structures. For an excellent review on the subject, see (16). Some radiolabeled PARP inhibitors are also being studied as radionuclide therapy agents (20). Although a direct comparison between ^{18}F -olaparib (this work) and other radiolabeled PARP imaging agents is hampered by the different model systems that are being used, the main advantage of ^{18}F -olaparib is its relatively high tumor uptake, a good contrast between PARP-expressing tumors and non-expressing tumors, and fast tumor uptake kinetics. One key challenge ^{18}F -olaparib shares with all other radiolabeled PARP inhibitors is its hepatobiliary clearance pattern, making imaging in the mouse abdomen more challenging. In the clinic, this could be averted by PET/CT or PET/MR imaging making localization of lesions more straightforward, especially in ovarian and breast tumors, where PARP inhibitors are primarily used. Being an isotopologue of the unlabeled drug olaparib, ^{18}F -olaparib benefits from a wealth of clinical data already available, which will aid its translation to the clinic. As an exact chemical match of olaparib, ^{18}F -olaparib allows direct imaging of the delivery of olaparib to tumor tissues, and can act as a direct companion imaging biomarker for treatment prediction. The radiofluorination chemistry we have employed here would allow to use a similar strategy on a much larger set of cancer drugs, since it allows radiolabeling of a much larger group of compounds than was previously possible. The use of isotopologues for PET imaging benefits from a large set of structure-activity relationship data and extensive toxicity profiling available through the drug development process. However, it does not necessarily follow that the superior therapeutic agent also makes for a better PET imaging agent, given that an imaging agent should comply with a different set of criteria. The main advantage of an isotopologue is the faster route to clinical translation it may allow, given the reduced need for toxicity data that should be presented to the regulator.

Although PARP-1 is by far the most abundant of the DDR-relevant isoforms of PARP, and a PARP-1-selective imaging agent may predict the outcome of PARP inhibition therapy better,(22) ^{18}F -olaparib olaparib is not selective for one specific isoform. It has previously been well recognized that olaparib affects PARP-1, PARP-2 and PARP-3 alike, albeit with varying effects (IC_{50} of olaparib for PARP-1 and PARP-2 is 5, and 1 nM, respectively). It is also known that replacement of the cyclopropanyl side chain in olaparib with a methoxy-moiety (AZ-2461(39)) significantly reduces its affinity towards PARP-3, and consequently reduces PARP-3 mediated bone marrow toxicity in a murine model. In addition, this compound has been described to have a lower affinity for PGP drug efflux pumps (8). Here, we did not evaluate the influence of PGP pumps for which olaparib, and thus ^{18}F -olaparib, is a known substrate, although one of the cell lines we used here, Capan-1, does express some, as demonstrated by Western blot on whole cell lysates (Supplemental Fig. 18).

Thus, different versions of radiolabeled PARP inhibitors may therefore provide subtly different readouts, and care should be taken in comparing them directly. For example, none of the small molecule inhibitors of PARP described so far uniquely bind to PARP-1 alone. The only imaging agent with this ability is a PARP-1-selective nanobody-RFP fusion protein (40). Its use, however, is limited to transfected cells *in vitro*, as it cannot cross the cell membrane, thus limiting the set of currently available *in vivo* imaging agents for PARP to radiolabeled small molecules.

The use of PARP imaging for evaluating irradiated tissue was first explored by Kossatz et al. using a fluorescently labeled version of olaparib (32). Molecular imaging of the biological effects of radiation therapy holds great promise for precision cancer therapy, and may aid in tailoring radiotherapy dose schedules to the individual tumor's response. Previously, we explored an imaging agent targeting γ H2AX for this purpose, ^{111}In - or ^{89}Zr -labeled anti- γ H2AX-TAT (15,41-43). γ H2AX is a phosphorylated histone expressed around DNA double strand breaks, and has been used extensively as a radiation damage marker. Given the latter imaging agent is based on an antibody, this may make clinical translation more challenging. Therefore, imaging the radiation damage response using radiolabeled PARP inhibitors may offer an alternative, since some are already being evaluated in early phase clinical trials.

We hypothesize that, when translated to the clinic, PET imaging with radiolabelled compounds targeting such as ^{18}F -olaparib will allow: (a) better patient selection, by determining tumor drug uptake; (b) measurement of the biological effects of genotoxic cancer treatment, such as chemo- and radiotherapy; and (c) allow better patient stratification, making the therapeutic use of PARP inhibitors even more effective, albeit in a more stringently selected patient population. One early phase 1 clinical trial using a PARP inhibitor-based imaging agent is already underway (using ^{18}F -FluorThanatrace, www.clinicaltrials.gov), the results of which will undeniably inform the field of future directions.

CONCLUSION

Taken together, we show here that ^{18}F -olaparib can be used for quantifying olaparib tumor accumulation, *in vitro* and *in vivo*. This study serves as an expansion of the evidence base for the use of PARP imaging agents for clinical PET. The use of the ^{18}F -labeled isotopologue of olaparib allows direct prediction of the distribution of olaparib, given its exact structural likeness to the native, non-radiolabeled drug. The translation of this diagnostic strategy to the clinic will significantly improve patient stratification as well as therapy response monitoring.

ACKNOWLEDGEMENTS

V.G. thanks the Royal Society for a Wolfson Research Merit Award. B.C. thanks Cancer Research UK for a Junior Group Leader award.

Competing financial interests.

The work herein is subject to a UK priority patent application.

References

1. Lord CJ, Ashworth A. The DNA damage response and cancer therapy. *Nature*. 2012;481:287-294.
2. O'Connor MJ. Targeting the DNA Damage Response in Cancer. *Mol Cell*. 2015;60:547-560.
3. Murai J, Huang SY, Das BB, et al. Trapping of PARP1 and PARP2 by Clinical PARP Inhibitors. *Cancer Res*. 2012;72:5588-5599.
4. Marchand JR, Carotti A, Passeri D, et al. Investigating the allosteric reverse signalling of PARP inhibitors with microsecond molecular dynamic simulations and fluorescence anisotropy. *Biochim Biophys Acta*. 2014;1844:1765-1772.
5. Lowery MA, Kelsen DP, Stadler ZK, et al. An emerging entity: pancreatic adenocarcinoma associated with a known BRCA mutation: clinical descriptors, treatment implications, and future directions. *Oncologist*. 2011;16:1397-1402.
6. Lesueur P, Chevalier F, Austry JB, et al. Poly-(ADP-ribose)-polymerase inhibitors as radiosensitizers: a systematic review of pre-clinical and clinical human studies. *Oncotarget*. 2017;8:69105-69124.
7. Rosado MM, Bennici E, Novelli F, Pioli C. Beyond DNA repair, the immunological role of PARP-1 and its siblings. *Immunology*. 2013;139:428-437.
8. Lord CJ, Ashworth A. PARP inhibitors: Synthetic lethality in the clinic. *Science*. 2017;355:1152-1158.
9. Livraghi L, Garber JE. PARP inhibitors in the management of breast cancer: current data and future prospects. *BMC Med*. 2015;13:188.
10. Kim Y, Kim A, Sharip A, Jiang J, Yang Q, Xie Y. Reverse the Resistance to PARP Inhibitors. *Int J Biol Sci*. 2017;13:198-208.
11. O'Driscoll L, Walsh N, Larkin A, et al. MDR1/P-glycoprotein and MRP-1 drug efflux pumps in pancreatic carcinoma. *Anticancer Res*. 2007;27:2115-2120.
12. Park SH, Noh SJ, Kim KM, et al. Expression of DNA Damage Response Molecules PARP1, gammaH2AX, BRCA1, and BRCA2 Predicts Poor Survival of Breast Carcinoma Patients. *Transl Oncol*. 2015;8:239-249.

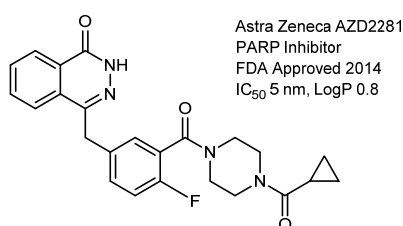
13. Pournazari P, Padmore RF, Kosari F, et al. B-lymphoblastic leukemia/lymphoma: overexpression of nuclear DNA repair protein PARP-1 correlates with antiapoptotic protein Bcl-2 and complex chromosomal abnormalities. *Hum Pathol*. 2014;45:1582-1587.
14. Rojo F, Garcia-Parra J, Zazo S, et al. Nuclear PARP-1 protein overexpression is associated with poor overall survival in early breast cancer. *Ann Oncol*. 2012;23:1156-1164.
15. Knight JC, Koustoulidou S, Cornelissen B. Imaging the DNA damage response with PET and SPECT. *Eur J Nucl Med Mol Imaging*. 2017;44:1065-1078.
16. Carney B, Kossatz S, Reiner T. Molecular Imaging of PARP. *J Nucl Med*. 2017;58:1025-1030.
17. Reiner T, Keliher EJ, Earley S, Marinelli B, Weissleder R. Synthesis and in vivo imaging of a ^{18}F -labeled PARP1 inhibitor using a chemically orthogonal scavenger-assisted high-performance method. *Angew Chem Int Ed Engl*. 2011;50:1922-1925.
18. Carlucci G, Carney B, Brand C, et al. Dual-Modality Optical/PET Imaging of PARP1 in Glioblastoma. *Molecular Imaging and Biology*. 2015;17:848-855.
19. Reilly SW, Makvandi M, Xu K, Mach RH. Rapid Cu-Catalyzed [^{211}At]Astatination and [^{125}I]Iodination of Boronic Esters at Room Temperature. *Org Lett*. 2018.
20. Jannetti SA, Carlucci G, Carney B, et al. PARP1-Targeted Radiotherapy in Mouse Models of Glioblastoma. *J Nucl Med*. 2018.
21. Anderson RC, Makvandi M, Xu K, et al. Iodinated benzimidazole PARP radiotracer for evaluating PARP1/2 expression in vitro and in vivo. *Nucl Med Biol*. 2016;43:752-758.
22. Carlucci G, Carney B, Brand C, et al. Dual-Modality Optical/PET Imaging of PARP1 in Glioblastoma. *Mol Imaging Biol*. 2015;17:848-855.
23. Makvandi M, Xu K, Lieberman BP, et al. A Radiotracer Strategy to Quantify PARP-1 Expression In Vivo Provides a Biomarker That Can Enable Patient Selection for PARP Inhibitor Therapy. *Cancer Res*. 2016;76:4516-4524.
24. Sander Effron S, Makvandi M, Lin L, et al. PARP-1 Expression Quantified by ^{18}F -FluorThanatrace: A Biomarker of Response to PARP Inhibition Adjuvant to Radiation Therapy. *Cancer Biother Radiopharm*. 2017;32:9-15.

25. Makvandi M, Pantel A, Schwartz L, et al. A PET imaging agent for evaluating PARP-1 expression in ovarian cancer. *J Clin Invest*. 2018;128:2116-2126.
26. Andersen TL, Friis SD, Audrain H, Nordeman P, Antoni G, Skrydstrup T. Efficient ^{11}C -carbonylation of isolated aryl palladium complexes for PET: application to challenging radiopharmaceutical synthesis. *J Am Chem Soc*. 2015;137:1548-1555.
27. Tredwell M, Preshlock SM, Taylor NJ, et al. A general copper-mediated nucleophilic ^{18}F fluorination of arenes. *Angew Chem Int Ed Engl*. 2014;53:7751-7755.
28. Preshlock S, Calderwood S, Verhoog S, et al. Enhanced copper-mediated ^{18}F -fluorination of aryl boronic esters provides eight radiotracers for PET applications. *Chem Commun (Camb)*. 2016;52:8361-8364.
29. Preshlock S, Tredwell M, Gouverneur V. ^{18}F -Labeling of Arenes and Heteroarenes for Applications in Positron Emission Tomography. *Chem Rev*. 2016;116:719-766.
30. Taylor NJ, Emer E, Preshlock S, et al. Derisking the Cu-Mediated ^{18}F -Fluorination of Heterocyclic Positron Emission Tomography Radioligands. *J Am Chem Soc*. 2017;139:8267-8276.
31. Carney B, Carlucci G, Salinas B, et al. Non-invasive PET Imaging of PARP1 Expression in Glioblastoma Models. *Mol Imaging Biol*. 2016;18:386-392.
32. Kossatz S, Weber WA, Reiner T. Optical Imaging of PARP1 in Response to Radiation in Oral Squamous Cell Carcinoma. *PLoS One*. 2016;11:e0147752.
33. Bristow RG, Hill RP. Hypoxia and metabolism. Hypoxia, DNA repair and genetic instability. *Nat Rev Cancer*. 2008;8:180-192.
34. Jiang Y, Verbiest T, Devery AM, et al. Hypoxia Potentiates the Radiation-Sensitizing Effect of Olaparib in Human Non-Small Cell Lung Cancer Xenografts by Contextual Synthetic Lethality. *Int J Radiat Oncol Biol Phys*. 2016;95:772-781.
35. Helleday T, Petermann E, Lundin C, Hodgson B, Sharma RA. DNA repair pathways as targets for cancer therapy. *Nat Rev Cancer*. 2008;8:193-204.
36. Thurber GM, Yang KS, Reiner T, et al. Single-cell and subcellular pharmacokinetic imaging allows insight into drug action in vivo. *Nat Commun*. 2013;4:1504.

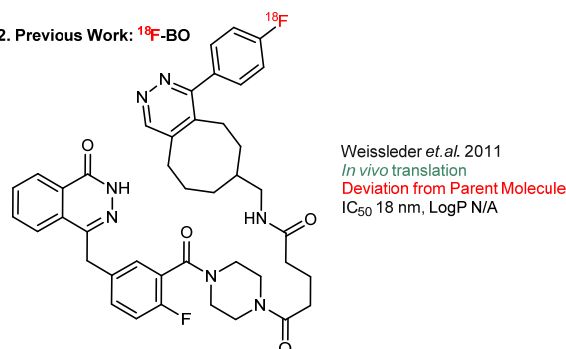
37. Zmuda F, Malviya G, Blair A, et al. Synthesis and Evaluation of a Radioiodinated Tracer with Specificity for Poly(ADP-ribose) Polymerase-1 (PARP-1) in Vivo. *J Med Chem.* 2015;58:8683-8693.
38. Huang T, Hu P, Banizs AB, He J. Initial evaluation of Cu-64 labeled PARPi-DOTA PET imaging in mice with mesothelioma. *Bioorg Med Chem Lett.* 2017;27:3472-3476.
39. Oplustil O'Connor L, Rulten SL, Cranston AN, et al. The PARP Inhibitor AZD2461 Provides Insights into the Role of PARP3 Inhibition for Both Synthetic Lethality and Tolerability with Chemotherapy in Preclinical Models. *Cancer Res.* 2016;76:6084-6094.
40. Buchfellner A, Yurlova L, Nuske S, et al. A New Nanobody-Based Biosensor to Study Endogenous PARP1 In Vitro and in Live Human Cells. *PLoS One.* 2016;11:e0151041.
41. Knight JC, Mosley MJ, Bravo LC, et al. ⁸⁹Zr-anti-gammaH2AX-TAT but not 18F-FDG Allows Early Monitoring of Response to Chemotherapy in a Mouse Model of Pancreatic Ductal Adenocarcinoma. *Clin Cancer Res.* 2017;23:6498-6504.
42. Knight JC, Topping C, Mosley M, et al. PET imaging of DNA damage using ⁸⁹Zr-labelled anti-gammaH2AX-TAT immunoconjugates. *Eur J Nucl Med Mol Imaging.* 2015;42:1707-1717.
43. Cornelissen B, Kersemans V, Darbar S, et al. Imaging DNA damage in vivo using gammaH2AX-targeted immunoconjugates. *Cancer Res.* 2011;71:4539-4549.

Figure 1: Reported olaparib-based radiolabeled PARP imaging and radionuclide therapy agents.

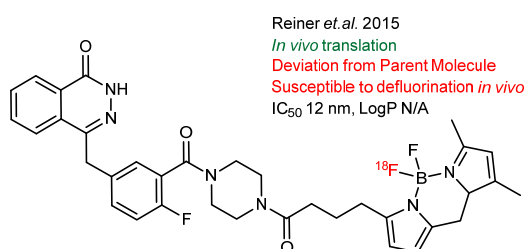
1. Olaparib (Lynparza)



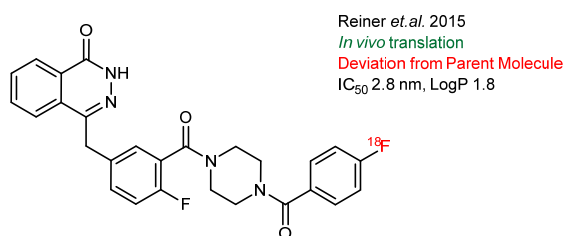
2. Previous Work: ¹⁸F-BO



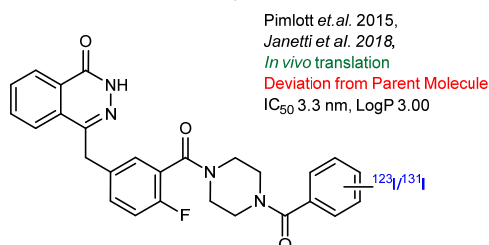
3. Previous Work: ¹⁸F-PARPi-FL



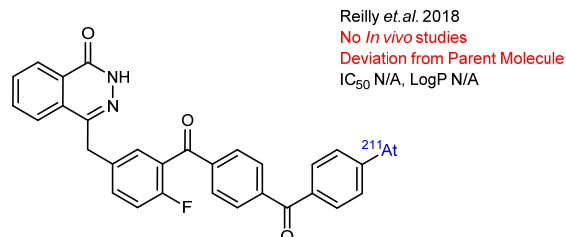
4. Previous Work: ¹⁸F-PARPi



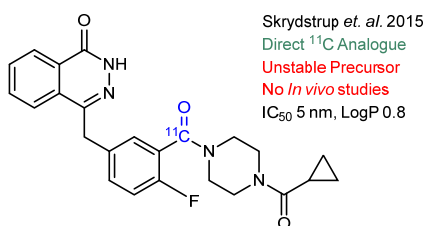
5. Previous Work: ¹²³I-PARPi, ¹³¹I-PARPi



6. Previous Work: ²¹¹At-PARPi



7. Previous Work: ¹¹C-Olaparib



8. This Work: ¹⁸F-Olaparib

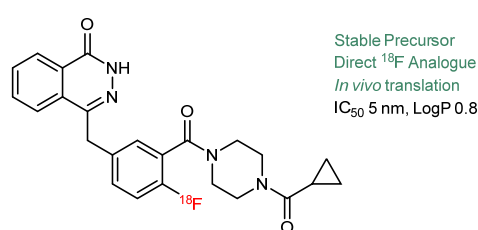


Figure 2: Synthesis of ^{18}F -olaparib from an N-silyl-protected boronic pinacol ester precursor.

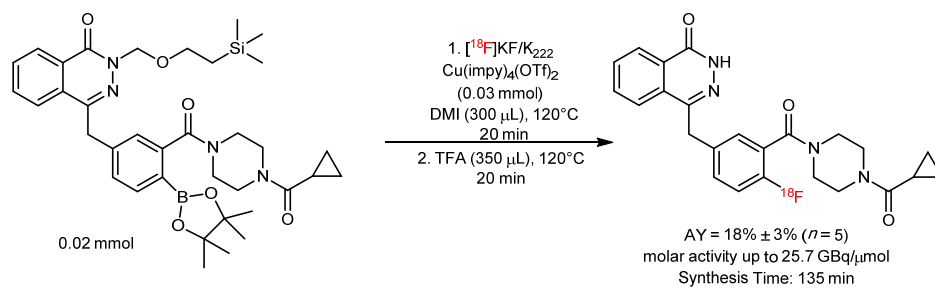


Figure 3: (A) Uptake of ^{18}F in PSN-1, MiaPaCa-2 and Capan-1 cells, 30 min after addition of ^{18}F -olaparib. Uptake can be blocked using an excess of cold, unlabeled olaparib. (B) Western blot probing for PARP-1 in a panel of pancreatic ductal adenocarcinoma cell lines, before, and after 2-48 h of external beam irradiation (10 Gy). (C) Uptake of ^{18}F -olaparib in PSN-1 cells could be blocked by an excess of olaparib, talazoparib, or rucaparib. (D) Uptake of ^{18}F -olaparib in a panel of cell lines, 48 h after external beam irradiation with increasing doses. As a control, uptake of ^{18}F -olaparib irradiated at 10 Gy could additionally be blocked by an excess of cold, unlabeled olaparib.

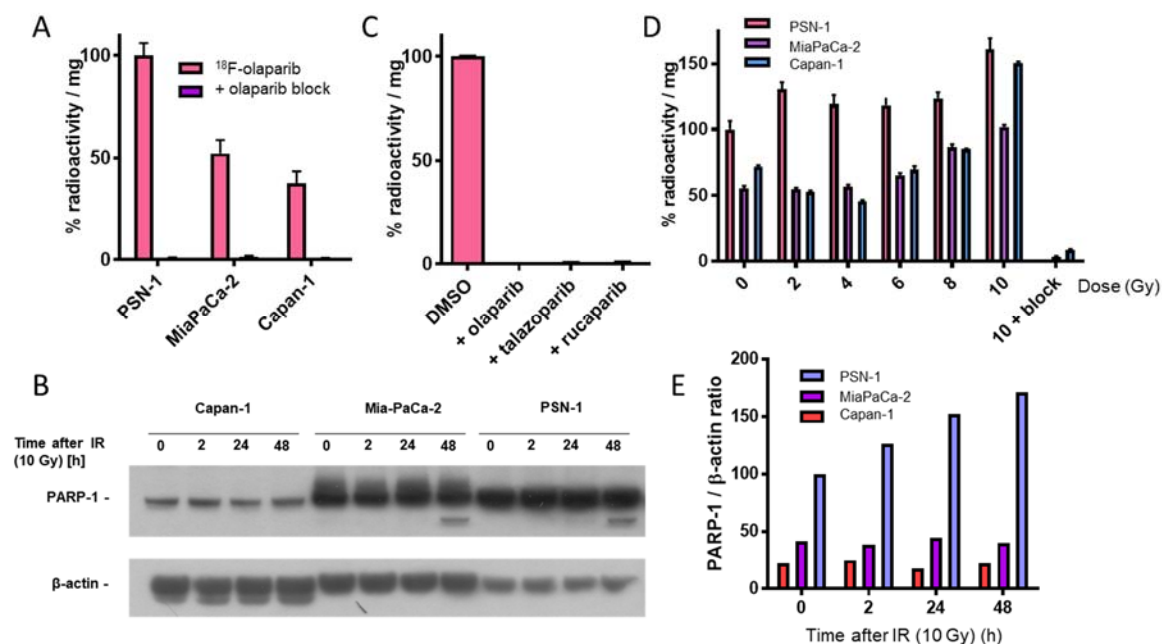


Figure 4: (A) Representative dynamic PET images after an intravenous bolus injection of ^{18}F -olaparib (3 MBq). The middle of the timeframes are indicated in min. Images are presented as MIPs (B) Biodistribution in wild type CBA mice, at 1 h post injection of ^{18}F -olaparib. L: liver, G: gall bladder, I: small intestine, C: caecum.

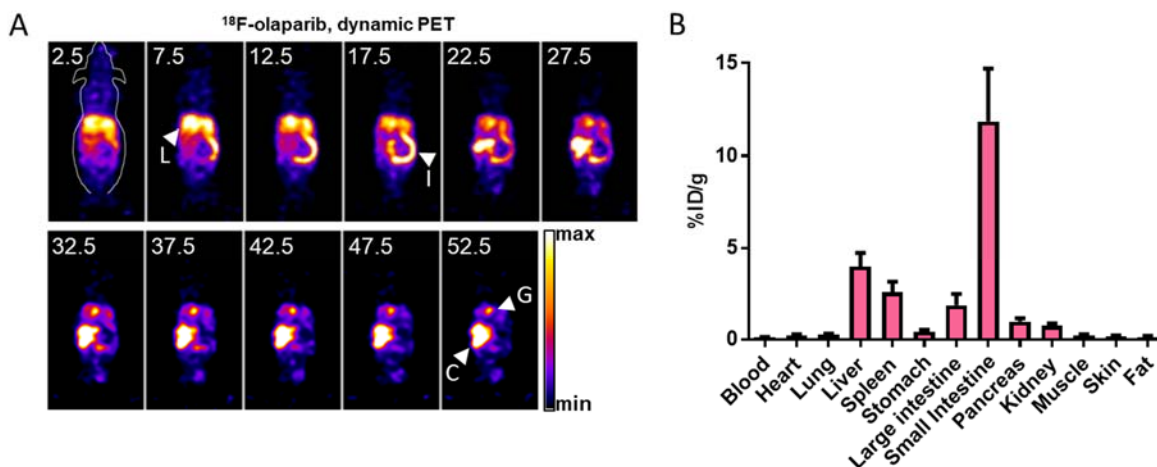
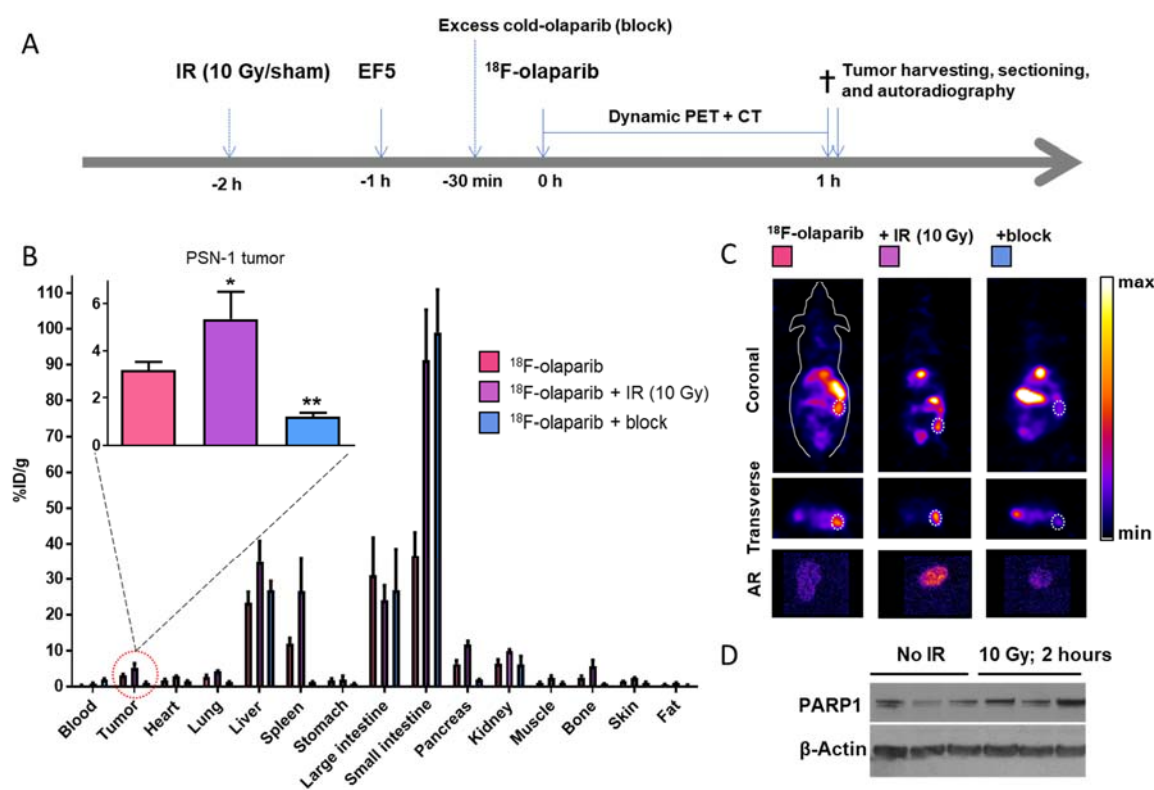


Figure 5: (A) Schematic of the experimental design of imaging experiments. Mice were irradiated or sham irradiated 2 h before injection of ^{18}F -olaparib. (B) Biodistribution in mice bearing PSN-1 xenografts, at 1 h after injection of ^{18}F -olaparib (3 MBq). (C) Representative coronal and transverse images of PSN-1 xenograft-bearing mice, 1 h post injection of ^{18}F -olaparib. Dashed lines indicate the position of the xenograft tumor. Insets represent autoradiograms of tumor sections, corroborating PET imaging results. (D) Western Blot showed increased PARP-1 levels in three irradiated compared to three non-irradiated PSN1-xenografts.



Supplemental information for

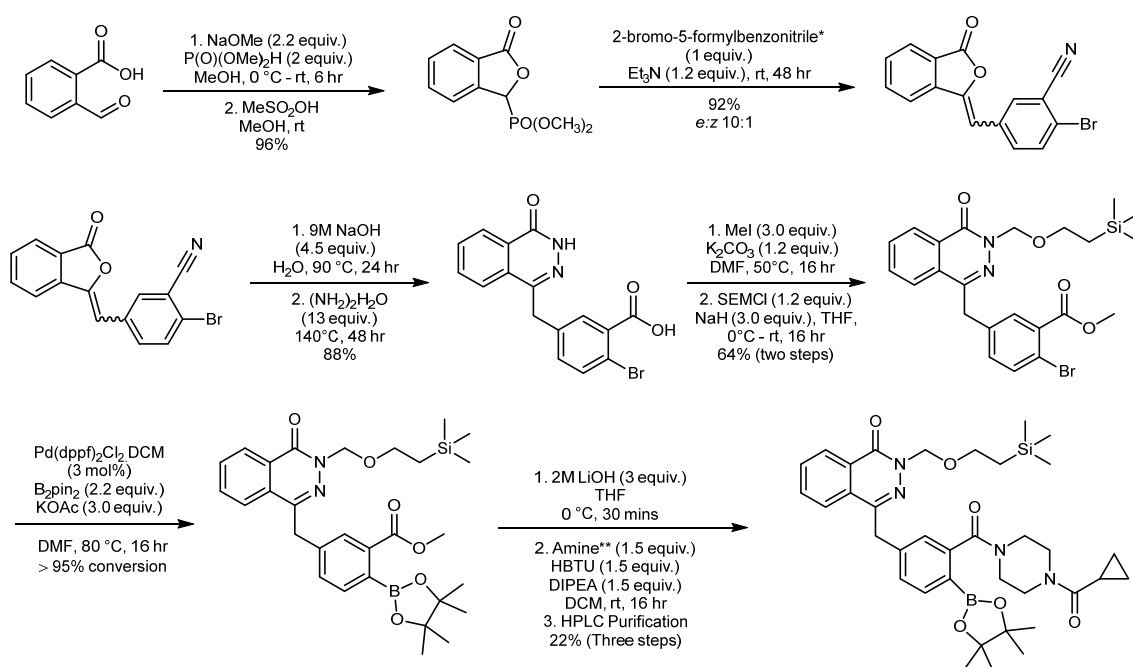
PET imaging of PARP expression using ^{18}F -olaparib

Thomas C. Wilson¹ †, Mary-Ann Xavier² †, James Knight², Stefan Verhoog¹, Julia Baguna-Torres², Michael Mosley², Samantha L. Hopkins², Sheena Wallington², Phillip D Allen², Veerle Kersemans², Rebekka Hueting¹, Sean Smart², Veronique Gouverneur^{*1}, Bart Cornelissen^{*2}

*bart.cornelissen@oncology.ox.ac.uk, veronique.gouverneur@chem.ox.ac.uk

1. Supplemental Material: Chemistry

All chemicals were purchased from Acros, Alfa Aesar, Fluorochem, Sigma-Aldrich and used as received without further purification. Solvents were purchased from Fisher, Rathburn or Sigma-Aldrich. When anhydrous solvents were required they were purified by expression through an activated alumina column built as described by Pangborn and Grubbs (1). Reactions were monitored by thin-layer chromatography (TLC) carried out on Merck Kiesegel 60 F254 plates, silica gel column chromatography was performed over Merck silica gel C60 (40-60 μm). All NMR spectra were recorded on Bruker DPX200, AV400, AVB400, AVC500, AVB500 and DRX500 spectrometers. Proton and carbon-13 NMR spectra are reported as chemical shifts (δ) in parts per million (ppm) relative to the solvent peak using the Bruker internal referencing procedure (edlock). Fluorine-19 NMR spectra are referenced relative to CFCl_3 in CDCl_3 . Coupling constants (J) are reported in units of hertz (Hz). The following abbreviations are used to describe multiplicities – s (singlet), d (doublet), t (triplet), q (quartet), m (multiplet), brs (broad singlet). High resolution mass spectra (HRMS, m/z) were recorded on a Bruker MicroTOF spectrometer using positive electrospray ionization (ESI^+) or on a Micromass GCT spectrometer using field ionization (FI^+) or chemical ionization (CI^+). Infrared spectra were recorded either as the neat compound or in a solution using a Bruker Tensor 27 FT-IR spectrometer. Absorptions are reported in wavenumbers (cm^{-1}) and only peaks of interest are reported. Optical rotations were measured on a PerkinElmer Polarimeter model 341 Specific rotations are reported in $10^{-1} \text{ deg cm}^2 \text{ g}^{-1}$ and concentrations in g/100 mL. Melting points of solids were measured on a Griffin apparatus and are uncorrected. IUPAC names were obtained using the ACD/I-Lab service.

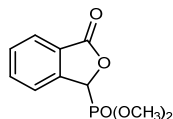


Supplemental Figure 1. Synthesis of 4-(3-(4-(cyclopropanecarbonyl)piperazine-1-carbonyl)-4-(4,4,5,5-tetra methyl-1,3,2-dioxaborolan-2-yl)benzyl)-2-((2-trimethylsilyl)ethoxy)methyl)phthalazin-1(2H)-one. *2-bromo-5-formylbenzonitrile was synthesized over two steps from 2-amino-5-bromobenzo-nitrile *via* formylation/Sandmeyer (46% over two steps), **N-(cyclopropylcarbonyl)piperazine.

1. Synthesis methods

See Supplemental Figure 1 for the full synthesis scheme.

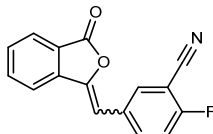
Dimethyl (3-oxo-1,3-dihydroisobenzofuran-1-yl)phosphonate



Dimethylphosphite (0.92 mL, 10.0 mmol) was added dropwise to a solution of sodium (0.58 g, 10.8 mmol) in MeOH (15 mL) at 0°C. To the solution, 2-carboxybenzaldehyde (1.00 g, 6.66 mmol) was added portionwise while stirring. The mixture was gradually warmed to room temperature and stirred for 6 hours. Methanesulfonic acid (0.77 mL, 11.9 mmol) was added dropwise and the mixture was stirred for another 30 minutes. The solution was concentrated in vacuo to produce a white solid, to which water was added (30 mL) and the crude product was extracted into DCM (3 × 30 mL). The organic layer was washed with water (2 × 30 mL), dried with MgSO₄ and filtered. The filtrate was concentrated in vacuo and washed with Et₂O (3 × 20 mL), affording Dimethyl-(3-oxo-1,3-dihydrobenzofuran-1-yl)phosphonate (1.54 g, 96%) as a white solid.

¹H NMR (400 MHz, CD₃OD) δ = 7.94 (d, *J* = 7.5 Hz, 1H), 7.83 (t, *J* = 7.5 Hz, 1H), 7.75 (d, *J* = 7.5 Hz, 1H), 7.68 (t, *J* = 7.5 Hz, 1H), 6.10 (d, *J* = 10.8, 1H), 3.91 (d, *J* = 10.8 Hz, 3H), 3.72 (d, *J* = 10.8 Hz, 3H). Data is in accordance with known literature; **Mp**: 90 - 92°C.(2)

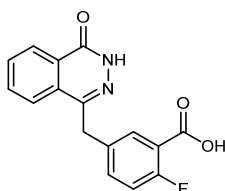
2-Fluoro-5-((3-oxoisobenzofuran-1(3*H*)-ylidene)methyl)benzonitrile



A solution of Dimethyldimethyl-(3-oxo-1,3-dihydrobenzofuran-1-yl)phosphonate (1.00 g, 4.13 mmol) and 2-fluoro-5-formylbenzonitrile (0.62 g, 4.13 mmol) in THF (50 mL) was prepared at room temperature. The solution was then cooled to 0°C followed by the addition of Et₃N (0.69 mL, 4.96 mmol). The reaction mixture was allowed to warm up to room temperature and was stirred for 48 h, followed by concentration in vacuo to produce a white solid. The solid was suspended in water, collected by vacuum filtration and washed with hexane (2 × 20 mL), Et₂O (2 × 20 mL), and MeOH (2 × 20 mL) affording 2-Fluoro-5-((3-oxoisobenzofuran-1(3*H*)-ylidene)methyl)benzonitrile (0.88 g, 80%) as a white solid.

NMR spectra showed a 3:1 mixture of E and Z isomers. Where possible, shifts are assigned to each respective isomer. ¹H NMR (400 MHz, DMSO-d₆) δ = 8.21 – 8.12 (m, 1H), 8.08 (dt, J 8.0, 1.0 Hz, 1H), 8.00 – 7.97 (m, 1H), 7.92 (t, J 7.6 Hz, 1H), 7.75 – 7.67 (m, 1H), 7.65 (t, J 9.0 Hz, 1H), 6.98 (s, 1H); **Mp**: 163 - 165°C. Data is in accordance with known literature.(2)

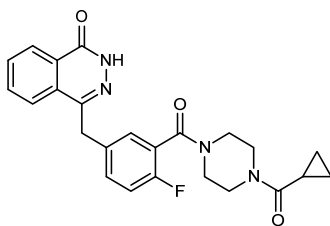
2-Fluoro-5-((4-oxo-3,4-dihydrophthalazin-1-yl)methyl)benzoic acid



2-Fluoro-5-[(3'-oxo-2'- benzofuran-1'-ylidene)methyl]benzonitrile (0.50 g, 1.89 mmol) was suspended in water (3 mL) and 13 M NaOH was added (0.67 mL). The mixture was heated to 90°C and stirred for 24 h, after which it was cooled to 70°C, followed by the addition of hydrazine monohydrate (1.34 mL, 26.9 mmol) and a further 72 h of stirring. The mixture was then cooled to room temperature and acidified with 8 M HCl to an approximate pH of 4. The solid precipitate was collected by vacuum filtration and washed with water (3 × 25 mL) and Et₂O (4 × 25 mL) affording 2-Fluoro-5-((4-oxo-3,4-dihydrophthalazin-1-yl)methyl)benzoic acid (0.38 g, 67%) as a red solid.(2)

¹H NMR (400 MHz, DMSO-d₆) δ = 12.57 (s, 1H), 8.26 (dd, J = 7.8, 0.8 Hz, 1H), 7.98 (d, J = 7.9 Hz, 1H), 7.93 – 7.86 (m, 1H), 7.86 – 7.79 (m, 2H), 7.61 – 7.54 (m, 1H), 7.23 (dd, J 10.8, 8.5 Hz, 1H), 4.35 (s, 2H); {¹H}¹⁹F NMR (376 MHz, DMSO-d₆) δ = -114.0; **Mp**: 217 - 219°C. Data is in accordance with known literature.(2)

4-(3-(4-(cyclopropanecarbonyl)piperazine-1-carbonyl)-4-fluorobenzyl)phthalazin-1(2H)-one (Olaparib)

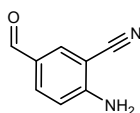


To a solution of 2-Fluoro-5-((4-oxo-3,4-dihydrophthalazin-1-yl)methyl)benzoic acid (50 mg, 0.168 mmol) in DMA (1 mL) was added DIPEA (56 μL, 0.336 mmol) and HBTU (64 mg, 0.170 mmol). The reaction mixture was stirred for 1 hour before addition of cyclopropylpiperazine-1-ylmethanone (0.170 mmol) was carried out. The reaction mixture was stirred at room temperature for 48 h. The reaction mixture was then extracted with DCM (3 × 5 mL) and washed with water (3 × 20 mL). The organic layers were collected,

dried with MgSO_4 and the excess solvent removed *in vacuo*. Purification *via* reverse phase HPLC was carried out affording 4-(3-(4 (cyclopropanecarbonyl) piperazine-1-carbonyl)-4-fluorobenzyl)phthalazin-1(2*H*)-one (olaparib) (25 mg, 34%) as a white solid.

^1H NMR (400 MHz, CDCl_3) δ = 10.65 (s, 1H), 8.44 – 8.37 (m, 1H), 7.75 – 7.61 (m, 3H), 7.34 – 7.22 (m, 2H), 6.97 (t, J = 8.9 Hz, 1H), 4.22 (s, 2H), 3.90 – 3.09 (m, 8H), 1.79 – 1.52 (s, 3H), 0.99 – 0.88 (m, 2H), 0.81 – 0.63 (s, 2H); $\{^1\text{H}\}^{19}\text{F}$ NMR (376 MHz, CDCl_3) δ = - 117.6; **Mp**: 69 - 71°C. Data is in accordance with known literature.(2)

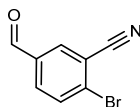
2-Amino-5-formylbenzonitrile



To a flame-dried round bottom flask was added 2-amino-5-bromo-benzonitrile (1.00 g, 5.08 mmol) and THF (30 mL). The solution was cooled to -78°C before *n*-BuLi in THF (2.5 M, 2.23 mL, 5.59 mmol) was added dropwise. The reaction was left to stir at -78°C for 2 h before quenching with DMF (0.55 mL, 7.11 mmol) and allowed to warm to room temperature. The solution was then extracted with NaHCO_3 (40 mL) and washed with DCM (3 x 30 mL). The organic layers were collected, dried with MgSO_4 , and the excess solvent removed *in vacuo*. The crude material was then purified *via* flash column chromatography (*n*-Pent:EtOAc 4:1) affording 2-amino-5-formylbenzonitrile (0.53 g, 71%) as a pale yellow solid.

^1H NMR (400 MHz, CDCl_3) δ = 9.76 (s, 1H), 7.92 (d, J = 1.8 Hz, 1H), 7.87 (dd, J = 8.6, 1.8 Hz, 1H), 6.82 (d, J = 8.6 Hz, 1H), 5.00 (bs, 2H); ^{13}C NMR (101 MHz, CDCl_3) δ = 188.6, 153.7, 136.5, 134.3, 127.4, 116.2, 115.1, 95.9. The data is in accordance with known literature.(3)

2-Bromo-5-formylbenzonitrile

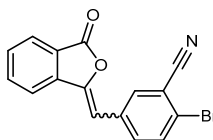


To a round bottom flask containing 2-Amino-5-formylbenzonitrile (17.95 g, 126 mmol) at 0°C was added 6M HCl (107 mL) and fuming H_2SO_4 (107 mL). After being allowed to cool, a solution of sodium nitrite (18.5 g, 268 mmol) in H_2O (40 mL) was added dropwise before allowing the reaction to stir for 30 minutes. The reaction mixture was then added dropwise to a solution of copper(II) bromide (40.1 g, 179 mmol) in 48% HBr (107 mL) at 0°C. The reaction was then stirred at 0°C for 60 min before being allowed to warm to

room temperature and being stirred for another hour. Upon completion, the reaction was poured into an ice/water mixture before the organic layer was extracted with DCM (3 x 150 mL). The organic layer was then dried with MgSO₄ and the excess solvent removed *in vacuo*. The crude material was purified by flash column chromatography (*n*-Pent:EtOAc 10:1) to afford 2-Bromo-5-formylbenzonitrile as a pale yellow solid (16.8 g, 80.6 mmol, 64%).

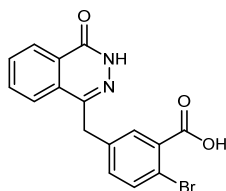
¹H NMR (400 MHz, CDCl₃) δ = 10.00 (s, 1H), 8.14 (s, 1H), 7.95 (d, 8.4, 1H), 7.90 (d, *J* = 8.3 Hz, 1H); ¹³C NMR (101 MHz, CDCl₃) δ = 188.9, 135.4, 135.1, 134.3, 133.7, 131.9, 117.2, 116.1; IR (ν, cm⁻¹): 1702, 1562, 1174, 1008; HRMS (ESI) for C₈H₅⁷⁹BrNO [M+H]⁺ requires 209.9549 found 209.9551; **Mp**: 108 - 110°C.

2-Bromo-5-((3-oxoisobenzofuran-1(3*H*)-ylidene)methyl)benzonitrile



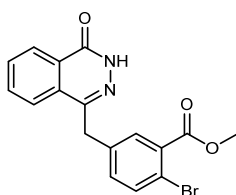
A solution of dimethyl-(3-oxo-1,3-dihydrobenzofuran-1-yl)phosphonate (5.00 g, 20.7 mmol) and 2-bromo-5-formylbenzonitrile (3.58 g, 17.2 mmol) in THF (100 mL) was prepared at room temperature. The solution was cooled to 0°C followed by the addition of Et₃N (4.78 mL, 34.4 mmol). The reaction mixture was warmed to room temperature and was stirred for 48 h, followed by concentration *in vacuo* to produce a white solid. The solid was suspended in water, collected by vacuum filtration and washed with hexane (2 × 20 mL) and Et₂O (3 × 20 mL) affording 2-Bromo-5-((3-oxoisobenzofuran-1(3*H*)-ylidene)methyl)benzonitrile (5.14 g, 15.8 mmol, 92%) as a white solid in an mixture of *e*:*z* stereoisomers (10:1) and a purity of 90%. NMR spectra showed a 10:1 mixture of E and Z isomers.

¹H NMR (400 MHz, DMSO-*d*₆) δ = 8.24 – 8.06 (m, 2H, 2H*), 8.01 – 7.90 (m, 3H, 3H*), 7.83 – 7.50 (m, 2H, 2H*), 7.00 (s, 1H*), 6.97 (s, 1H) (Where possible, shifts are assigned to each respective isomer); ¹³C NMR (100 MHz, DMSO-*d*₆) δ = 166.3, 146.6, 140.0, 135.9, 135.7, 135.4, 134.3, 134.1, 132.0, 131.6, 125.9, 123.9, 121.5, 117.5, 115.5, 103.9 (only those peaks corresponding to the major isomer are reported); IR (ν, cm⁻¹): 2980, 1771, 1472, 1394, 970, 760, 689; HRMS (ESI) for C₁₆H₉⁷⁹BrNO₂ [M+H]⁺ requires 325.9746 found 325.9745; **Mp**: 118 - 120°C.

2-Bromo-5-((4-oxo-3,4-dihydrophthalazin-1-yl)methyl)benzoic acid

2-Bromo-5-[(3'-oxo-2'-benzofuran-1'-ylidene)methyl]benzonitrile (12.0 g, 36.9 mmol) was suspended in water (75 mL) and 13 M NaOH was added (19 mL, 247 mmol). The mixture was heated to 90°C and stirred for 24 h, after which it was warmed to reflux (140°C), followed by the addition of hydrazine monohydrate (25.0 mL, 780 mmol) and a further 48 h of stirring. The mixture was then cooled to room temperature and acidified with 5 M HCl to an approximate pH of 2. The solid precipitate was collected by vacuum filtration and washed with water (50 mL) and Et₂O (3 × 50 mL) affording 2-Bromo-5-((4-oxo-3,4-dihydrophthalazin-1-yl)methyl)benzoic acid (12.27 g, 88%) as a red solid.

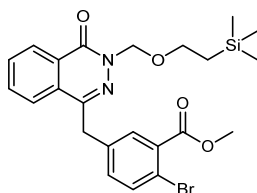
¹H NMR (400 MHz, DMSO-d₆) δ = 12.61 (s, 1H), 8.25 (dd, *J* = 7.7, 1.4 Hz, 1H), 7.99 – 7.94 (m, 1H), 7.89 (ddd, *J* = 8.1, 7.1, 1.5 Hz, 1H), 7.83 (td, *J* = 7.5, 1.2 Hz, 1H), 7.71 (d, *J* = 2.3 Hz, 1H), 7.62 (d, *J* = 8.2 Hz, 1H), 7.36 (dd, *J* = 8.2, 2.3 Hz, 1H), 4.33 (s, 2H); **¹³C NMR** (100 MHz, DMSO-d₆) δ = 167.7, 159.8, 145.2, 138.5, 134.3, 134.1, 133.4, 132.1, 131.4, 129.5, 128.3, 126.5, 125.9, 118.4, 100.0, 36.9; **IR** (ν, cm⁻¹): 2890, 1771, 1472, 1394, 970, 760, 689; **HRMS** (ESI) for C₁₆H₁₀⁷⁹BrN₂O₃ [M-H]⁻ requires 356.9945 found 356.9948; **Mp**: > 250°C.

Methyl-2-bromo-5-((4-oxo-3,4-dihydrophthalazin-1-yl)methyl)benzoate

To a solution of 2-Bromo-5-((4-oxo-3,4-dihydrophthalazin-1-yl)methyl)benzoic acid (12.32 g, 34.4 mmol) in anhydrous DMF (100 mL) was added iodomethane (6.38 mL, 103.2 mmol) and anhydrous potassium carbonate (5.70 g, 41.3 mmol). The reaction was then heated to 50°C and stirred overnight. Upon completion, the excess solvent was removed *in vacuo* and water (100 mL) was added to the crude material. The precipitate formed was filtered and washed with Et₂O (3 × 100 mL) before drying *in vacuo* affording Methyl-2-bromo-5-((4-oxo-3,4-dihydrophthalazin-1-yl)methyl) benzoate as a dull brown solid (11.4 g, 30.6 mmol, 89%).

¹H NMR (400 MHz, DMSO-*d*₆) δ = 12.60 (s, 1H), 7.99 – 7.93 (m, 1H), 7.90 (ddd, *J* = 8.1, 7.1, 1.5 Hz, 1H), 7.83 (ddd, *J* = 8.4, 7.2, 1.3 Hz, 1H), 7.73 (d, *J* = 2.2 Hz, 1H), 7.67 (d, *J* = 8.2 Hz, 1H), 4.35 (s, 2H), 3.83 (s, 3H); **¹³C NMR** (100 MHz, DMSO-*d*₆) δ = 166.6, 159.8, 145.1, 138.6, 134.4, 134.1, 134.0, 132.8, 132.1, 131.6, 129.5, 128.3, 126.5, 125.9, 118.5, 53.1, 36.9; **IR** (ν , cm⁻¹): 2983, 1650, 1250, 1205, 1104, 772; **HRMS** (ESI) for C₁₇H₁₃⁷⁹BrN₂²³NaO₃ [M+Na]⁺ requires 395.0002 found 395.0001; **Mp**: 211 - 213°C.

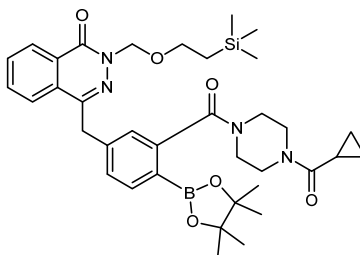
Methyl-2-bromo-5-((4-oxo-((2-(trimethylsilyl)ethoxy)methyl)-3,4-dihydro phthalazin-1-yl)methyl) benzoate



To a round bottom flask under an atmosphere of argon containing Methyl-2-bromo-5-((4-oxo-((2-(trimethylsilyl)ethoxy)methyl)-3,4-dihydro phthalazin-1-yl)methyl) benzoate (11.0 g, 29.6 mmol) at 0°C was added anhydrous THF (200 mL) and sodium hydride (60% in dispersion oil, 3.55 g, 88.8 mmol). The reaction was stirred at 0°C for 30 min before warming to room temperature upon which 2-(trimethylsilyl)ethoxymethyl chloride (6.25 mL, 35.6 mmol) was added dropwise. The reaction was stirred overnight before the excess solvent was removed *in vacuo* and purified directly *via* flash column chromatography (*n*-Pent:EtOAc 10:3) affording Methyl-2-bromo-5-((4-oxo-((2-(trimethylsilyl)ethoxy)methyl)-3,4-dihydro phthalazine-1-yl)methyl)benzoate as a white solid (10.7 g, 72%, 21.3 mmol).

¹H NMR (400 MHz, CDCl₃) δ = 8.52 – 8.45 (m, 1H), 7.77 – 7.68 (m, 3H), 7.66 – 7.58 (m, 1H), 5.58 (s, 2H), 4.28 (s, 2H), 3.91 (s, 3H), 3.79 – 3.73 (m, 2H), 1.02 – 0.97 (m, 2H), 0.01 (s, 9H); **¹³C NMR** (100 MHz, CDCl₃) δ = 167.8, 161.3, 145.7, 138.6, 136.0, 134.9, 133.9, 133.8, 133.0, 132.6, 130.5, 129.8, 129.2, 126.3, 121.3, 80.4, 68.6, 54.0, 39.5, 19.5, 0.00 (3C); **IR** (ν , cm⁻¹): 2952, 1721, 1652, 1431, 1294, 1223, 1074, 1027, 854, 832, 745; **HRMS** (ESI) for C₂₃H₂₇⁷⁹BrN₂²³NaO₄²⁸Si [M+Na]⁺ requires 525.0826 found 525.0827; **Mp**: 85 - 87°C.

4-(3-(4-(cyclopropanecarbonyl)piperazine-1-carbonyl)-4-(4,4,5,5-tetramethyl-1,3,2-dioxaborolan-2-yl)benzyl)-2-((2-trimethylsilyl)ethoxy)methyl)phthalazin-1(2H)-one



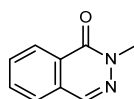
To a Schlenk tube under an atmosphere of argon was added, Methyl-2-bromo-5-((4-oxo-((2-(trimethylsilyl)ethoxy) methyl)-3,4-dihydro phthalazin-1-yl)methyl)benzoate (1.48 g, 2.94 mmol), bis(pinacolato)diboron (1.49 g, 5.89 mmol), Pd(dppf)Cl₂ (72 mg, 0.09 mmol) and potassium acetate (0.87 g, 8.88 mmol). The reaction flask was then backfilled with argon and placed in an oil bath at 90°C upon which degassed DMF (13 mL) was added and the reaction left to stir overnight. Upon completion, the reaction was cooled and passed through a plug of Celite before extracting with EtOAc (100 mL) and washing with Lithium Chloride solution (3 x 50 mL). The organic phases were then collected and the excess solvent was removed *in vacuo*. The crude material was then purified by flash column chromatography (10:3 *n*-Pent: EtOAc) to afford a mixture of Methyl-5-((4-oxo-3-((2-(trimethylsilyl)ethoxy)methyl)-3,4-dihydro phthalazin-1-yl)methyl)-2-(4,4,5,5-tetramethyl-1,3,2-dioxaborolan-2-yl)benzoate and bis(pinacolato)diboron (2.00 g) with the following ¹H NMR spectra being observed. ¹H NMR (400 MHz, CDCl₃) δ = 8.43 (d, *J* = 7.8 Hz, 1H), 7.85 (s, 1H), 7.76 – 7.57 (m, 2H), 7.53 (d, *J* = 8.0 Hz, 1H), 7.38 (s, 2H), 5.58 (s, 2H), 4.32 (s, 2H), 3.86 (s, 3H), 3.76 (t, *J* = 7.3 Hz, 1H), 0.99 (t, *J* = 7.6 Hz, 2H), - 0.03 (s, 9H). Peaks reported only correspond to the product. The crude material was taken forward without further purification.

To a round bottom flask containing Methyl-5-((4-oxo-3-((2-(trimethylsilyl)ethoxy) methyl)-3,4-dihydrophthalazin-1-yl) methyl)-2-(4,4,5,5-tetramethyl-1,3,2-dioxaborolan-2-yl)benzoate and bis(pinacolato) diboron (2.00 g) was added THF (100 mL) before cooling to 0°C. Upon cooling, 2M lithium hydroxide (7 mL, 14 mmol) was added dropwise before allowing to reaction to stir for 30 min at 0°C. 1M HCl was then added dropwise to the reaction mixture at 0°C until reaching pH 4. The mixture was then extracted with EtOAc (3 x 80 mL) and washed with Brine (3 x 50 mL). The organic phases were combined and the excess solvent removed *in vacuo*. The crude material (1.4 g) was transferred to a round bottom flask upon which DCM (100 mL), HBTU (2.97 g, 7.84 mmol) and DIPEA (1.36 mL, 7.84 mmol) was added. After stirring at room temperature for 30 minutes, *N*-cyclopropylcarbonylpiperazine (1.11 mL, 7.85 mmol)

was added and the reaction stirred overnight. After stirring for 16 hours, the excess solvent was removed *in vacuo* and the crude material isolated by flash column chromatography (Pure EtOAc) before purification by reverse phase HPLC was carried out to afford 4-(3-(4-(cyclopropanecarbonyl) piperazine-1-carbonyl)-4-(4,4,5,5-tetramethyl-1,3,2-dioxaborolan-2-yl)benzyl)-2-((2-trimethylsilyl) ethoxy)methyl)phthalazin-1(2*H*)-one (419 mg, 0.62 mmol, 22% - three steps) as a white solid in a mixture of rotamers. In each case the shift relating to the minor rotamer has been denoted with an asterisk.*

¹H NMR (400 MHz, CDCl₃) δ = 8.46 (dd, *J* = 7.8, 1.6 Hz, 1H + 1H*), 7.79 – 7.55 (m, 4H + 4H*), 7.32 – 7.28 (m, 1H + 1H*), 7.14 (bs, 1H + 1H*), 5.59 (s, 2H + 2H*), 4.33 (s, 2H + 2H*), 3.87 – 3.04 (m, 10H + 10H*), 1.28 (s, 12H + 12H*), 1.04 – 0.97 (m, 4H + 4H*), 0.90 – 0.85 (m, 1H + 1H*), 0.83 – 0.71 (m, 2H + 2H*), 0.00 (s, 9H + 9H*); **¹³C NMR** (100 MHz, CDCl₃) δ = 172.3 (1C + 1C*), 171.0 (1C + 1C*), 160.0 (1C + 1C*), 144.7 (1C + 1C*), 142.9 (1C + 1C*), 141.3 (1C + 1C*), 136.3 (1C + 1C*), 133.3 (1C + 1C*), 131.5 (1C + 1C*), 129.2 (1C + 1C*), 128.4 (1C + 1C*), 128.2 (1C + 1C*), 127.7 (1C + 1C*), 125.4 (1C + 1C*), 125.2 (1C + 1C*), 84.1 (2C + 2C*), 79.0 (1C + 1C*), 67.3 (1C + 1C*), 47.3 (1C*), 46.9 (1C), 45.2 (1C*), 44.8 (1C), 41.9 (1C*), 41.7 (2C), 41.4 (1C*), 39.1 (1C + 1C*), 24.9 (4C + 4C*), 18.1 (1C + 1C*), 11.1 (1C + 1C*), 7.66 (2C + 2C*), -1.36 (3C + 3C*) (the carbon bearing the boron substituent is not observed); **IR** (ν , cm⁻¹): 2981, 2889, 2360, 2341, 1641, 1382, 1354, 1146, 1087, 956; **HRMS** (ESI) for C₃₆H₄₉N₄O₆¹⁰B²³Na²⁸Si [M+Na]⁺ requires 694.34429 found 694.34418; **Mp**: 78 - 80°C.

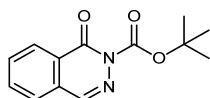
2-Methylphthalazin-1(2*H*)-one



To a round bottom flask containing DMF (10 mL) under an atmosphere of argon was added, phthalazone (300 mg, 2.05 mmol). To solution was then cooled to 0°C before sodium hydride (60% in dispersion oil, 61 mg, 2.53 mmol) was added portion wise. iodomethane (119 μ L, 1.92 mmol). The reaction was stirred overnight before the solvent was removed *in vacuo* and the crude material purified directly *via* flash column chromatography using *n*-pentane: EtOAc (10:1) affording 2-2-Methylphthalazin-1(2*H*)-one as a white solid (210 mg, 1.31 mmol, 64%).

¹H NMR (400 MHz, CDCl₃) δ = 8.42 – 8.38 (m, 1H), 8.12 (s, 1H), 7.81 – 7.70 (m, 2H), 7.69 – 7.65 (m, 1H), 3.83 (s, 3H); **¹³C NMR** (100 MHz, CDCl₃) δ = 159.7, 137.6, 133.0, 131.6, 129.8, 127.8, 126.5, 126.0, 39.5. The data is in accordance with known literature.(4)

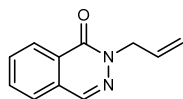
***tert*-Butyl 1-oxophthalazine-2(1*H*)-carboxylate**



To a round bottom flask containing THF (10 mL) under an atmosphere of nitrogen was added, phthalazone (500 mg, 3.41 mmol), di-*tert*-butyl dicarbonate (1.11 g, 5.12 mmol) and DMAP (620 mg, 5.12 mmol). The reaction was stirred overnight at room temperature before the solvent was removed *in vacuo* and the crude material purified directly *via* flash column chromatography using *n*-pentane: EtOAc (5:1) *tert*-Butyl 1-oxophthalazine-2(1*H*)-carboxylate as a white solid (765 mg, 3.11 mmol, 91%).

¹H NMR (400 MHz, CDCl₃) δ = 8.43 (dd, *J* = 7.9, 1.3 Hz, 1H), 7.83 (td, *J* = 7.5, 1.4 Hz, 1H), 7.77 (td, *J* = 7.6, 1.3 Hz, 1H), 7.68 (dd, *J* = 7.5, 1.3 Hz, 1H), 1.66 (s, 9H); **¹³C NMR** (100 MHz, CDCl₃) δ = 158.3, 150.9, 138.9, 134.2, 132.3, 129.2, 128.7, 127.5, 126.4, 85.9, 27.8 (3C); **IR** (ν, cm⁻¹): 2980, 1720, 1641, 1470, 1325, 1130; **HRMS** (ESI) for C₁₃H₁₄N₂O₃ [M+H]⁺ requires 247.1012 found 247.1015; **Mp**: 81 - 83°C.

2-allylphthalazin-1(2*H*)-one

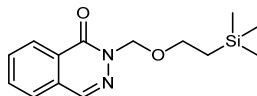


To a round bottom flask containing DMF (30 mL) under an atmosphere of nitrogen was added, phthalazone (500 mg, 3.42 mmol), anhydrous potassium carbonate (708 mg, 5.12 mmol) and allyl bromide (442 μL, 5.12 mmol). The reaction was stirred overnight at room temperature before the solvent was removed *in vacuo* and the crude material purified directly *via* flash column chromatography using *n*-pentane: EtOAc (3:1) affording 2-allylphthalazin-1(2*H*)-one as a brown oil (222 mg, 1.20 mmol, 35%)

¹H NMR (400 MHz, CDCl₃) δ = 8.42 (ddd, *J* = 7.5, 1.7, 0.7 Hz, 1H), 8.17 (d, *J* = 0.8 Hz, 1H), 7.83 – 7.72 (m, 2H), 7.71 – 7.67 (m, 1H), 6.04 (ddt, *J* = 17.2, 10.3, 5.9 Hz, 1H), 5.30 – 5.22 (m, 2H), 4.85 (dt, *J* = 5.9, 1.5 Hz,

2H); ^{13}C NMR (100 MHz, CDCl_3) δ = 159.2, 138.1, 133.1, 132.5, 131.7, 129.7, 128.0, 126.8, 126.0, 118.0, 53.5. Data is in accordance with literature values.⁽⁵⁾

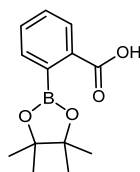
2-((2-triethylsilyl)ethoxymethyl)phthalazin-1(2H)-one



To a round bottom flask containing THF (10 mL) under an atmosphere of argon was added, phthalazone (480 mg, 3.28 mmol). To solution was then cooled to 0°C before sodium hydride (60% in dispersion oil, 97 mg, 4.04 mmol) was added portion wise. The reaction was then stirred for 30 min at 0°C before warming to room temperature after which 2-(trimethylsilyl)ethoxymethyl chloride (0.70 mL, 3.97 mmol) was added dropwise. The reaction mixture was left to stir overnight after which the solvent was removed *in vacuo*. The crude mixture was then extracted with DCM (3 x 10 mL) and washed with brine (3 x 10 mL). The organic layer was collected, dried with magnesium sulfate and the excess solvent removed *in vacuo*. The crude material was then purified by flash column chromatography (2:3 *n*-Pent:EtOAc) to afford 2-((2-triethylsilyl)ethoxymethyl) phthalazin-1(2H)-one as a colorless oil (435 mg, 1.57 mmol, 46%).

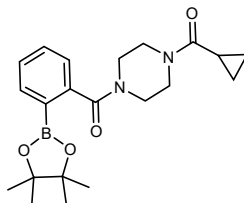
^1H NMR (400 MHz, CDCl_3) δ = 8.41 (d, J = 7.8 Hz, 1H), 8.15 (s, 1H), 7.76 (dt, J = 21.7, 7.6 Hz, 2H), 7.67 (d, J = 7.7 Hz, 1H), 5.55 (s, 2H), 3.74 – 3.68 (m, 2H), 0.99 – 0.92 (m, 2H), - 0.05 (s, 9H); ^{13}C NMR (100 MHz, CDCl_3) δ = 161.4, 139.6, 134.9, 133.2, 131.2, 129.4, 128.4, 127.6, 80.4, 68.5, 19.5, 0.00 (3C); IR (ν , cm^{-1}): 1661, 1081, 833, 758; HRMS (ESI) for $\text{C}_{14}\text{H}_{20}\text{N}_2^{23}\text{NaO}_2^{28}\text{Si}$ [$\text{M}+\text{Na}$] $^+$ requires 299.1186 found 299.1185.

2-(4,4,5,5-Tetramethyl-1,3,2-dioxaborolan-2-yl)benzoic acid



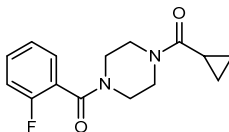
To a solution of anhydrous THF (20 mL) under an atmosphere of argon was added 2-boronobenzoic acid (1.00 g, 6.02 mmol), pinacol (0.71 g, 6.02 mmol) and magnesium sulfate (1.44 g, 12.04 mmol). The reaction was left to stir overnight at room temperature. Upon completion, the reaction was filtered and the excess solvent removed *in vacuo* affording 2-(4,4,5,5-Tetramethyl-1,3,2-dioxaborolan-2-yl)benzoic acid as a white solid (1.49 g, 6.00 mmol, 99%).

¹H NMR (400 MHz, DMSO-d₆) δ = 7.83 (dd, J = 7.6, 0.9 Hz, 1H), 7.55 (td, J = 7.3, 1.3 Hz, 1H), 7.46 (td, J = 7.5, 1.4, 1H), 7.43 – 7.39 (m, 1H), 1.29 (s, 12H); **¹³C NMR** (100 MHz, DMSO-d₆) δ = 169.6, 134.7, 132.2, 131.9, 129.2, 128.3, 83.4 (2C), 25.0 (4C) (the carbon bearing the boron substituent is not observed); **IR** (ν , cm⁻¹): 2972, 1679, 1344, 1304, 1141, 754; **HRMS** (ESI) for C₁₃H₁₆¹⁰BO₄ [M-H]⁻ requires 247.1212 found 247.1215; **Mp**: 118 - 120°C.

(4-(Cyclopropanecarbonyl)piperazin-1-yl)(2-(4,4,5,5-tetramethyl-1,3,2-dioxaborolan-2-yl)phenyl)methanone

To a round bottom flask containing 2-(4,4,5,5-Tetramethyl-1,3,2-dioxaborolan-2-yl)benzoic acid (1.00 g, 4.03 mmol) was added DCM (40 mL), diisopropylethylamine (1.05 mL, 6.04 mmol) and HBTU (2.29 g, 6.04 mmol). The reaction mixture was stirred for 30 min before adding cyclopropylpiperazine-1-ylmethanone (0.86 mL, 6.04 mmol). The reaction was stirred overnight before the excess solvent with removed *in vacuo* and the crude material purified *via* flash column chromatography (EtOAc:MeOH 10:1) affording (4-(Cyclopropanecarbonyl)piperazin-1-yl)(2-(4,4,5,5-tetramethyl-1,3,2-dioxaborolan-2-yl)phenyl)methanone as a white solid (1.08 g, 2.82 mmol, 70%) in a mixture of rotamers (2:1). The shifts relating to the minor rotamer has been donated with an asterisk.*

¹H NMR (400 MHz, CDCl₃) δ = 7.81 (d, J = 7.4 Hz, 1H + 1H*), 7.45 (td, J = 7.6, 1.5 Hz, 1H + 1H*), 7.35 (td, J = 7.5, 1.3 Hz, 1H + 1H*), 7.22 (d, J = 7.5 Hz, 1H + 1H*), 3.86 – 3.69 (m, 4H, 4H*), 3.67 – 3.50 (m, 2H, 2H*), 3.34 – 3.07 (m, 2H, 2H*), 1.81 – 1.52 (m, 1H + 1H*), 1.29 (s, 12H + 12H*), 1.04 – 0.95 (m, 2H + 2H*), 0.67 – 0.87 (m, 2H + 2H*); **¹³C NMR** (100 MHz, CDCl₃) δ = 172.3 (1C + 1C*), 171.3 (1C + 1C*), 142.3 (1C + 1C*), 135.7 (1C + 1C*), 131.2 (1C + 1C*), 128.2 (1C + 1C*), 125.4 (1C + 1C*), 84.1 (2C + 2C*), 47.3 (1C*), 47.0, 45.2 (1C*), 44.9, 41.9 (2C), 41.6 (2C*) 24.9 (4C + 4C*), 11.0 (1C + 1C*), 7.65 (2C + 2C*) (the carbon bearing the boron substituent is not observed); **IR** (ν , cm⁻¹): 2970, 1634, 1467, 1213, 1014, 741; **HRMS** (ESI) for C₂₁H₃₀¹⁰BN₂O₄ [M+H]⁺ requires 384.2220 found 384.2218; **Mp**: 85 - 87°C.

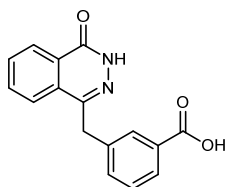
(4-(Cyclopropanecarbonyl)piperazin-1-yl)(2-fluorophenyl)methanone

To a round bottom flask was added, 2-fluorobenzoic acid (1.00 g, 7.14 mmol), DCM (40 mL), diisopropylethylamine (1.86 mL, 10.7 mmol) and HBTU (4.06 g, 10.7 mmol). The reaction mixture was then stirred for 30 min at room temperature before adding cyclopropylpiperazine-1-ylmethanone (1.52 mL, 10.7 mmol). The reaction was stirred overnight before the excess solvent with removed *in vacuo* and the

crude material purified *via* flash column chromatography (EtOAc:MeOH 10:1) affording (4-(Cyclopropanecarbonyl)piperazin-1-yl)(2-(4,4,5,5-tetramethyl-1,3,2-dioxaborolan-2-yl)phenyl)methanone as a white solid (1.32 g, 4.78 mmol 67%) in a mixture of rotamers (2:1). In each case the shift relating to the minor rotamer has been donated with an asterisk.*

¹H NMR (400 MHz, CDCl₃) δ = 7.40 – 7.29 (m, 2H + 2H*), 7.16 (td, J = 7.5, 1.1 Hz, 1H + 1H*), 7.04 (ddd, J = 9.4, 8.3, 1.1 Hz, 1H + 1H*), 3.88 – 3.46 (m, 6H + 6H*), 3.38 – 3.20 (m, 2H + 2H*), 1.76 – 1.58 (m, 1H + 1H*), 0.98 – 0.88 (m, 2H + 2H*), 0.83 – 0.62 (m, 2H + 2H*); **¹³C NMR** (100 MHz, CDCl₃) δ = 172.3 (1C + 1C*), 165.4 (1C + 1C*), 158.0 (d, J = 247.7 Hz, 1C + 1C*), 131.7 (d, J = 8.0 Hz, 1C + 1C*), 129.1 (1C + 1C*), 124.9 (d, J = 3.5 Hz, 1C + 1C*), 123.5 (d, J = 17.4, 1C + 1C*), 115.8 (d, J = 21.3, 1C + 1C*), 47.0 (1C*), 46.7 (1C), 45.6 (1C*), 45.1 (1C), 42.2 (2C), 41.9 (1C*), 41.7 (1C*), 11.0 (1C + 1C*), 7.64 (2C + 2C*); **¹H¹⁹F NMR** (376 MHz, CDCl₃) δ = - 115.0 (s, 1F*), - 115.1 (s, 1F); **IR** (ν , cm⁻¹): 1630, 1460, 1219, 1004, 727; **HRMS** (ESI) for C₁₅H₁₈¹⁹FN₂O₂ [M+H]⁺ requires 277.1282 found 277.1285; **Mp**: 65 - 67°C.

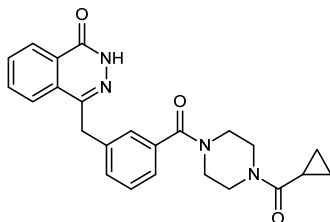
3-((4-oxo-3,4-dihydrophthalazin-1-yl)methyl)benzoic acid



A solution of Dimethyl-(3-oxo-1,3-dihydrobenzofuran-1-yl)phosphonate (7.25 g, 30.0 mmol) and 3-formylbenzonitrile (2.62 g, 20.0 mmol) in THF (250 mL) was prepared at room temperature. The solution was then cooled to 0°C followed by the addition of Et₃N (6.10 mL, 30.0 mmol). The reaction mixture was warmed to room temperature and was stirred for 48 h, followed by concentration in vacuo to produce a white solid. The solid was suspended in water, collected by vacuum filtration and washed with hexane (2 × 20 mL) and Et₂O (3 × 20 mL) affording 3-((3-oxoisobenzofuran-1(3H)-ylidene)methyl)benzonitrile (4.40 g) as a crude white solid which was then taken through to the next step without further purification. 3-((3-oxoisobenzofuran-1(3H)-ylidene)methyl)benzonitrile (4.40 g, 17.8 mmol) was suspended in water (100 mL) and 13 M NaOH was added (26.4 mL, 238 mmol). The mixture was heated to 90°C and stirred for 2 h, after which it was warmed to reflux (140°C), followed by the addition of hydrazine monohydrate (7.48 mL, 240 mmol) and a further 16 h of stirring. The mixture was then cooled to room temperature and acidified with 5 M HCl to an approximate pH of 2. The solid precipitate was collected by vacuum filtration and washed with water (100 mL) and Et₂O (3 × 100 mL) affording 3-((4-oxo-3,4-dihydrophthalazin-1-yl)methyl)benzoic acid (4.18 g, 15.0 mmol, 50%, two steps) as a white solid.

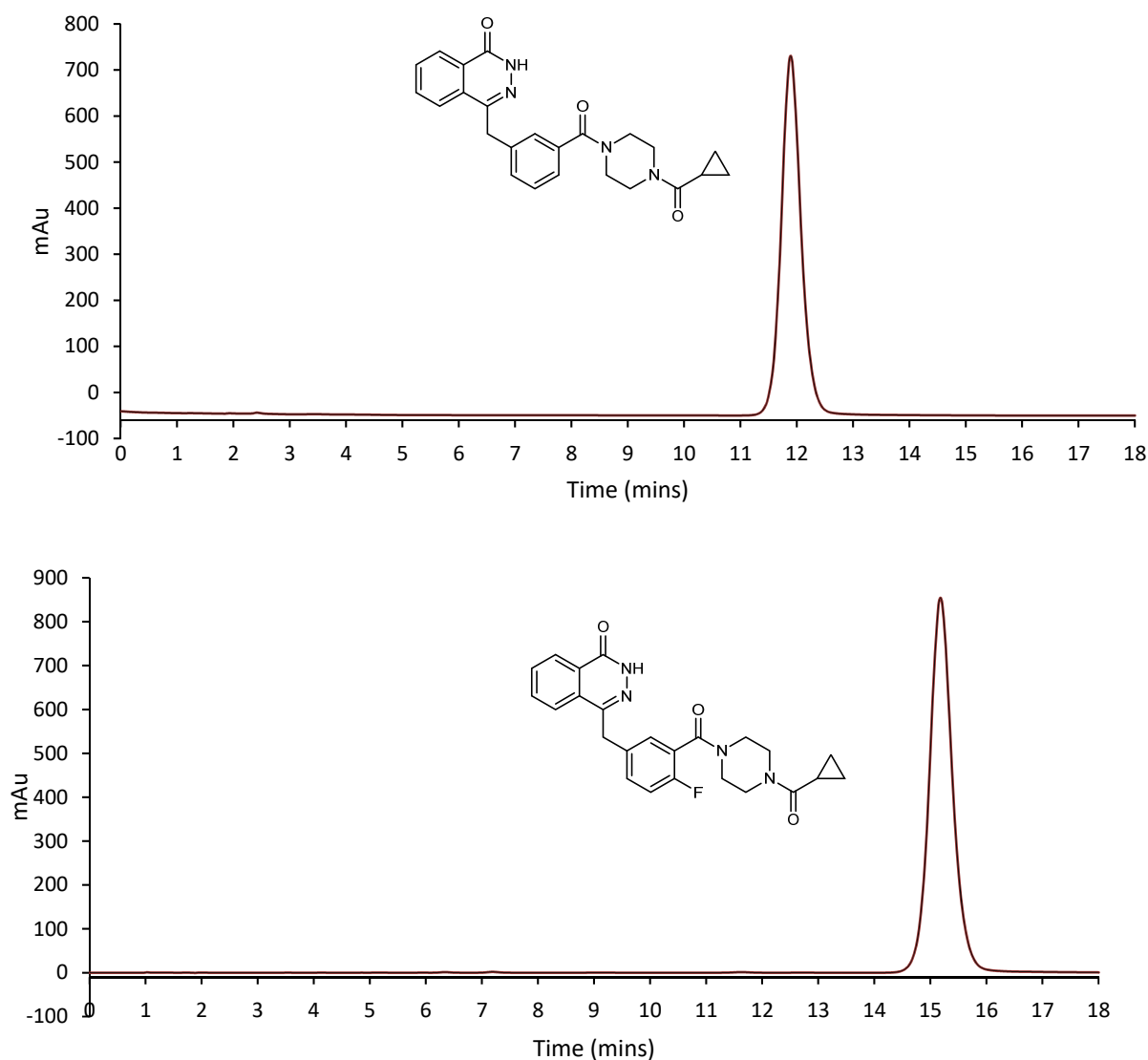
¹H NMR (400 MHz, DMSO-*d*₆) δ = 12.64 (s, 1H), 8.25 (dd, *J* = 7.9, 1.4 Hz, 1H), 7.96 (d, *J* = 7.9 Hz, 1H), 7.91 – 7.85 (m, 2H), 7.82 (dd, *J* = 7.6, 1.2 Hz, 1H), 7.80 – 7.75 (m, 1H), 7.58 (dt, *J* = 7.7, 1.5 Hz, 1H), 7.42 (t, *J* = 7.7 Hz, 1H), 4.38 (s, 2H); **¹³C NMR** (100 MHz, DMSO-*d*₆) δ = 167.6, 159.8, 145.5, 139.1, 134.0, 133.7, 132.0, 131.4, 129.8, 129.5, 129.3, 128.3, 127.9, 126.5, 126.0; **IR** (ν , cm⁻¹): 3004, 1686, 1457, 1270, 1082, 937, 762, 666; **HRMS** (ESI) for C₁₆H₁₁N₂O₃ [M-H]⁻ requires 279.0840 found 279.0647; **Mp**: > 250°C.

4-(3-(4-(cyclopropanecarbonyl)piperazine-1-carbonyl)benzyl)phthalazin-1(2H)-one



To a solution of 3-((4-oxo-3,4-dihydrophthalazin-1-yl)methyl)benzoic acid (1.00 g, 3.57 mmol) in DCM (100 mL) was added DIPEA (930 μ L, 5.36 mmol) and HBTU (2.63 g, 5.36 mmol). The reaction mixture was stirred for 1 h before addition of cyclopropylpiperazine-1-ylmethanone (760 μ L, 5.36 mmol) was carried out. The reaction mixture was then stirred at room temperature for 48 h, and the reaction mixture was extracted with DCM (3 \times 50 mL) and washed with water (3 \times 50 mL). The organic layers were collected, dried with MgSO₄ and the excess solvent removed *in vacuo*. Purification *via* reverse phase HPLC was then carried (Supplemental Figure 2) out affording 4-(3-(4-(cyclopropanecarbonyl)piperazine-1-carbonyl)benzyl)phthalazin-1(2H)-one (810 mg, 55%) as a white solid.

¹H NMR (400 MHz, CDCl₃) δ = 11.83 (bs, 1H), 8.46 – 8.39 (m, 1H), 7.73 – 7.67 (m, 3H), 7.37 – 7.30 (m, 3H), 7.27 – 7.20 (m, 1H), 4.33 (s, 2H), 3.89 – 3.18 (m, 8H), 1.78 – 1.60 (m, 1H), 1.00 – 0.90 (m, 2H), 0.82 – 0.64 (m, 2H); **¹³C NMR** (100 MHz, CDCl₃) δ = 172.4, 170.4, 161.1, 145.7, 138.3, 135.5, 133.5, 131.5, 130.2, 129.6, 129.0, 128.2, 127.2, 127.0, 125.5, 125.1, 47.5, 45.3, 42.3 (2C), 38.5, 14.2, 11.0, 7.73; **IR** (ν , cm⁻¹): 2925, 1632, 1430, 1353, 1101, 772; **HRMS** (ESI) for C₂₄H₂₅N₄O₃ [M+H]⁺ requires 417.1856 found 417.2001; **Mp**: 82 – 84°C.



Supplemental Figure 2. HPLC UV Trace of 4-(3-(4-(cyclopropanecarbonyl)piperazine-1-carbonyl)benzyl)phthalazin-1(2H)-one and olaparib. HPLC Eluent: Synergi 4 μm Hydro-RP 80A, 150 x 4.6 mm with 25% MeCN/75% H_2O (isocratic 1 mL/min) monitoring with UV (220 nm).

Synthesis of $[\text{Cu}(\text{OTf})_2(\text{impy})_4]$ complex

A solution of imidazo[1,2-b]pyridazine (impy) (758 mg, 6.36 mmol, 10 equiv.) in MeOH (1 mL) was added dropwise at 55°C to a solution of $\text{Cu}(\text{OTf})_2$ (230 mg, 0.636 mmol, 1.0 equiv.) in MeOH (1 mL). The blue precipitate which formed was washed with Et_2O (3 x 2 mL), then recrystallized from hot MeOH to afford $[\text{Cu}(\text{OTf})_2(\text{impy})_4]$ (324 mg, 0.387 mmol, 61%).

Anal. Calcd. for $C_{26}H_{20}CuF_6N_{12}O_6S_2$: C, 37.26; H, 2.41; N, 20.05. Found: C, 37.07; H, 2.33; N, 19.91; **IR** (ATR, neat): ν (cm^{-1}) = 2981, 1620, 1541, 1503, 1374, 1352, 1306, 1281, 1241, 1221, 1149, 1071, 1027, 950, 918, 879, 801, 755, 733, 632.

2. Radiochemical synthesis

Radiochemistry:

$[^{18}F]$ Fluoride was produced by Alliance Medical (UK) via the $^{18}O(p,n)^{18}F$ reaction and delivered as $[^{18}F]$ fluoride in ^{18}O -enriched-water. Radiosynthesis and azeotropic drying was performed on a NanoTek microfluidic device (Advion).

Procedure for preparation of a solution of $[^{18}F]KF/K_{222}$ in MeCN:

A solution of Kryptofix 222 (15 mg) and K_2CO_3 (3 mg) in 1 mL of MeCN/ H_2O , 4:1 was freshly prepared. $[^{18}F]$ Fluoride (3.0-4.0 GBq) was separated from ^{18}O -enriched-water using a Chromafix PSHCO3 ^{18}F separation cartridge (45 mg) and subsequently released with 900 μL (in 6 x 150 μL portions) of the K_{222}/K_2CO_3 solution into a 5 mL V-vial containing a magnetic stir bar in the concentrator. The solution was dried with five cycles of azeotropic drying with MeCN (5 x 200 μL) under a flow of N_2 at 105°C. The dried $[^{18}F]KF/K_{222}$ residue was redissolved in anhydrous MeCN (500 - 1000 μL).

General procedure for small scale heterocycle screening experiments with 4-(4,4,5,5-tetramethyl-1,3,2-dioxaborolan-2-yl)benzonitrile:

A solution of $[^{18}F]KF/K_{222}$ in MeCN (20 - 30 MBq, 10-50 μL) was dispensed into a V-vial containing $Cu(OTf)_2(py)_4$ (0.0053 mmol), 4-(4,4,5,5-tetramethyl-1,3,2-dioxaborolan-2-yl)benzonitrile (13.7 mg, 0.06 mmol) and a magnetic stirrer bar. Air (20 mL) was flushed through the reaction vial using a syringe and then a solution containing the heterocycle (0.06 mmol) in DMF (300 μL) was added via syringe. The sealed vial was heated at 110°C for 20 min. The reaction was quenched by addition of water (200 μL). An aliquot was removed for analysis by radioTLC and HPLC for radiochemical conversion and product identity. Analysis was performed using a Waters Nova-Pak C18 column (4 μm , 3.9 x 150 mm) at a flow rate 1 mL/min. Radio-TLC was performed on Merck Kiesegel 60 F254 plates, using n-hexane/EtOAc (1:1) as eluent. Analysis was performed using a plastic scintillator/PMT detector.

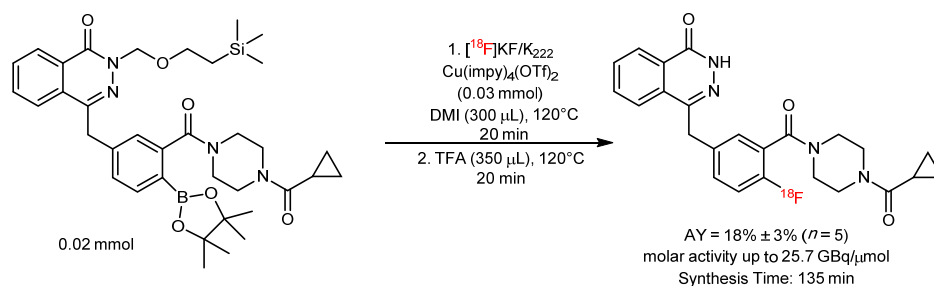
General procedure for small scale ^{18}F -labeling of arenes:

A solution of [^{18}F]KF/K₂₂₂ in MeCN (20 - 30 MBq, 10 - 50 μL) was dispensed into a V-vial containing Copper source (0.03 mmol), aryl pinacol boronate (0.02 mmol) and a magnetic stirrer bar. Air (20 mL) was flushed through the reaction vial using a syringe and then solvent (300 μL) was added via syringe. The sealed vial was heated at 110°C for 20 min. The reaction was quenched by addition of water (200 μL). An aliquot was removed for analysis by radioTLC and HPLC for radiochemical conversion and product identity. Analysis was performed using the gradient given below with a Waters Nova-Pak C18 column (4 μm , 3.9 x 150 mm) at a flow rate 1 mL/min. Radio-TLC was performed on Merck Kiesegel 60 F254 plates, using as eluent DCM/MeOH (9:1). Analysis was performed using a plastic scintillator/PMT detector.

HPLC gradient for small scale heterocycle screening experiments and small scale ^{18}F -labeling of arenes:

Water/MeCN, 1 mL/min, Waters Nova-Pak C18 Column, 4 μm , 3.9 x 150 mm 0 - 1 min (5% MeCN) isocratic 1 - 10 min (5% MeCN to 95% MeCN) linear increase 10 - 14 min (95% MeCN) isocratic 14 - 15 min (95% MeCN to 5% MeCN) linear decrease 15 - 17 min (5% MeCN) isocratic.

Procedure for the Synthesis and Isolation of ^{18}F -Olaparib:



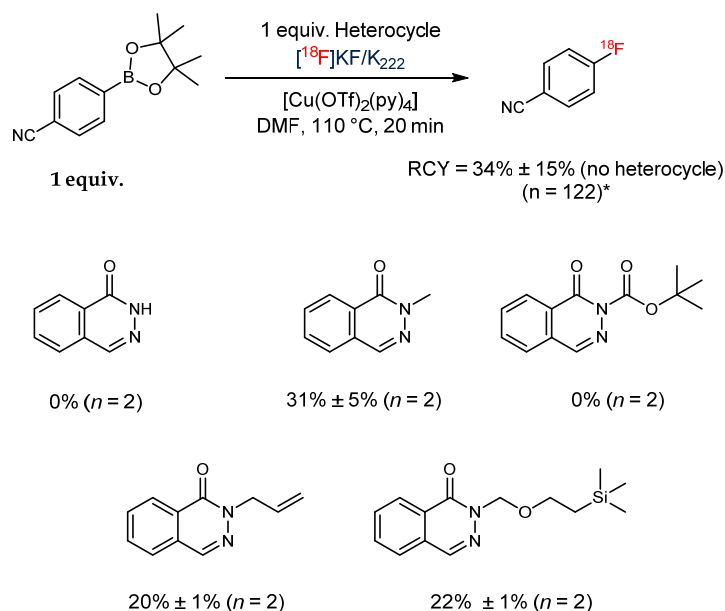
^{18}F -olaparib was obtained *via* the Cu-mediated ^{18}F -fluorodeboronation of the corresponding boronic ester precursor (Figure 1, 2), using methodology previously described by Tredwell *et al.* (6) [^{18}F]Fluoride was separated from ^{18}O -enriched-water using an anion exchange cartridge (Sep-Pak Accell Plus QMA Carbonate Plus Light Cartridge, 46 mg Sorbent per Cartridge, 40 μm particle size, Waters) and released with 900 μL (in 6 x 150 μL portions) of a solution of K₂₂₂/K₂C₂O₄/K₂CO₃ (kryptofix 222 (6.3 mg), K₂C₂O₄ (1 mg) and K₂CO₃ (0.1 mg) in 1 mL of MeCN/H₂O, 4:1) into a 5 mL V-vial containing a magnetic stir bar in the concentrator. The solution was dried with five cycles of azeotropic drying with MeCN (5 x 200 μL) under a flow of N₂ at 105°C. The 5 mL vial containing the dried [^{18}F]KF/K_{2.2.2} complex was purged with 30 mL of air using a syringe and then a solution of arylboronate precursor (13.4 mg, 0.02 mmol) and Cu(OTf)₂(impv)₄ (25 mg, 0.03 mmol) in anhydrous 1,3-dimethyl-2-imidazolidinone (DMI) (300 μL) was added. The mixture was heated at 120°C for 20 min in a sealed vial with stirring. After 20 min, TFA (350 μL) was added and

stirring was continued at 120°C for 20 min. The reaction was then cooled to room temperature before quenching with H₂O (6 mL) and eluting over a Oasis HLB Plus cartridge (preconditioned with 2 mL MeOH and 10 mL H₂O). The vial was then rinsed with CH₃CN:H₂O (1:9, 2.0 mL), and eluting over the Oasis HLB cartridge after which the product was eluted with CH₃CN (2.0 mL) into a 5 mL V-vial. The MeCN was evaporated under a flow of N₂ at 100°C until approximately 50 µL remained. The reaction mixture was then diluted in with 28% MeCN/ 72% 25 mM NH₄HCO₂ in H₂O and loaded directly onto a 2 mL HPLC loop and injected on a semi-Prep HPLC column (Synergi 4µm Hydro-RP 250x10mm) and eluted into a collection vial with 28% MeCN/ 72% 25 mM NH₄HCO₂ in H₂O monitoring with UV (254 nm) and radioactive traces.

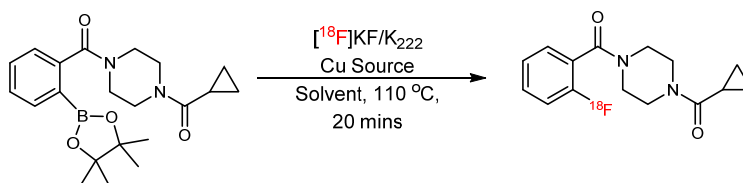
The ¹⁸F-olaparib was collected in 10 mL of H₂O and eluted over a Oasis HLB Plus cartridge (preconditioned with 2 mL MeOH and 10 mL H₂O). The cartridge was washed with H₂O (1.0 mL), after which the product was eluted with EtOH (2.0 mL). The ethanol was evaporated under a flow of N₂ while heating at 100°C. The dry residue was then re-dissolved in 10% DMSO/PBS (pH = 7.4).

The Molar Activity of ¹⁸F-olaparib was assessed by radio-HPLC, using an analytical Synergi 4 µm Hydro-RP 80A column, 150 x 4.6 mm eluted with 25% MeCN/75% H₂O (isocratic 1 mL/min), monitoring with UV (220 nm) and radioactive traces.

Test reactions were carried out on components of the molecule, to explore the compatibility of all chemical motifs with the Cu-assisted radiolabelling reaction (Supplemental Figure 3, 4, 5, 6). Additional optimisation of the Cu-complex catalyst and drying methods was performed to improve activity yields (Supplemental Table 1, 2). Molar activity was calculated based on a standard series and co-injection of cold, unlabelled olaparib (Supplemental Figure 7, Supplemental Table 3).



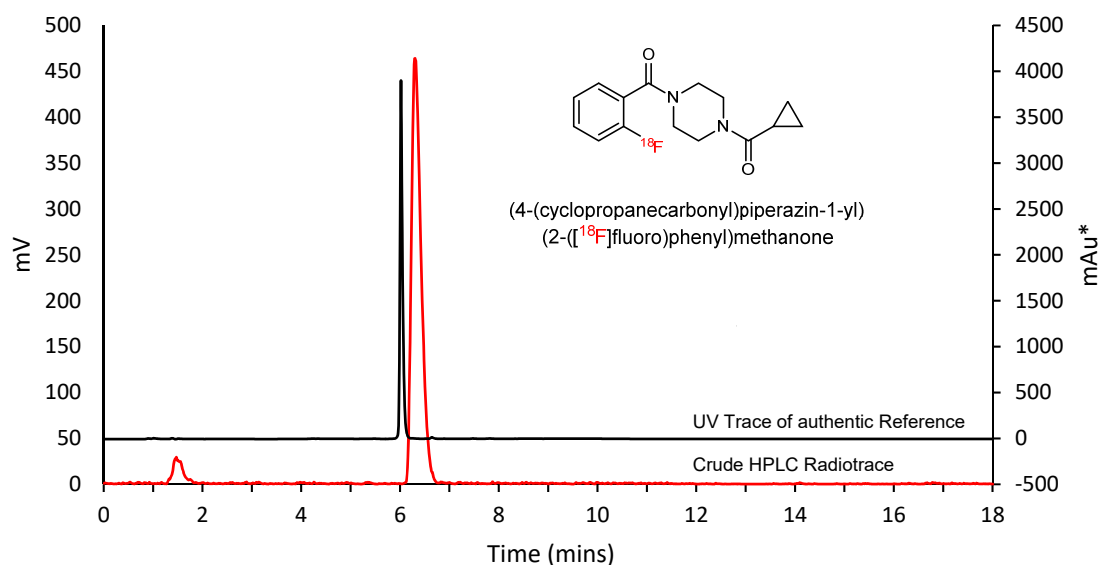
Supplemental Figure 3: Screening of Protecting Groups: *See reference (7)



Supplemental Figure 4: Radiochemical conversion of (4-(Cyclopropanecarbonyl) piperazin-1-yl)(2-(4,4,5,5-tetramethyl-1,3,2-dioxaborolan-2-yl)phenyl)methanone

Supplemental Table 1. Radiochemical conversion of (4-(Cyclopropanecarbonyl)piperazin-1-yl)(2-(4,4,5,5-tetramethyl-1,3,2-dioxaborolan-2-yl)phenyl)methanone

Cu Source	Solvent (400 μ L)	RCC (n = 2)
Cu(OTf) ₂ (py) ₄	DMA	17% ± 3%
Cu(OTf) ₂ (impy) ₄	DMA	48% ± 1%
Cu(OTf) ₂ (impy) ₄	DMI	82% ± 1%

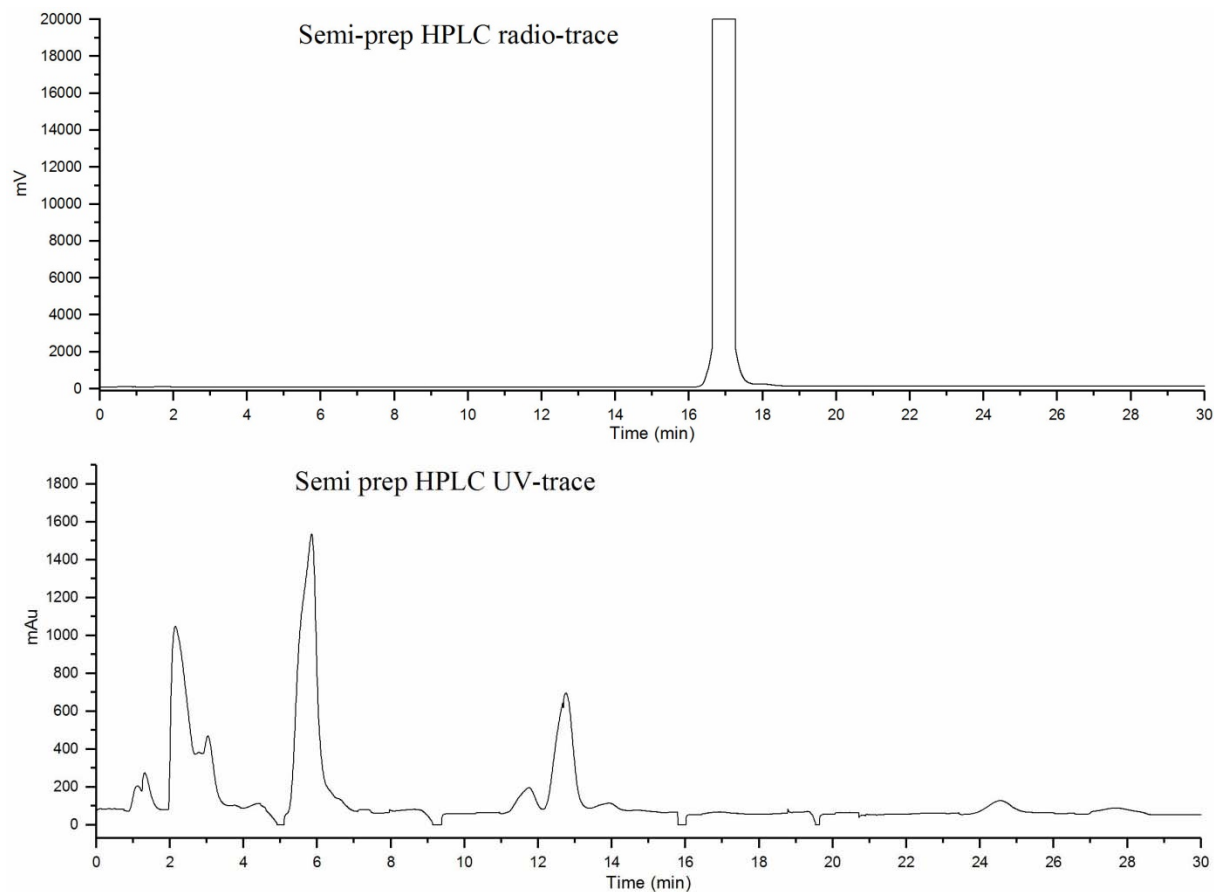


Supplemental Figure 5. UV Trace and Radiotracer of (4-(Cyclopropanecarbonyl)piperazin-1-yl)(2-fluorophenyl)methanone

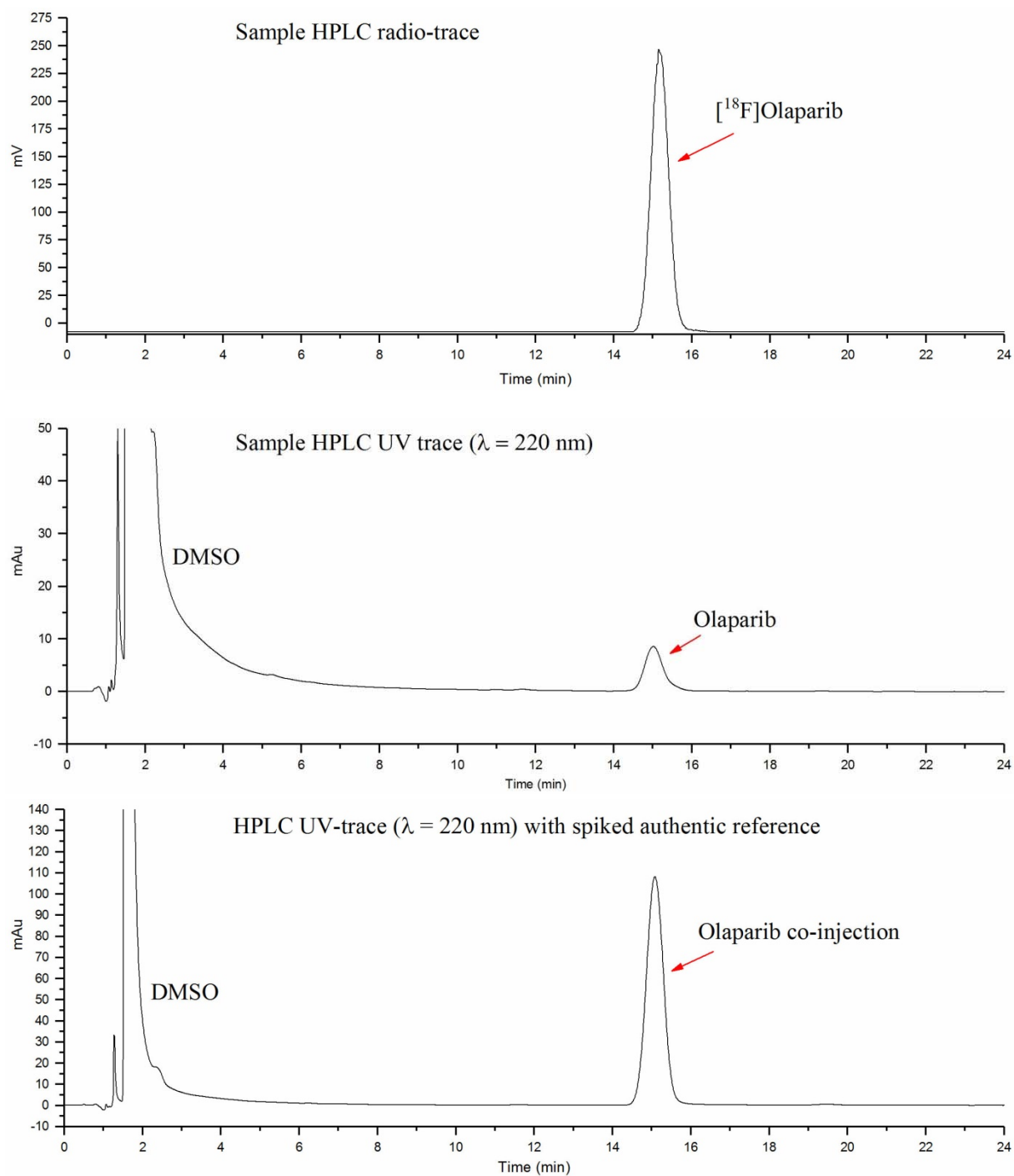
Supplemental Table 2: ¹⁸F-Olaparib Isolation Results:

Run	QMA Ion	Activity (MBq)				RCY (%) ^b	Synthesis Time (min)	Molar Activity (GBqμmol ⁻¹)
		Starting	Dried	HLB 1	HLB 2			
1	Oxalate ^a	5500	3070	1050	290	5	149	7.2
2	Oxalate ^a	3620	2650	1076	550	15	136	10.1
3	Oxalate ^a	3400	1502	711	220	6	154	2.8
4	Oxalate ^a	7750	3120	1215	309	4	135	9.8
5	Oxalate ^a	8080	3140	1152	470	6	135	21.3
Radiochemical Yield^c: 7% ± 4% (n = 5)								
6	Carbonate	8510	7420	3890	1168	14	140	10.9
7	Carbonate	10000	8420	4330	2300	23	130	21.3
8	Carbonate	10000	8950	3510	1836	18	129	25.7
9	Carbonate	1510	1281	640	278	18	144	2.7
10	Carbonate	7780	6730	3100	1343	17	132	15.4
Radiochemical Yield^d: 18% ± 3% (n = 5)								

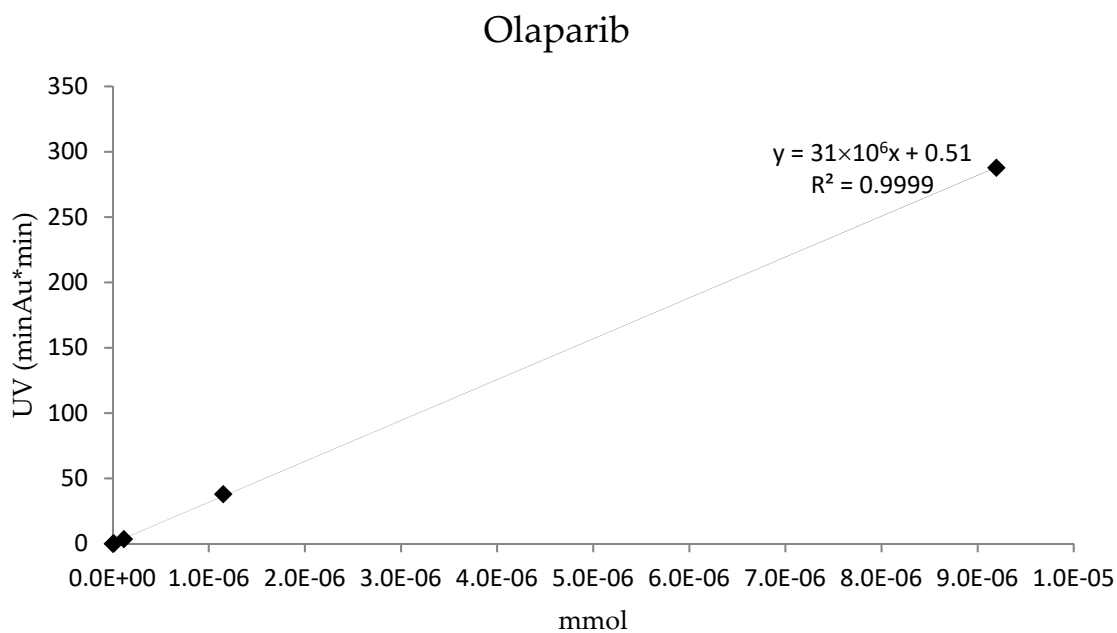
^aPre-conditioned with 3 mL of a 10 mg/mL $K_2C_2O_4(aq)$ solution followed by 5 mL H_2O at a flow rate of 3 mL/min; ^bnon-decay corrected; ^cRCY under oxalate drying conditions; ^dRCY under carbonate drying conditions.



Supplemental Figure 6. Semi-prep radioHPLC purification of ¹⁸F-olaparib



Supplemental Figure 7. Purified ¹⁸F-olaparib was injected onto an analytical column. Additionally, a sample spiked with an authentic reference sample of olaparib (0.7 μg) was analyzed. Analytical HPLC conditions are listed in the previous section.

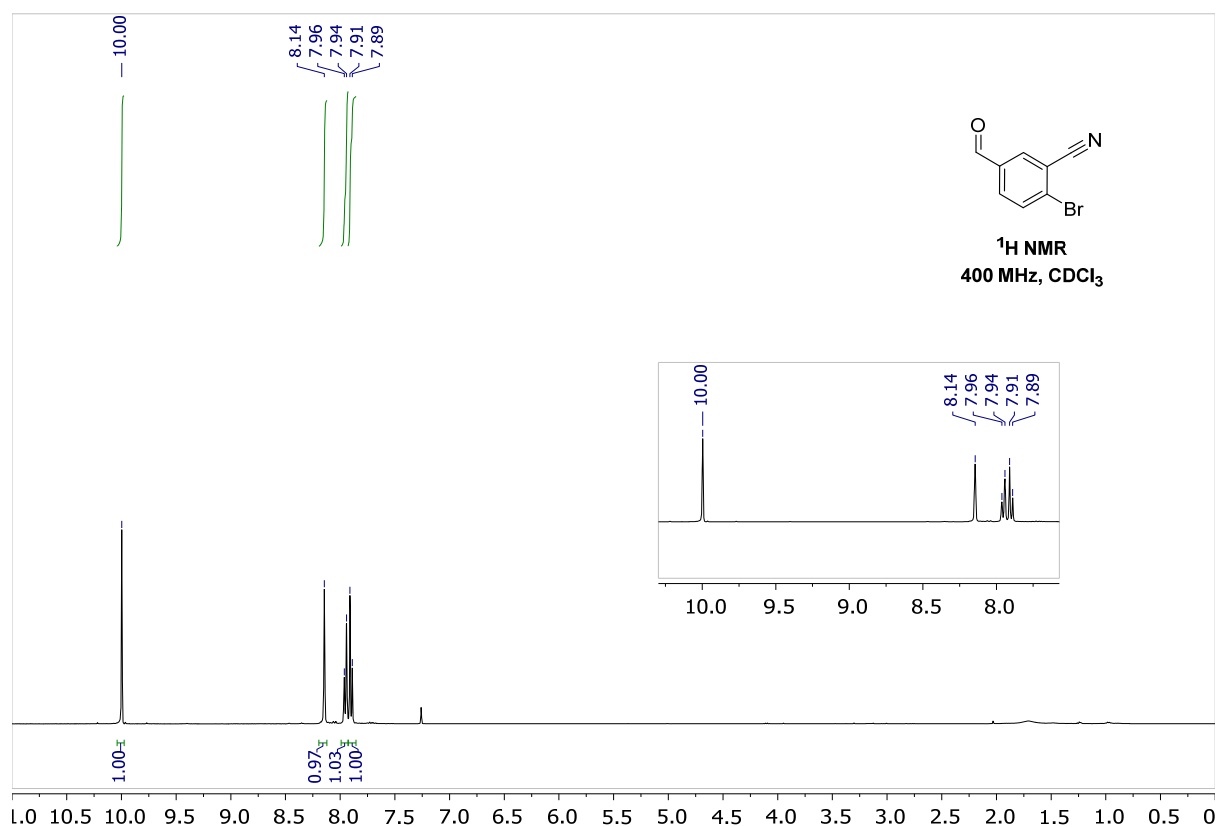
Supplemental Data: Molar Activity of ^{18}F -olaparib:

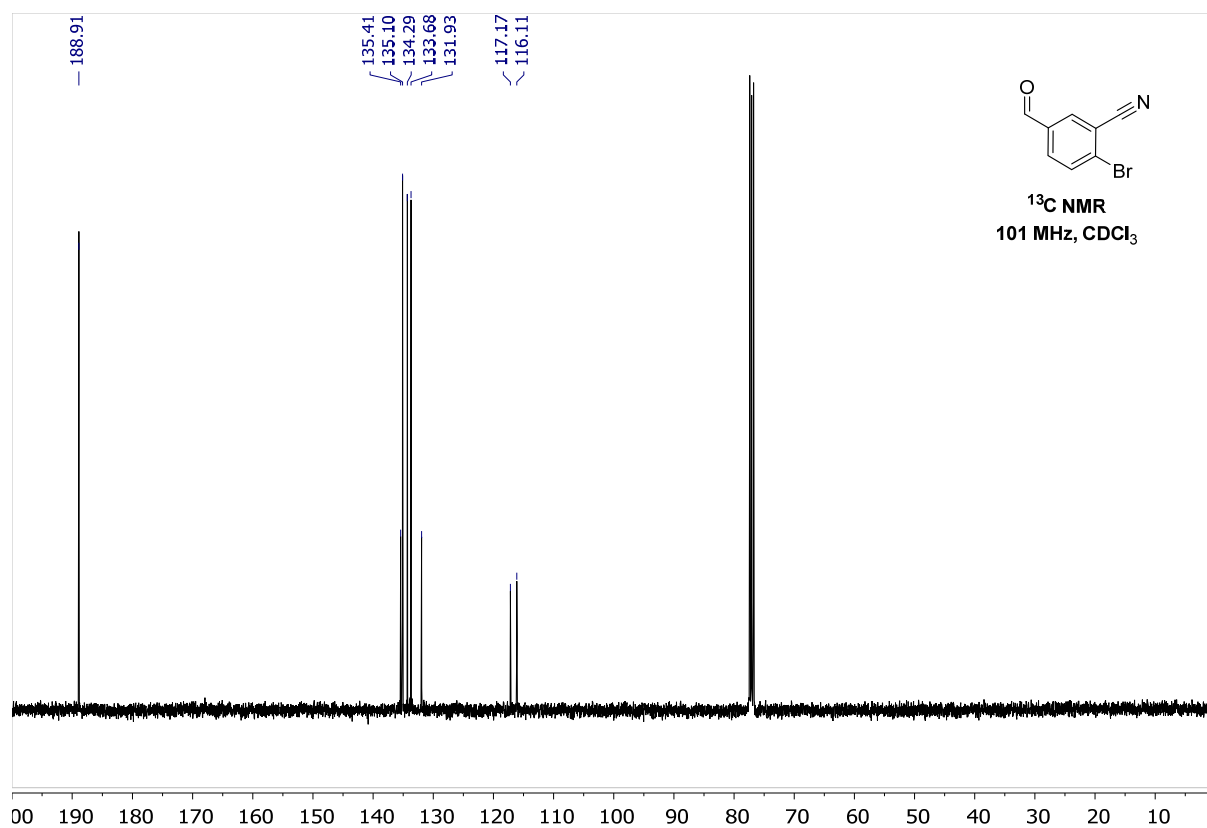
Supplemental Table 3. Molar Activity Calculations for ^{18}F -olaparib ^aUnder oxalate drying conditions;
^bUnder carbonate drying conditions.

Injection Number	Activity (MBq)	Area (mAu*min)	Mmol injected (*10 ⁻⁷)	Molar Activity (GBq.μmol ⁻¹)
1 ^a	2.0	9.16	2.7	7.2
2 ^a	1.4	4.82	1.3	10.4
3 ^a	1.6	18.29	5.6	2.8
4 ^a	0.7	2.73	0.71	9.8
5 ^a	3.1	5.06	1.4	21.3
6 ^b	1.1	3.67	1.0	10.9
7 ^b	1.6	2.86	0.75	21.3
8 ^b	1.7	2.58	0.66	25.7
9 ^b	2.2	25.79	8.1	2.7
10 ^b	2.6	5.79	1.7	15.4

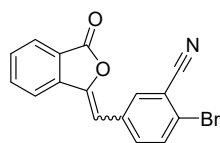
2. NMR Spectra of Novel Compounds:

2-Bromo-5-formylbenzonitrile

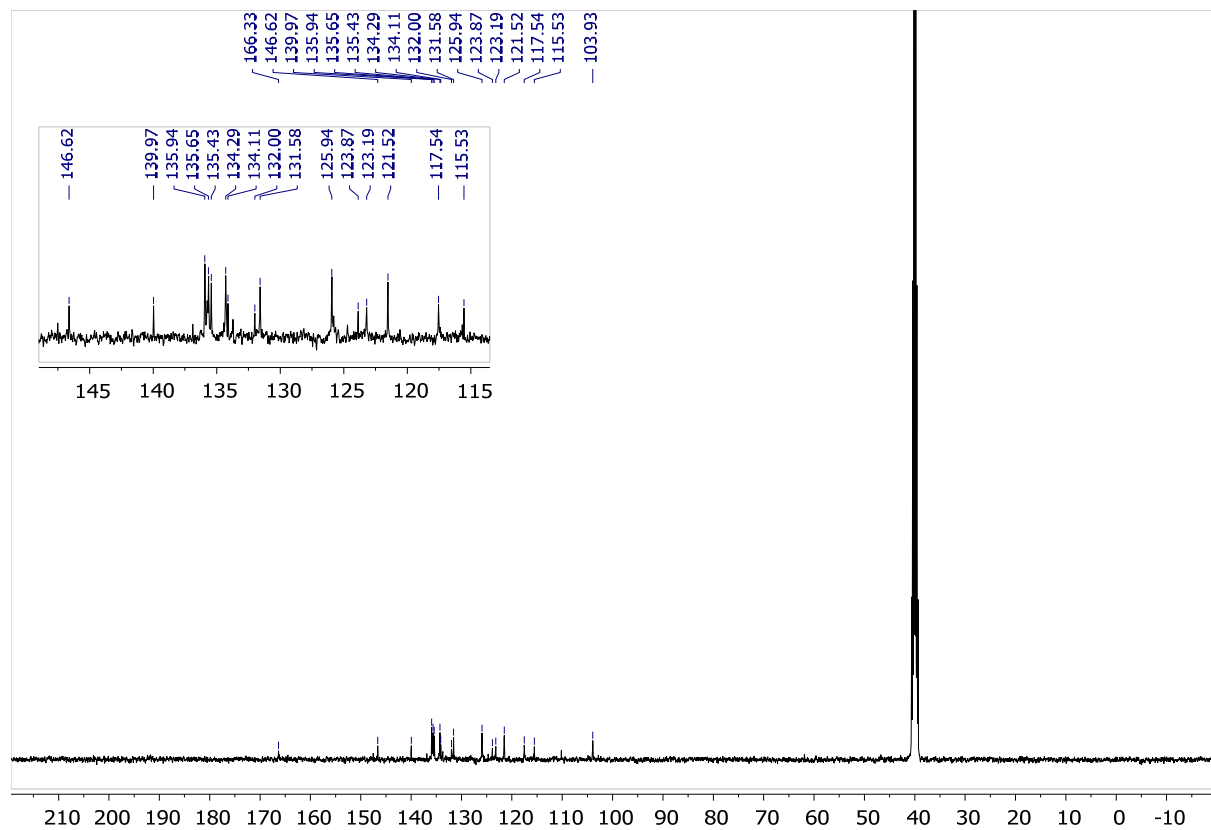
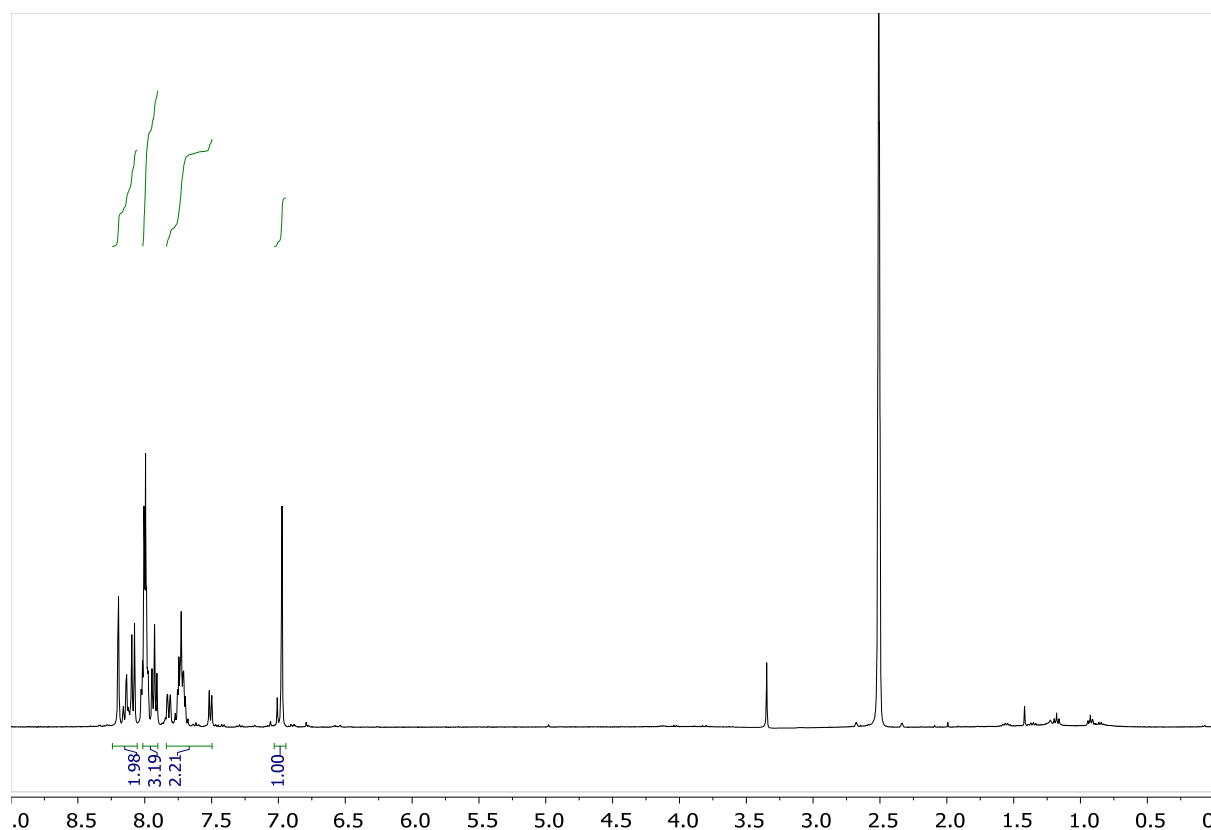




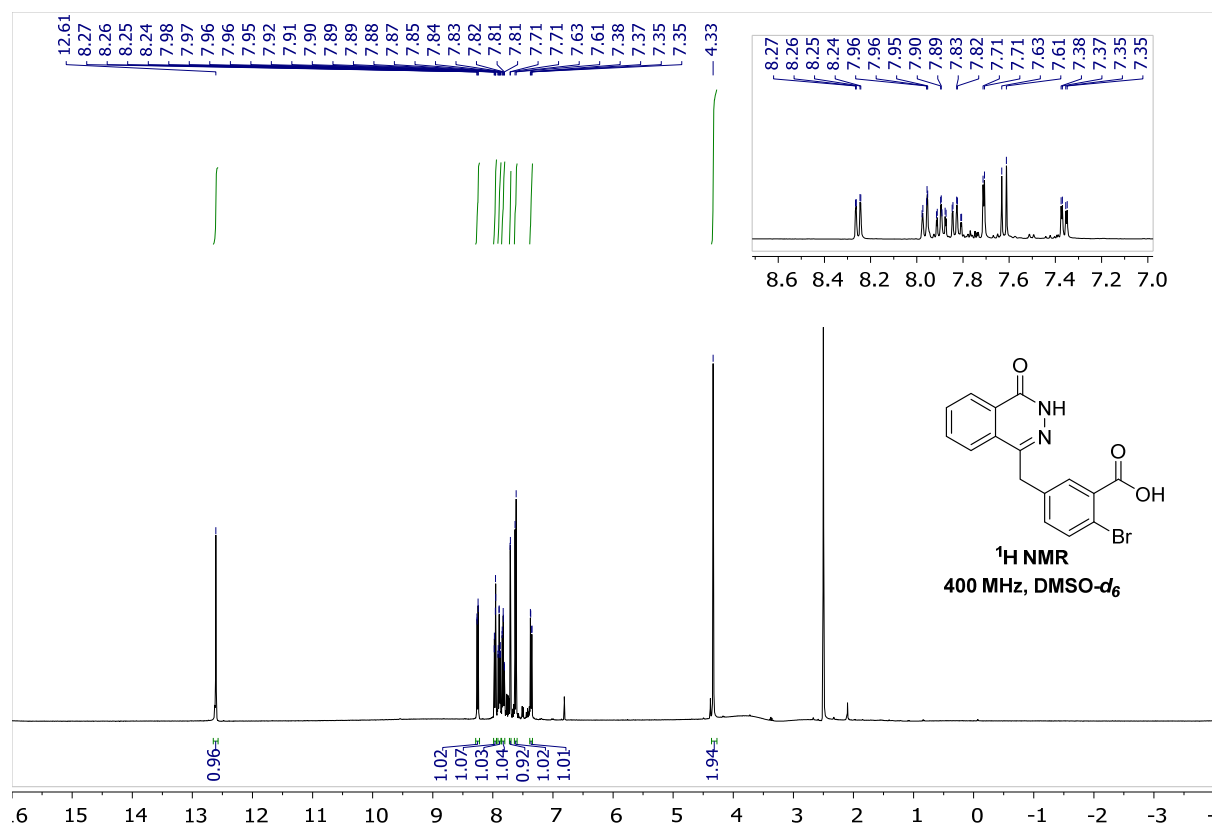
2-Bromo-5-((3-oxoisobenzofuran-1(3H)-ylidene)methyl)benzonitrile

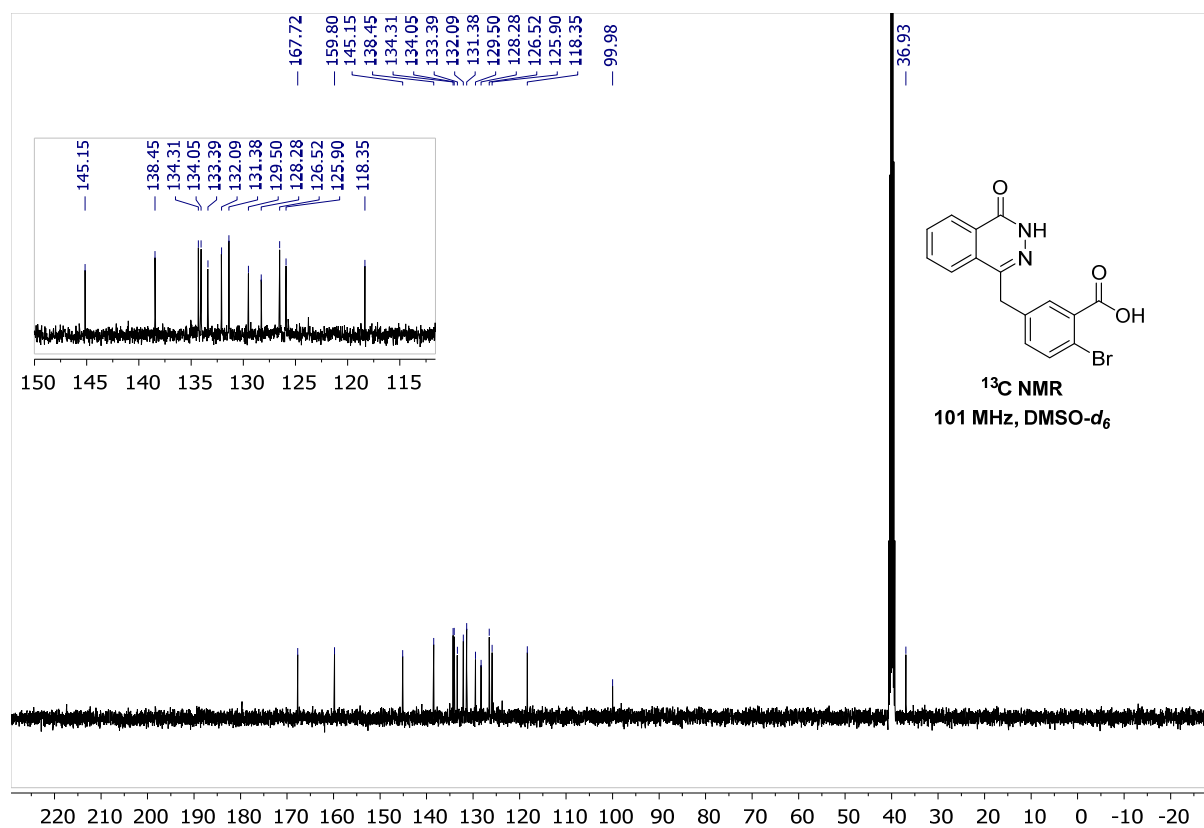


¹³C NMR
101 MHz, DMSO-*d*₆

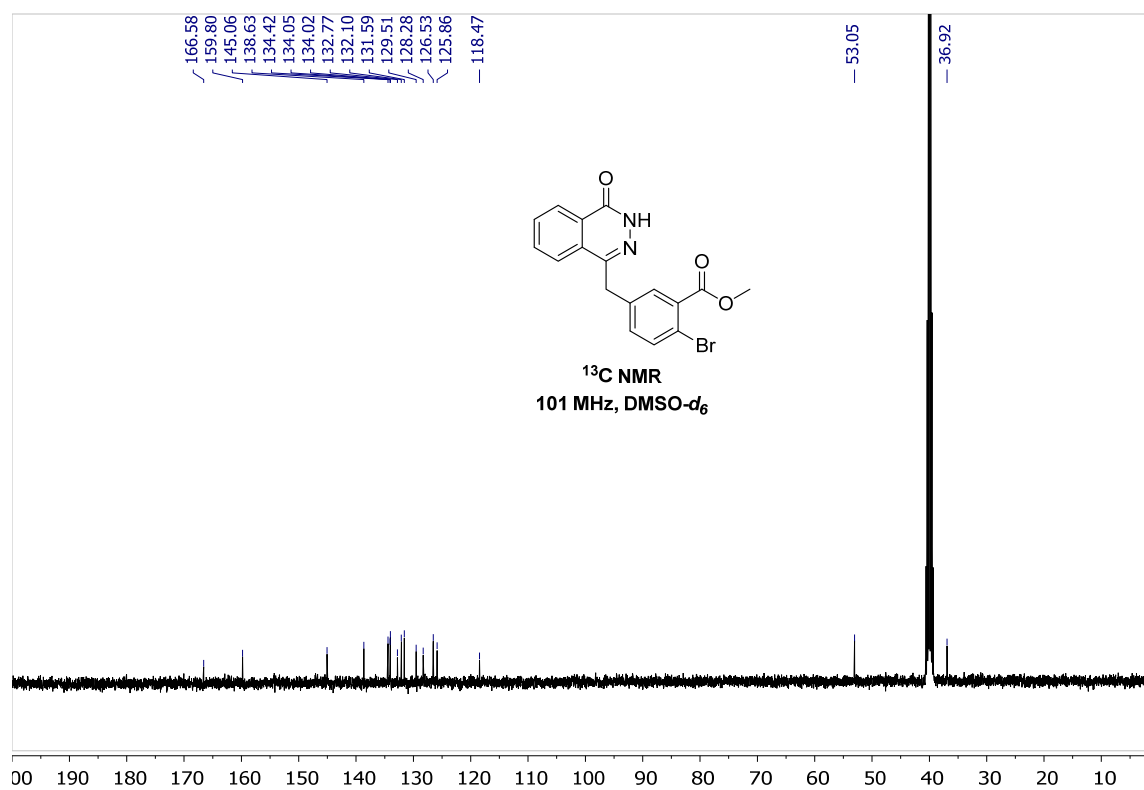
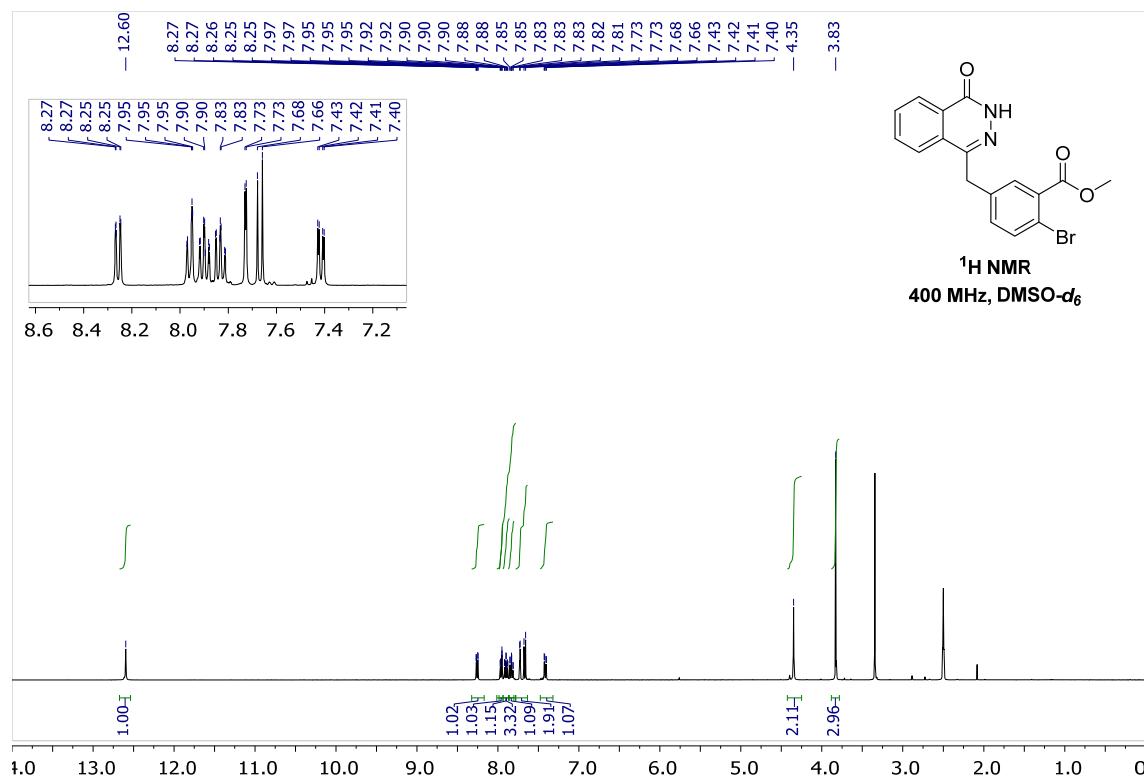


2-Bromo-5-((4-oxo-3,4-dihydrophthalazin-1-yl)methyl)benzoic acid



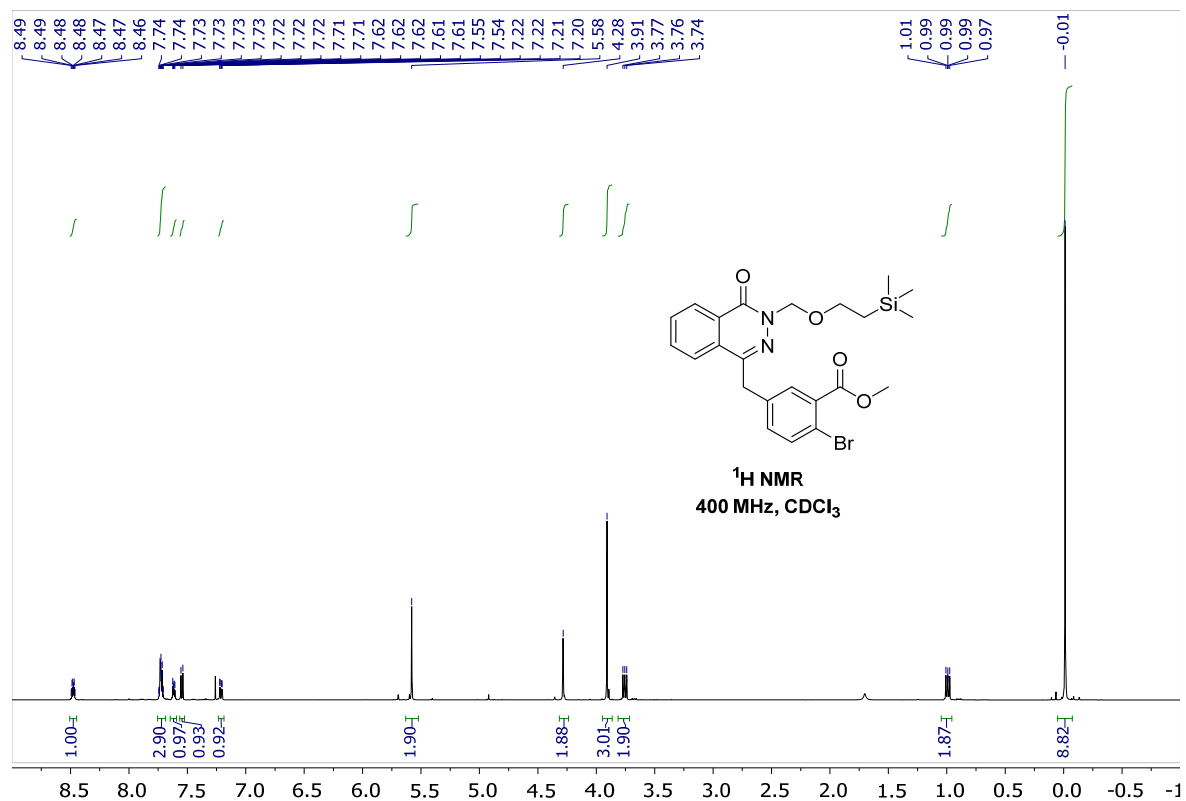


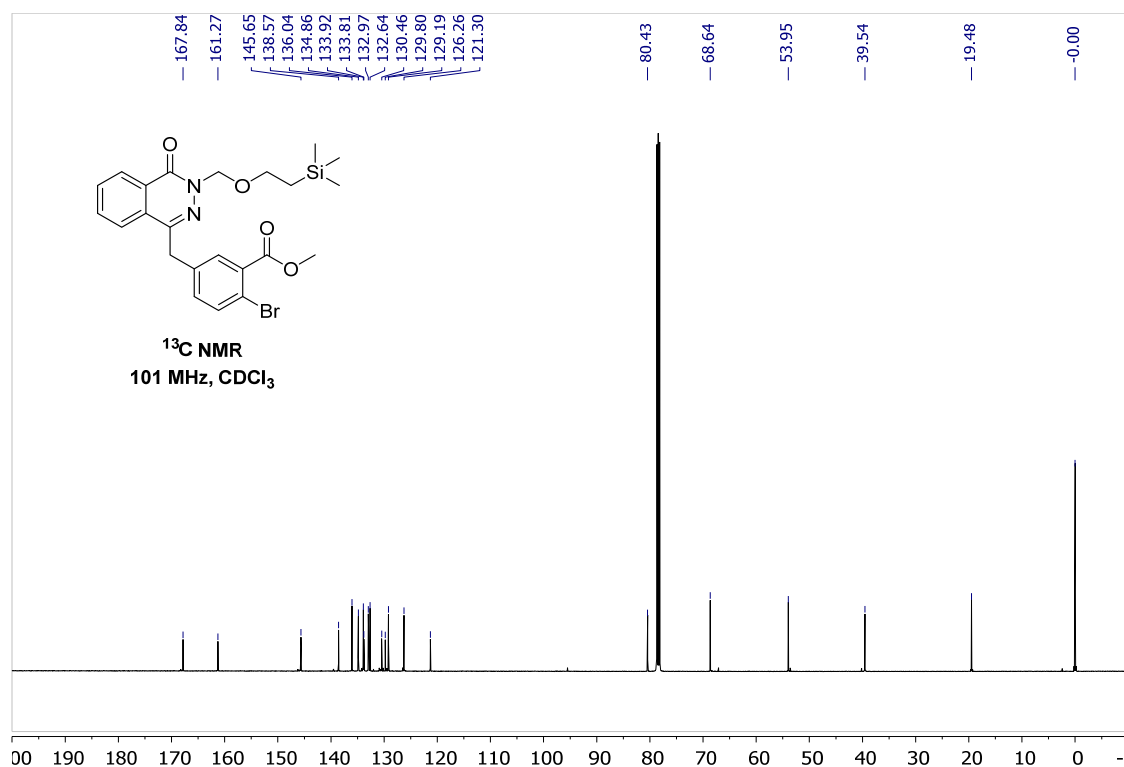
Methyl-2-bromo-5-((4-oxo-3,4-dihydrophthalazin-1-yl)methyl)benzoate



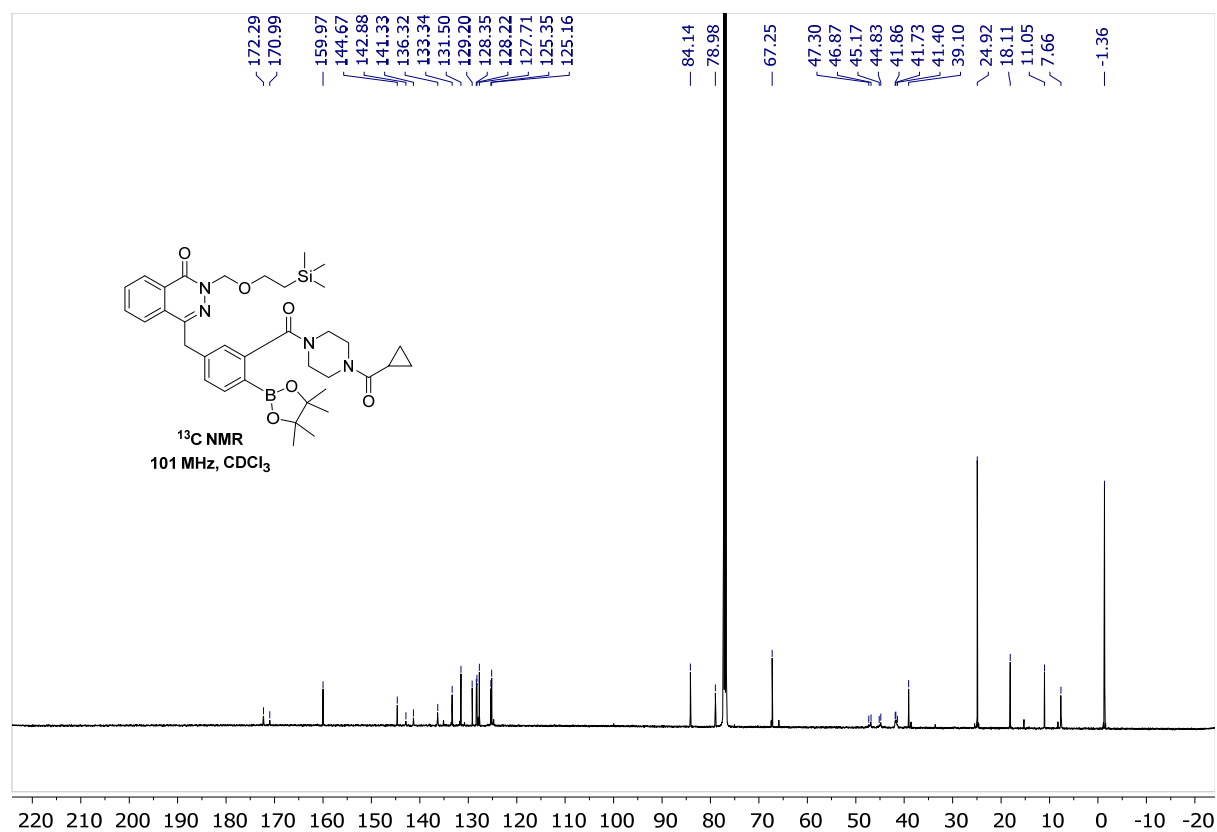
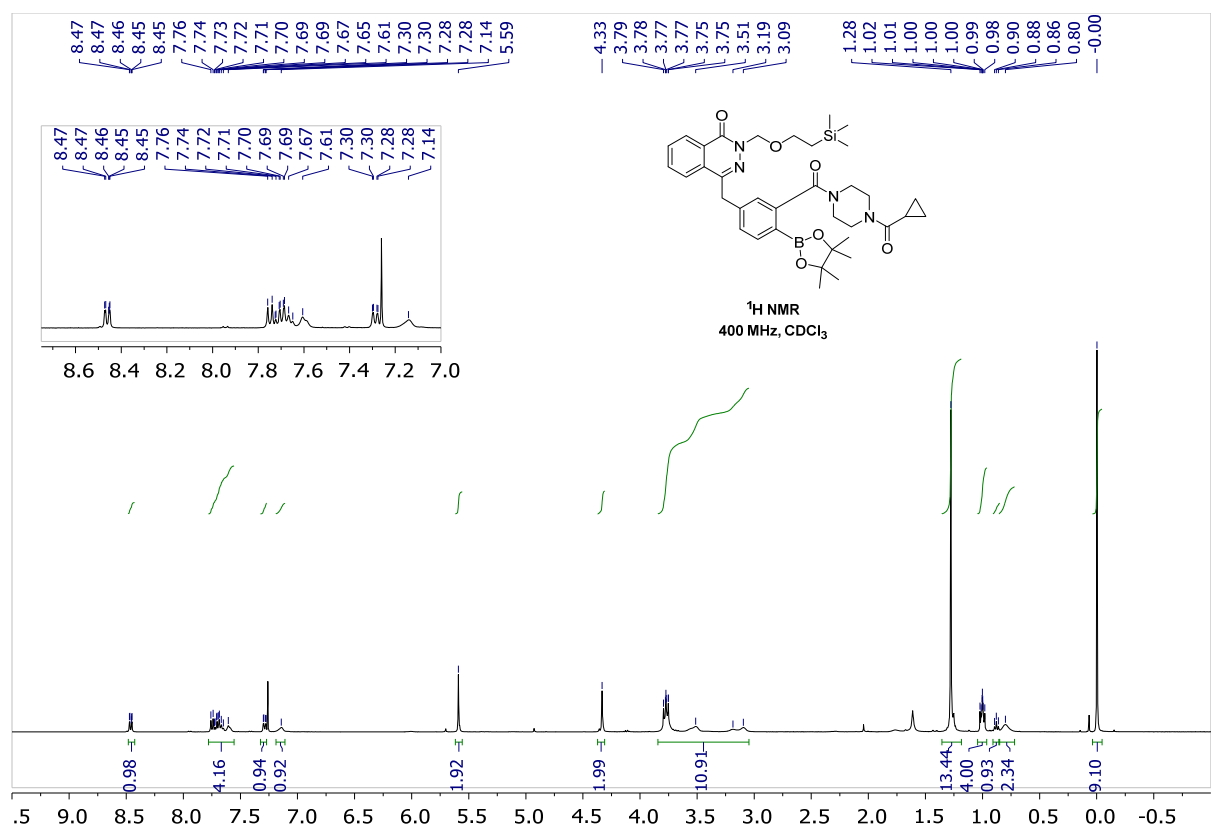
**Methyl-2-bromo-5-((4-oxo-(2-(trimethylsilyl)ethoxy)methyl)-3,4-dihydro
methyl)benzoate**

phthalazin-1-yl)

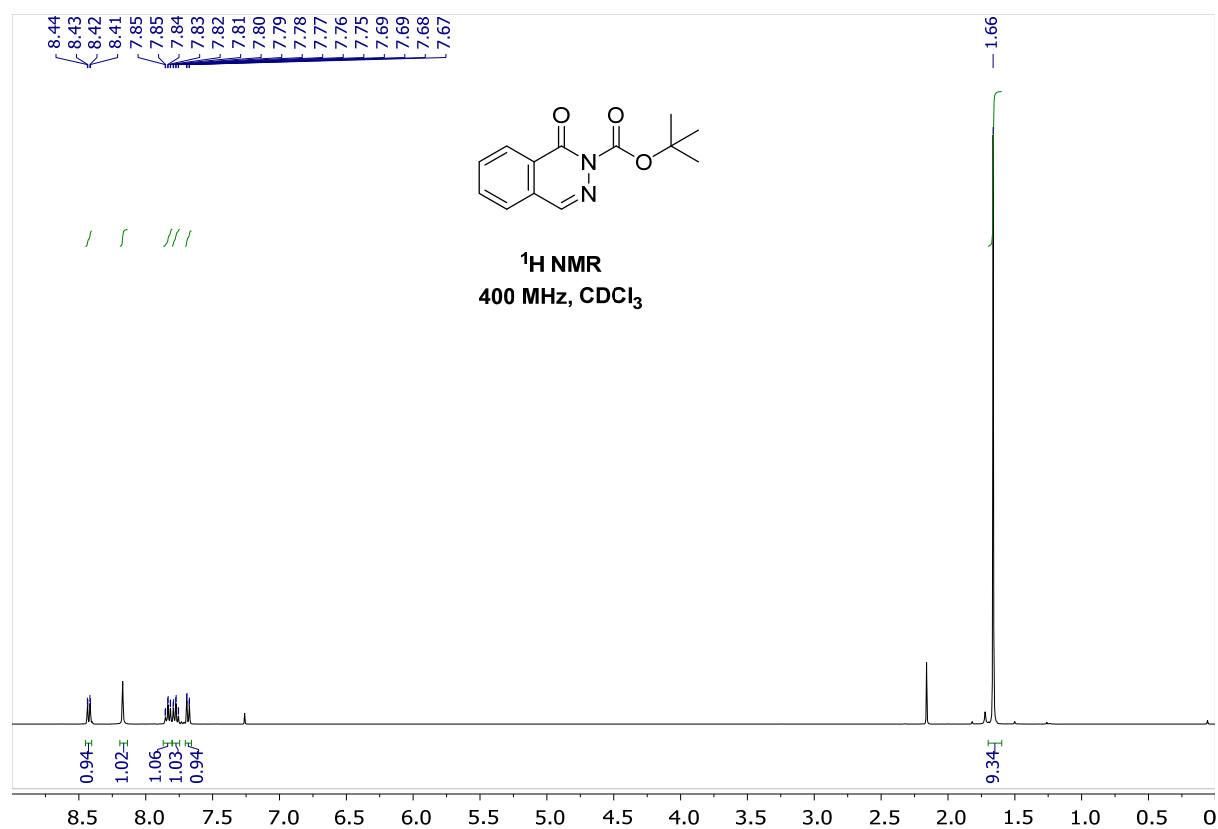


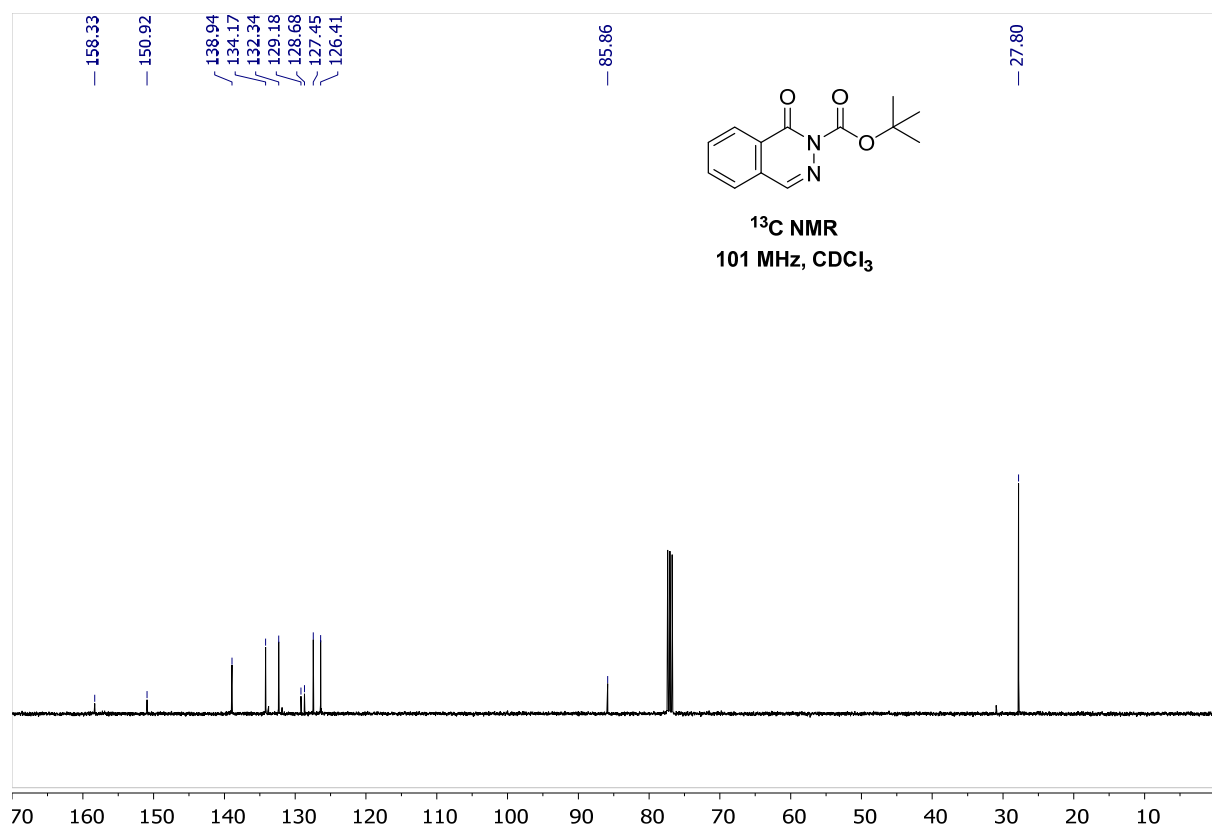


4-(3-(4-(cyclopropanecarbonyl)piperazine-1-carbonyl)-4-(4,4,5,5-tetramethyl-1,3,2-dioxaborolan-2-yl)benzyl)-2-((2-trimethylsilyl)ethoxy)methyl)phthalazin-1(2H)-one

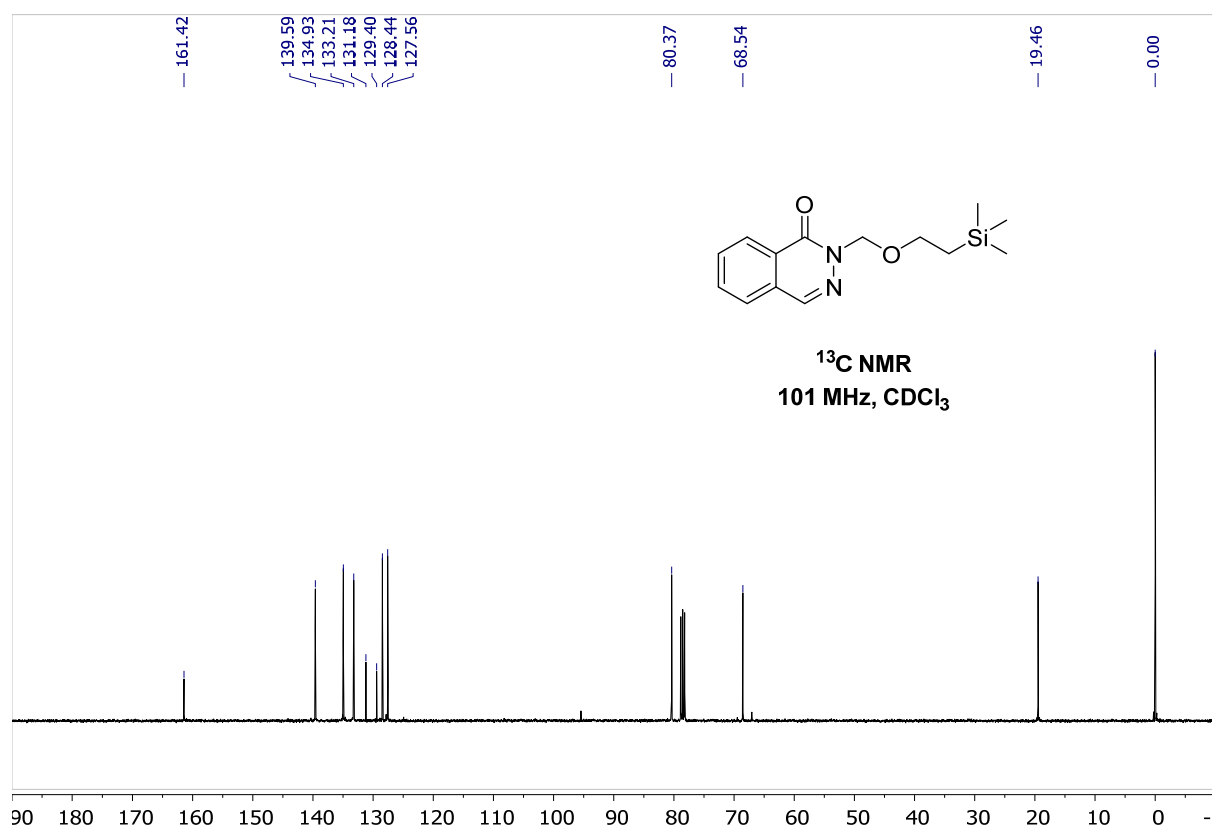
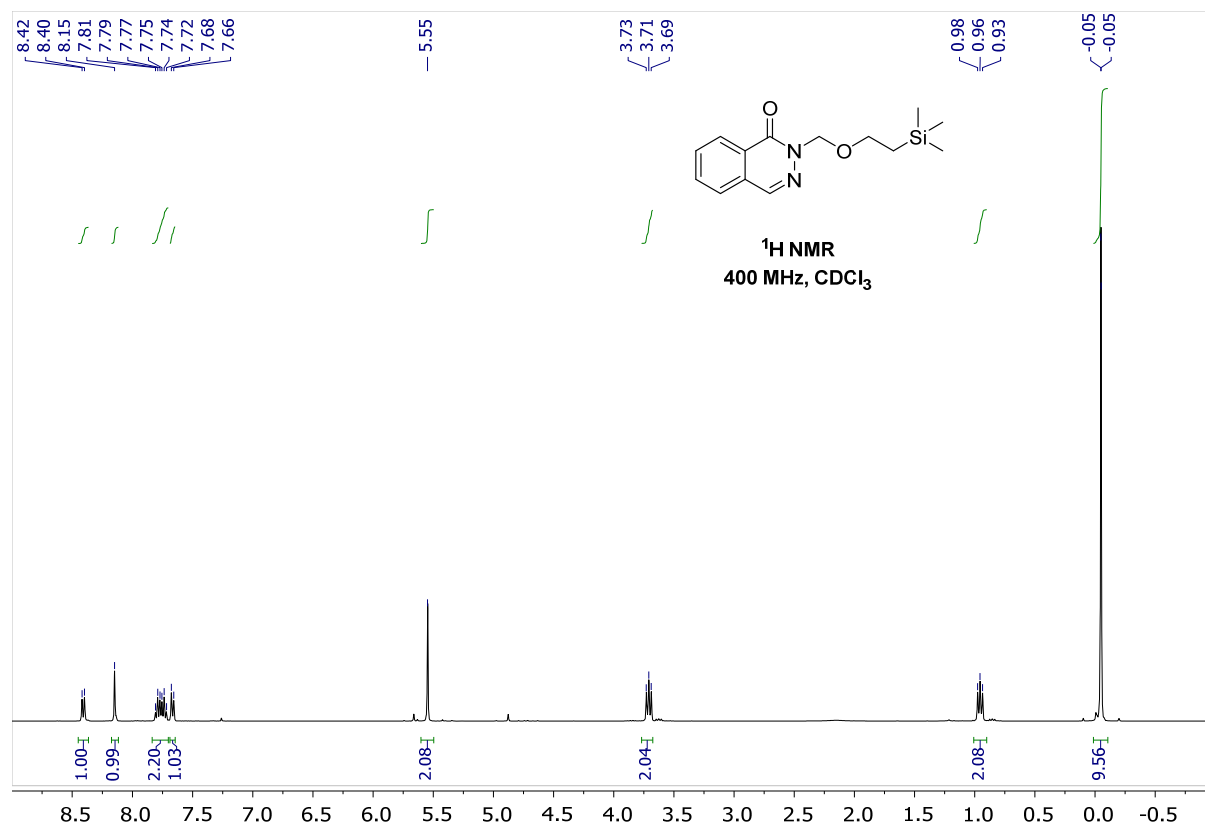


***tert*-Butyl 1-oxophthalazine-2(1*H*)-carboxylate**

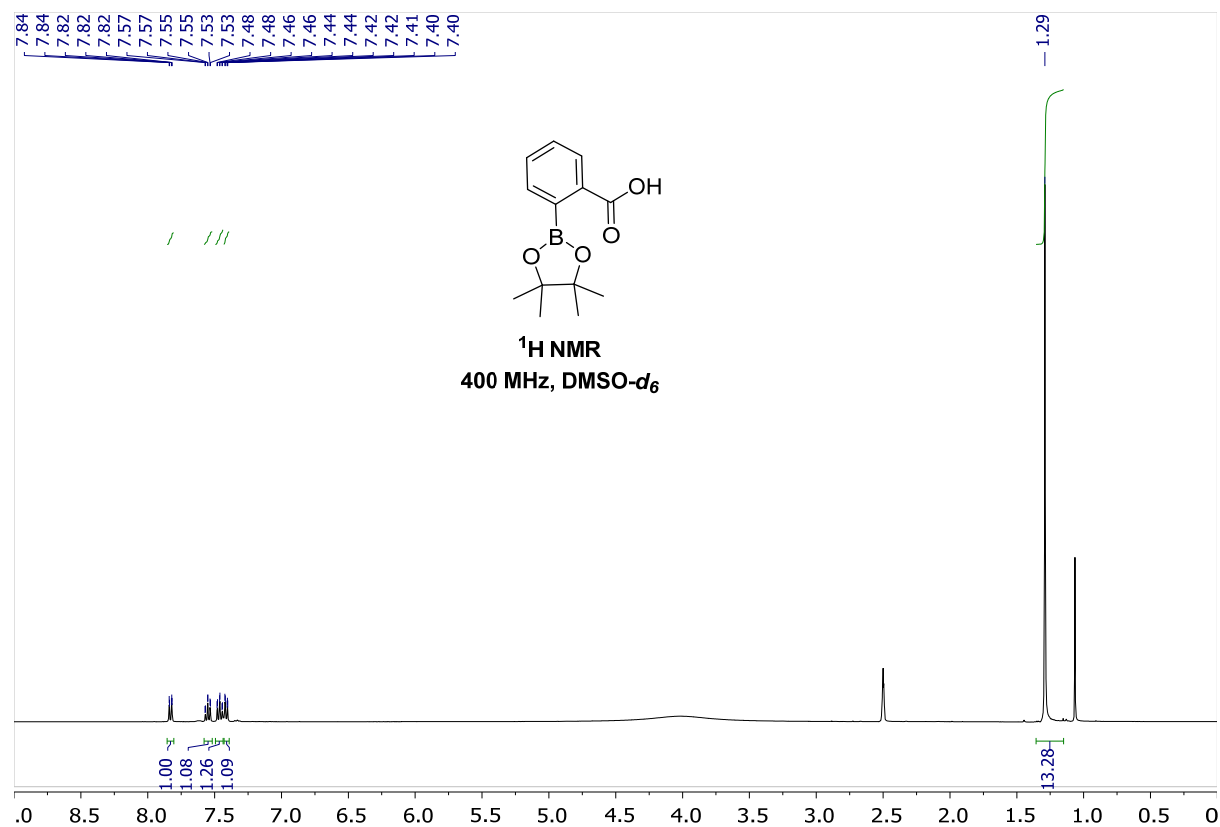


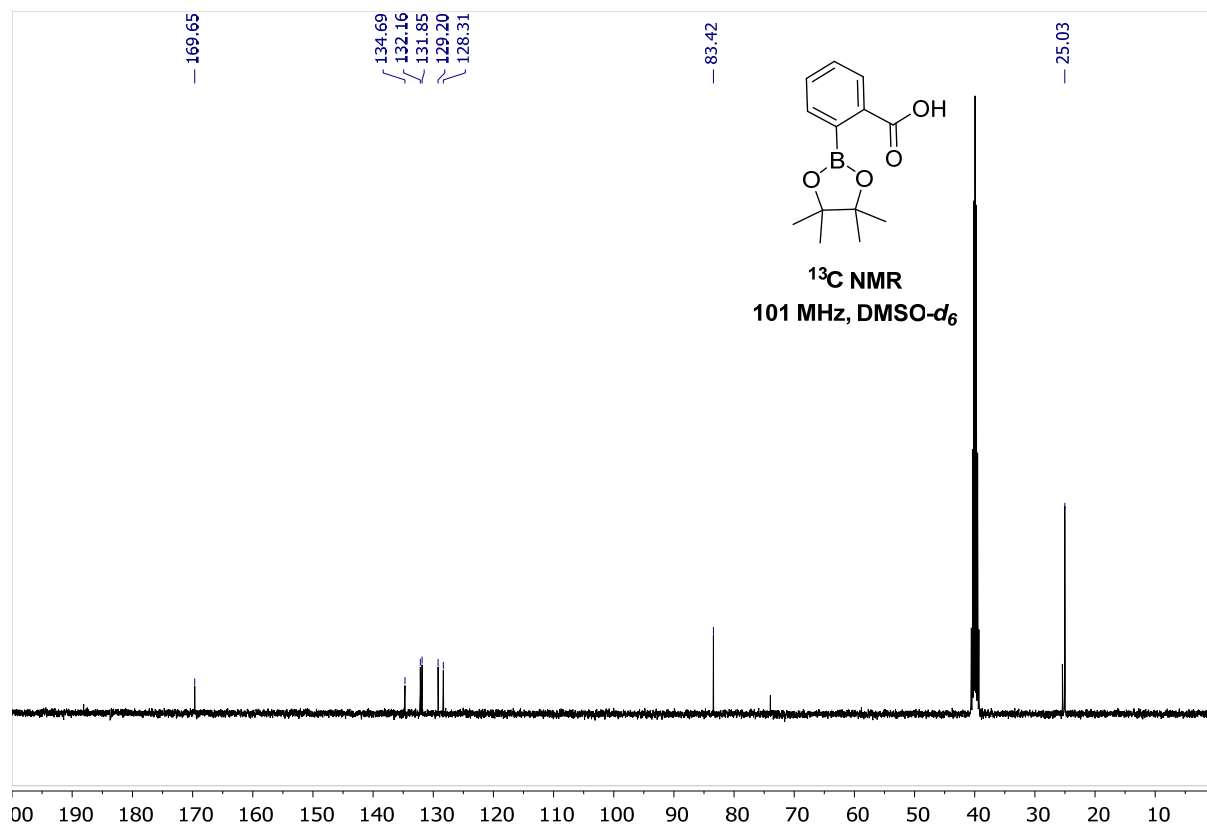


2-((2-triethylsilyl)ethoxymethyl)phthalazin-1(2H)-one

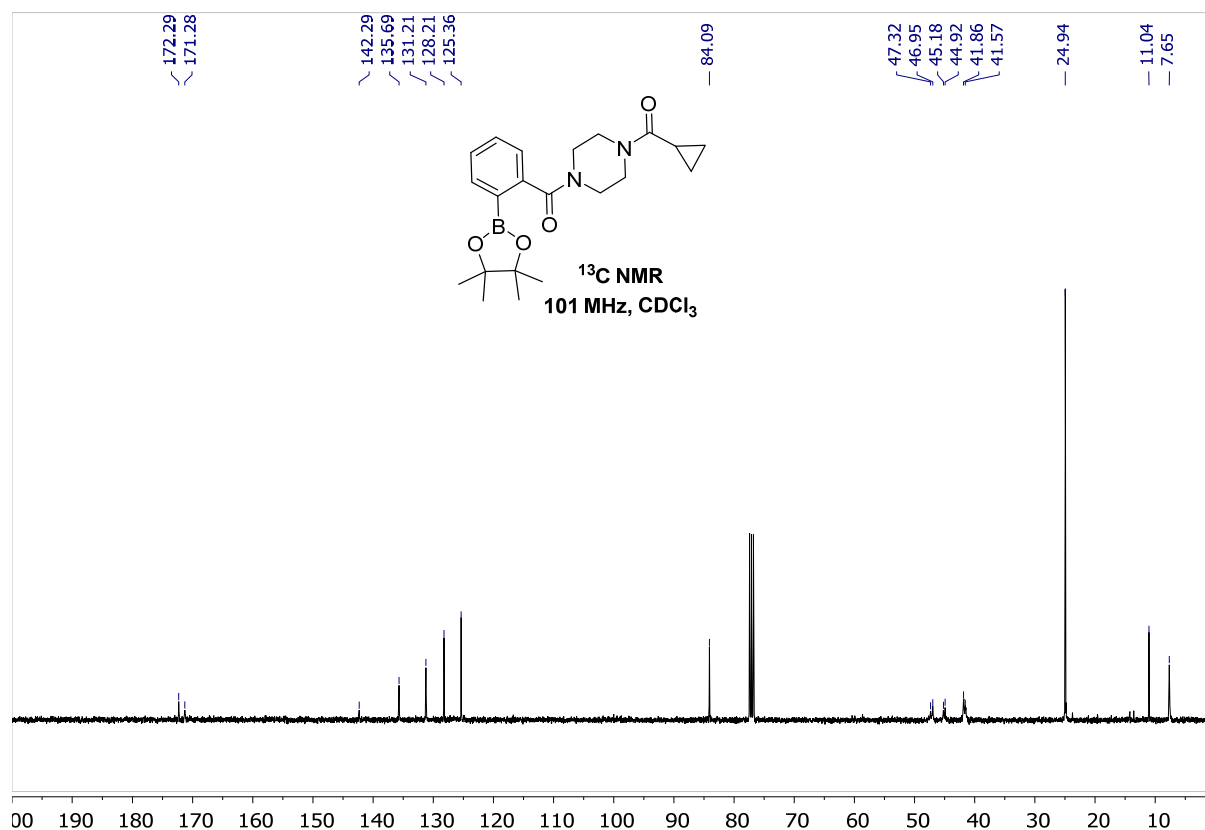
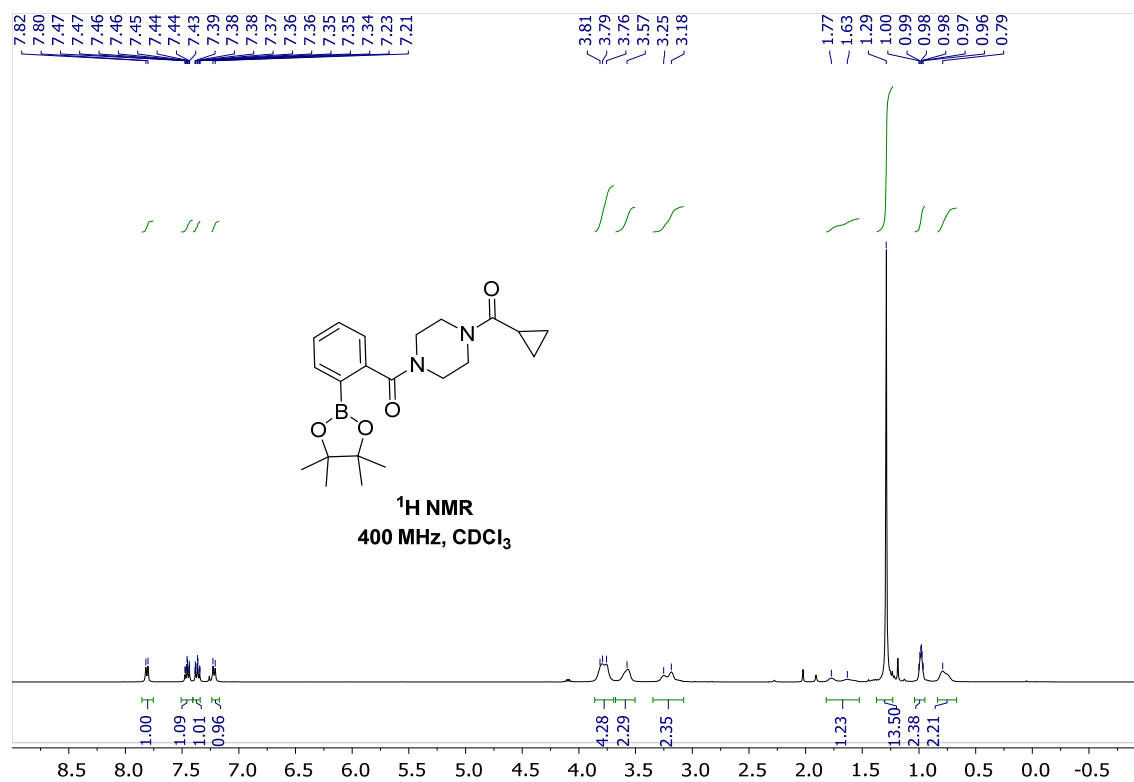


2-(4,4,5,5-Tetramethyl-1,3,2-dioxaborolan-2-yl)benzoic acid

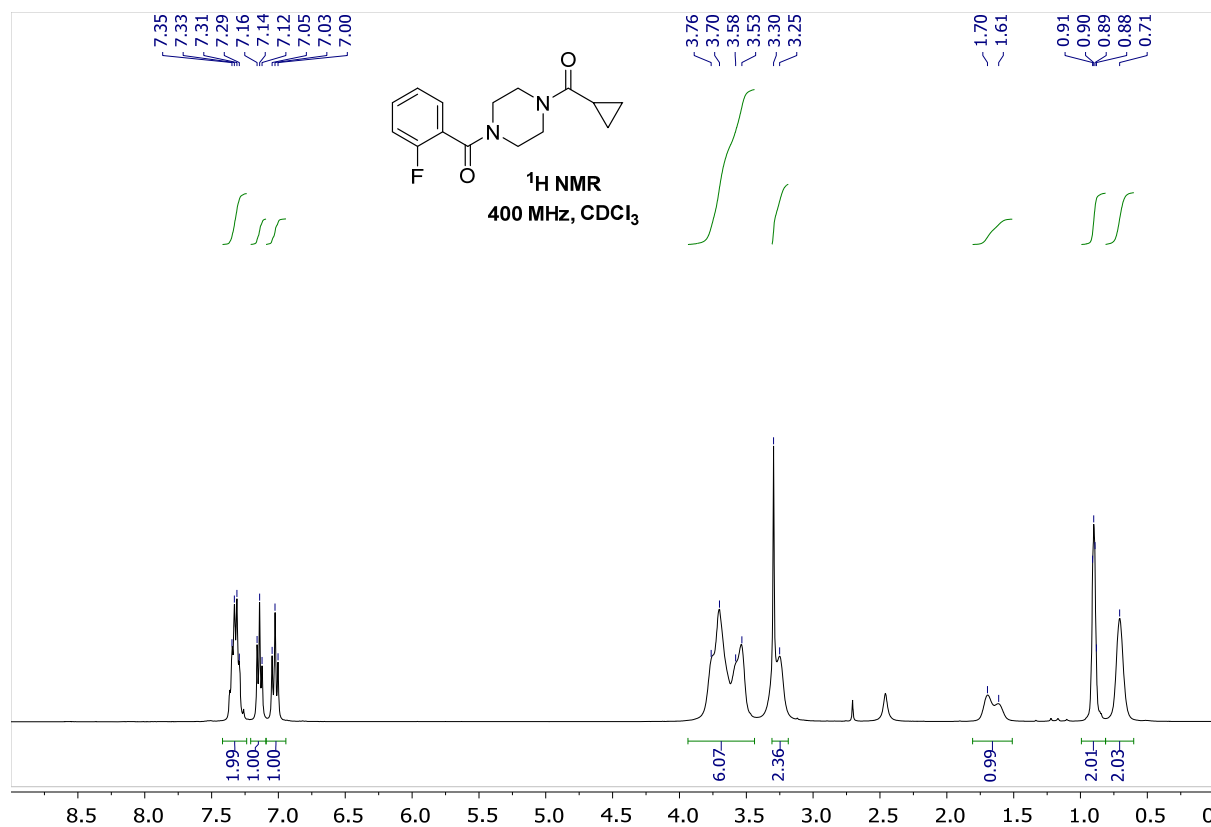


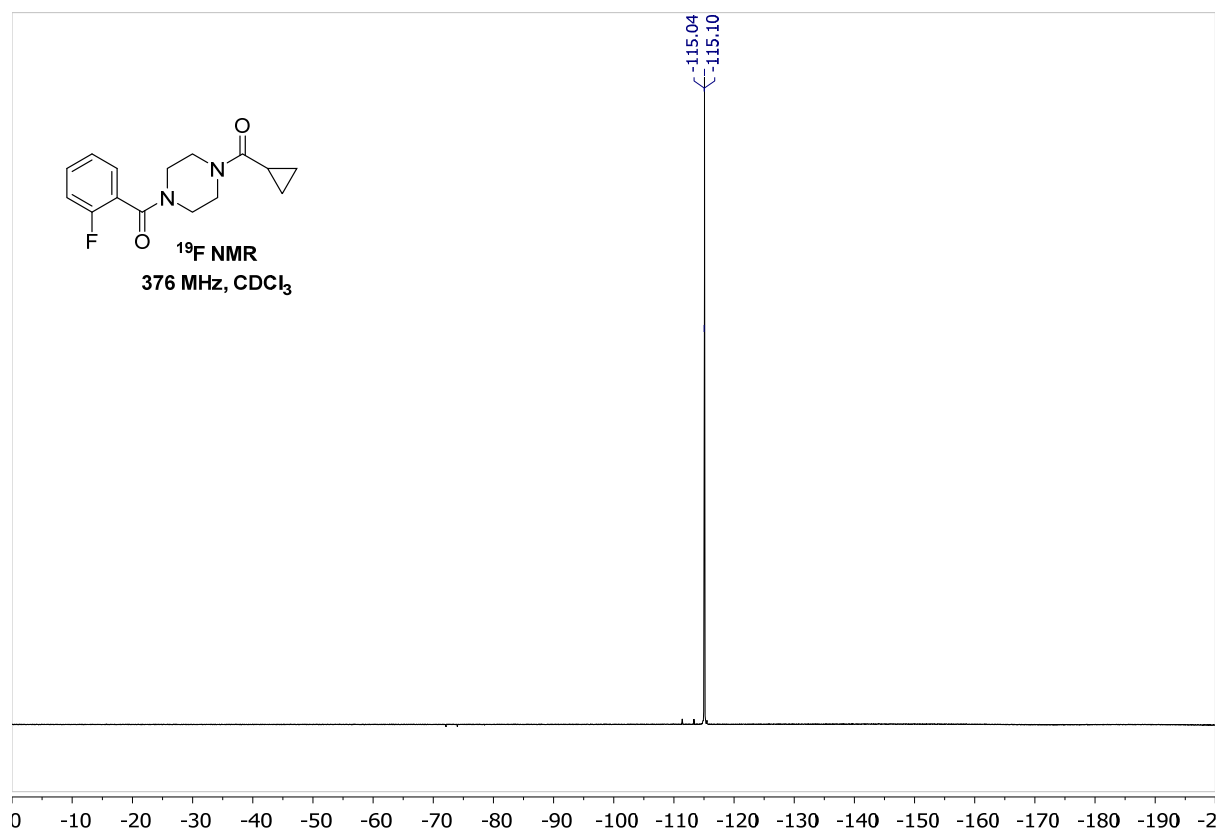
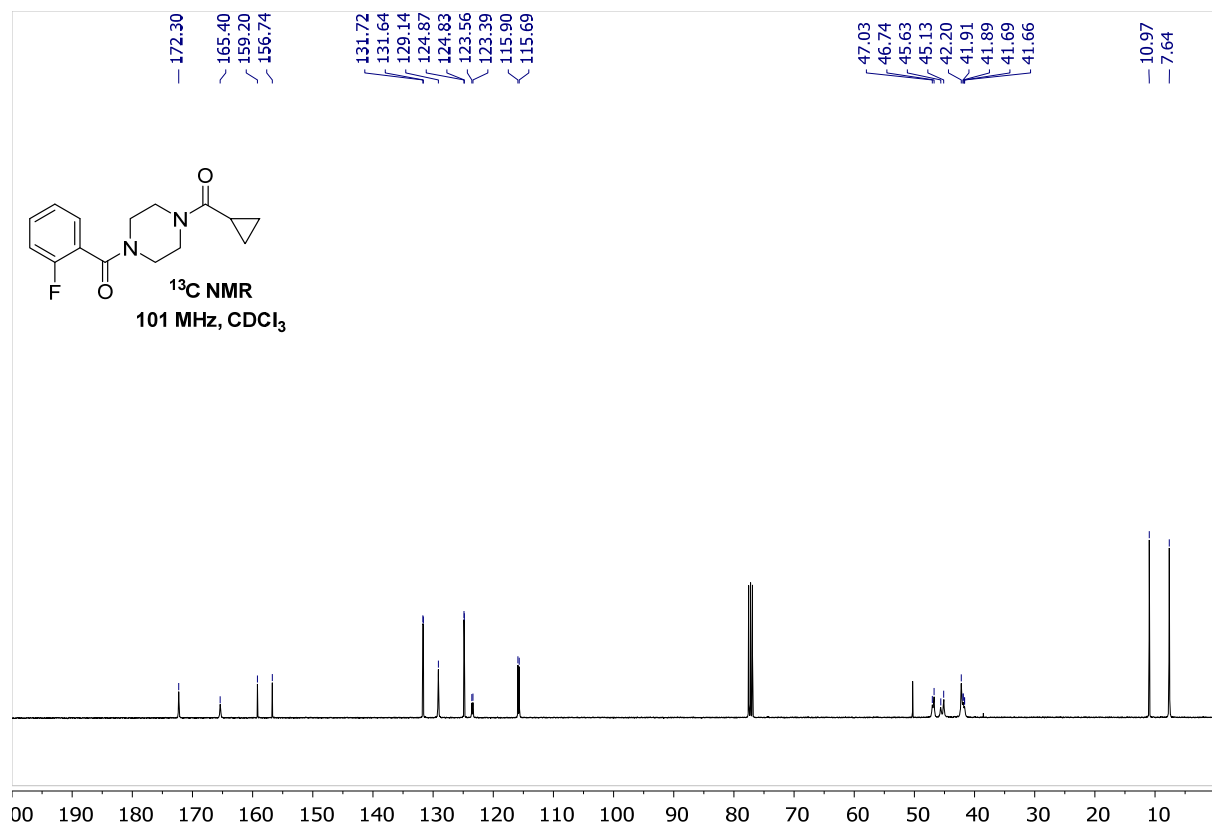


(4-(Cyclopropanecarbonyl)piperazin-1-yl)(2-(4,4,5,5-tetramethyl-1,3,2-dioxaborolan-2-yl)phenyl)methanone

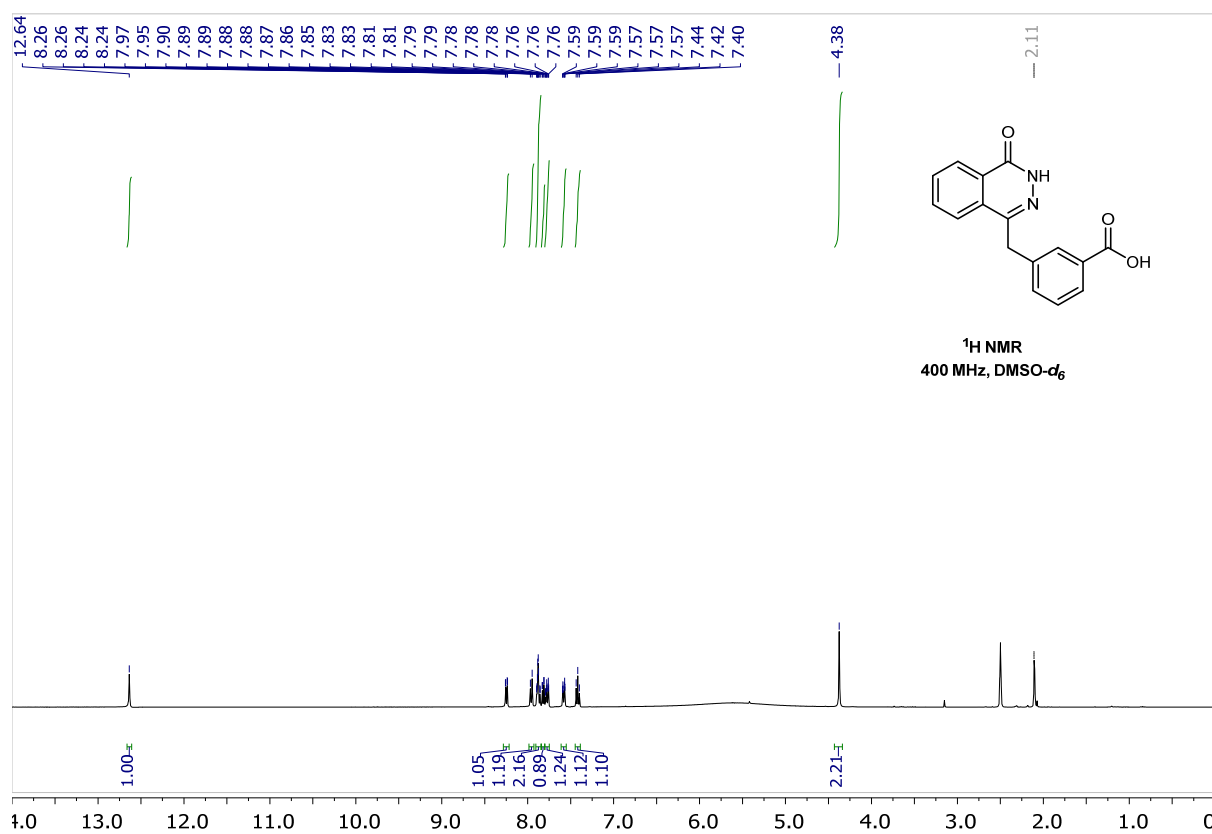


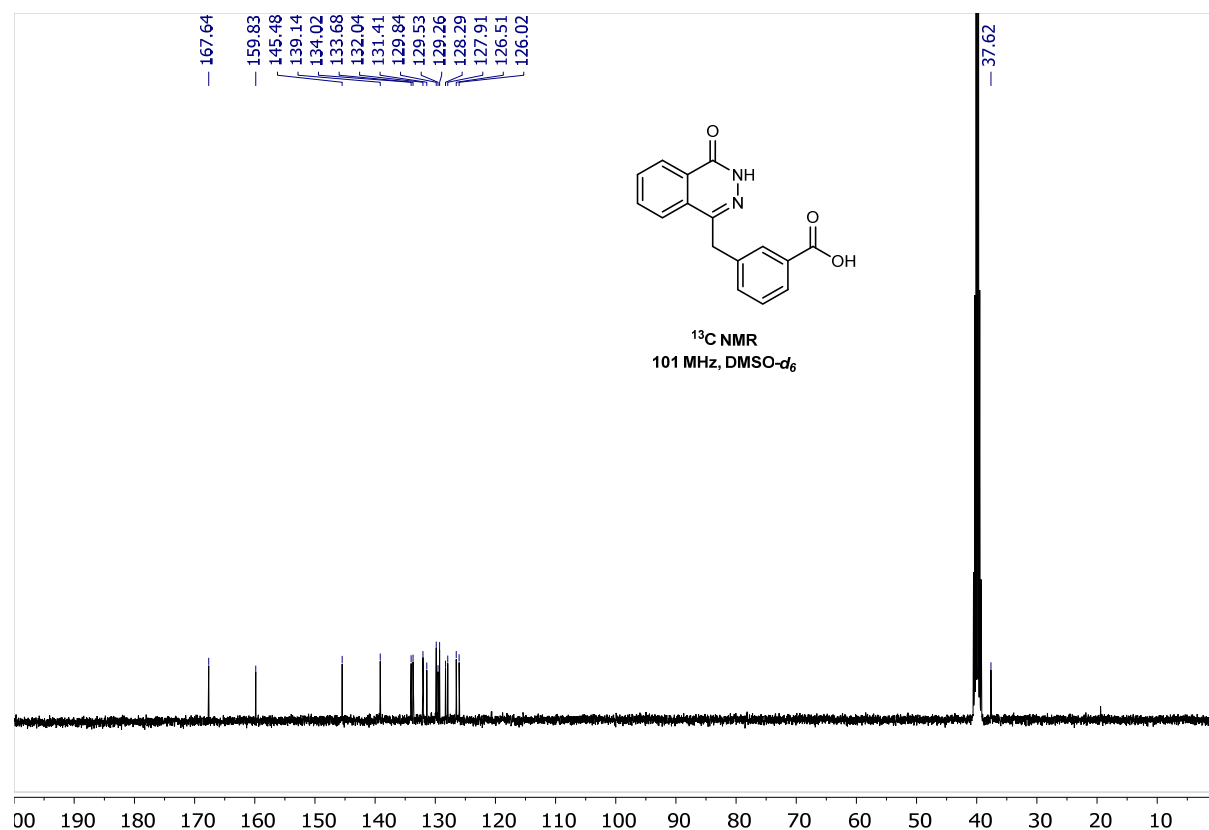
(4-(Cyclopropanecarbonyl)piperazin-1-yl)(2-fluorophenyl)methanone

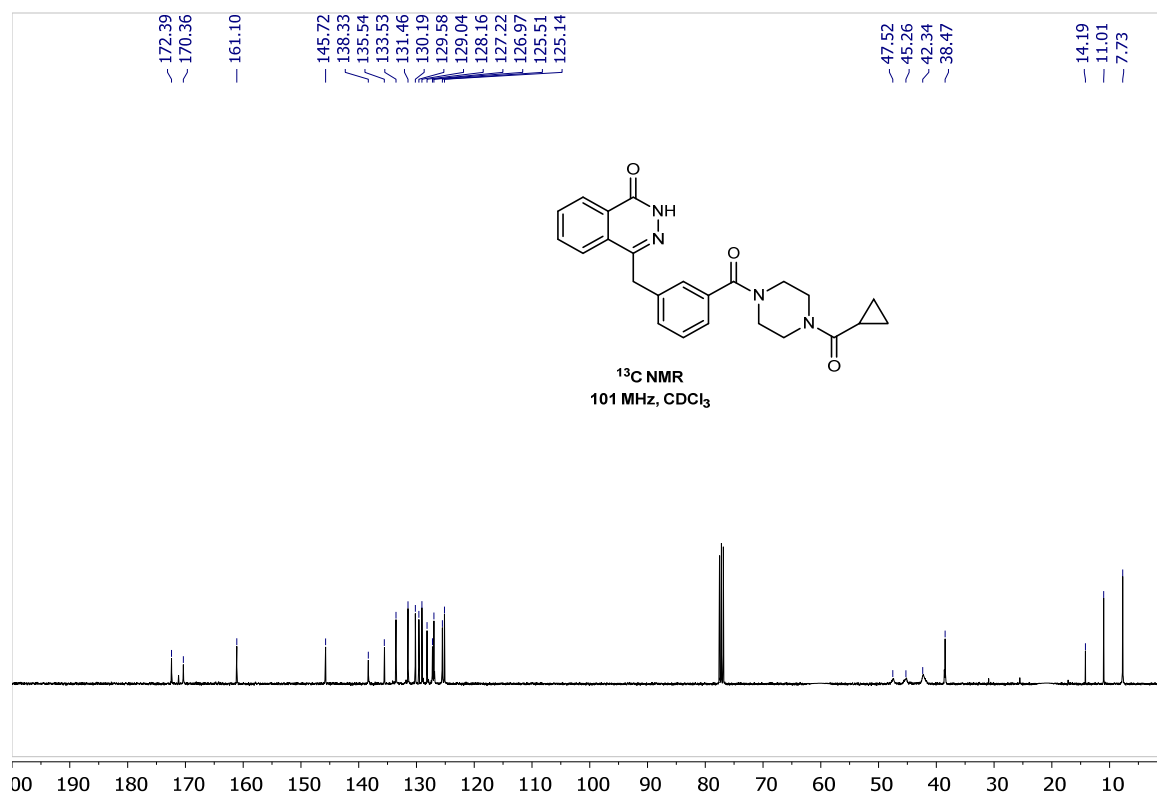
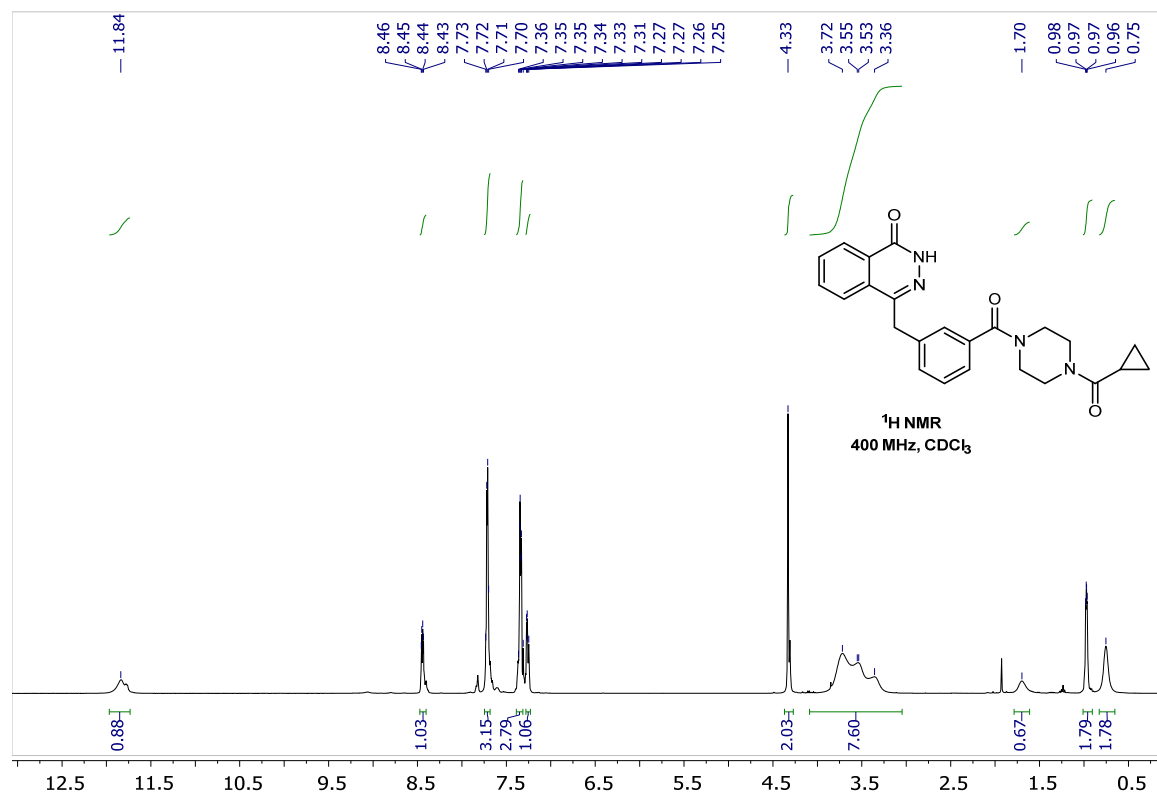




3-((4-oxo-3,4-dihydrophthalazin-1-yl)methyl)benzoic acid





4-(3-(4-(cyclopropanecarbonyl)piperazine-1-carbonyl)benzyl)phthalazin-1(2H)-one

3. Supplemental Material: Biology

1. Cells

PSN-1, MiaPaCa-2, and Capan-1 human pancreatic duct adenocarcinoma cells were originally purchased from ATCC. Cells were maintained in Dulbecco's Modified Eagle Medium (DMEM), supplemented with 10% foetal bovine serum (FBS), 2 mM L-glutamine, 100 units/mL penicillin, and 0.1 mg/mL streptomycin. Cells were grown in a 37°C environment containing 5% CO₂ and were harvested and passaged as required using Trypsin-EDTA solution. Cells were authenticated by the provider and the cumulative length of culture was less than 6 months following retrieval from liquid nitrogen storage. Cells were regularly tested to confirm the absence of mycoplasma contamination. Capan-1 cells used in this study were subsequently found by STR profiling not to match with the ATCC-held profile. However, low PARP enzyme expression was confirmed by Western blot and immunohistochemistry.

2. Western Blot

Western blot probing for PARP-1 was performed after cells were exposed to external beam radiation (0 or 10 Gy; ¹³⁷Cs source, using a using an IBL-637 ¹³⁷Cs irradiator, Cisbio International; 1 Gy/min) with 2 or 24 hours recovery.

Total protein preparations were produced at 4°C on approximately 1×10⁷ cells using RIPA lysis buffer (50 mM Tris, pH 8, 1% NP40, 0.5% sodium deoxycholate, 0.1% sodium dodecyl sulphate, 150 mM sodium chloride, cOmplete™ protease inhibitor cocktail [Sigma-Aldrich]). The cell lysates were isolated by centrifugation after lysis through a 21G hypodermic syringe and 30 second sonication. Thirty microgram lysate samples were run on a 4-12% Bis-Tris MES gel (Novex), transferred to a PVDF membrane and exposed to a 1:500 dilution of anti-PARP-1 antibody (Proteintech 13371-ap-1, lot 00045356) or anti-PGP-1 (abcam 170904, 1:2000), followed by a 1:3000 dilution of the secondary goat anti-rabbit-HRP (Bio-Rad). The membrane was exposed to autoradiography film after development using an ECL western blot substrate solution (Pierce Thermo Scientific 32209). β-actin was used as the loading control.

3. Immunocytochemistry

Cells were plated onto 8-chamber slides (Falcon CultureSlides) at 7×10⁴ cells per chamber in 0.75 mL culture media and incubated overnight in a 37°C CO₂ incubator until approximately 80% confluent. The slides were briefly in phosphate-buffered saline (PBS) pH7.4, and the cells fixed in 4% formaldehyde/PBS for 10 min. The slides were washed in PBS for 3 x 5 minutes, and cells permeabilized in 0.5% Triton X100

(Sigma) for 10 min. The cells were washed as before and non-specific binding was blocked by incubation of the slides in 2% BSA/PBS for 1 hour. To each appropriate section approximately 100µl primary antibody diluted 1:100 and 1:250 in 2% BSA/PBS, or just 2% BSA/PBS, was applied, and incubated in a humid chamber for 2 hours. The primary antibodies used was anti-PARP-1 rabbit polyclonal (ProteinTech 13371-ap-1). The slides were washed in PBS for 3 x 5 minutes, and the secondary goat-anti-rabbit IgG-594 antibody (Life Technologies Alexa Fluor, 1:500 dilution in 2% BSA/PBS), was applied and incubated for 1 hour. The slides were then washed in PBS for 3 x 5 minutes, excess fluid removed with a tissue, and a drop of Vectashield + DAPI (Vector Laboratories) was applied to each section. Finally a coverslip was gently lowered onto each slide, and Covergrip (Biotium) used to seal the coverslips. Prepared slides were stored at 4°C in the dark. The slides were analyzed using a Leica SP8 confocal fluorescent microscope.

4. Cell uptake experiments

Cell uptake of ^{18}F -olaparib in PSN-1, MiaPaCa-2 and Capan-1 cells was determined as previously described (8-10). Aliquots of cells (1.5×10^5 cells/well) were seeded in 24-well plates in warm cell culture medium (500 µL) and the cells were allowed to adhere overnight. Cells were irradiated (10 Gy; dose rate 0.8 Gy/min) or sham-irradiated and then returned to an incubator (37°C, 5% CO₂) for 2-48 h. The cell culture medium was then removed and cells were washed once with fresh cell culture medium (500 µL). In 500 µL of cell culture medium (not supplemented with FBS, L-glutamine, or penicillin/streptomycin), ^{18}F -olaparib (50 kBq) was added to each well and the cells were then incubated at 37°C. In the blocking groups, non-radioactive olaparib, talazoparib, or rucaparib were also added in increasing concentrations (10 pM - 10 µM). After 30 or 60 minutes, the cell culture medium was removed and combined with two washes (500 µL) of cell culture medium. The remaining monolayer of cells was then lysed with 0.1 M sodium hydroxide for 20 minutes at room temperature. The amount of radioactivity contained within the cell culture medium and the cell lysate fractions was measured using a gamma counter. Protein levels from parallel plates were quantified using a Pierce BCA protein assay kit (Thermo Scientific) according to the manufacturer's recommendations and bovine serum albumin was used as the protein standard. Cell uptake levels of ^{18}F -olaparib were normalized to percent of the total added radioactivity per milligram protein. These experiments were performed in triplicate on at least three separate occasions. IC₅₀ values were calculated using GraphPad Prism software (GraphPad Software, San Diego, CA, USA). Data are presented as mean ± SEM.

(Radiation dose dependency)

Aliquots of cells (7.5×10^4 cells/well) were seeded in 24-well plates in warm cell culture medium (500 μ L). After 4 h, cells were irradiated (0, 2, 4, 6, 8, or 10 Gy; dose rate 0.8 Gy/min) and then returned to an incubator (37°C, 5% CO₂). After 24 or 48 h, the cell culture medium was then removed and cells were washed once with fresh cell culture medium (500 μ L). In 500 μ L of cell culture medium (not supplemented with FBS, L-glutamine, or penicillin/streptomycin), ¹⁸F-olaparib (50 kBq) was added to each well and the cells were then incubated at 37°C. In the blocking groups, non-radioactive olaparib was also added to each well to achieve a concentration of 10 μ M. After 30 minutes, the cell culture medium was removed and combined with two washes (500 μ L) of cell culture medium. The remaining monolayer of cells was then lysed with 0.1 M sodium hydroxide for 20 minutes at room temperature. The amount of radioactivity contained within the cell culture medium and the cell lysate fractions was measured using a gamma counter. Protein levels from parallel plates were quantified using a Pierce BCA protein assay kit (Thermo Scientific) according to the manufacturer's recommendations and bovine serum albumin was used as the protein standard. Radiotracer cell uptake levels were normalized to percent of the total added radioactivity per milligram protein.

5. *In vivo* tumor models

All animal procedures were performed in accordance with the UK Animals (Scientific Procedures) Act 1986 and with local ethical committee approval. Animals were housed in IVC cages in sex-matched groups up to 5 per cage, in an artificial day-night cycle facility, with ad libitum access to food and water.

(PSN-1 and Capan-1)

Cells were harvested using trypsin, washed twice using PBS, and reconstituted in DMEM. PSN-1 or Capan-1 xenograft tumors were established in the right hind flank of female NOD/SCID mice (Charles River, UK) by subcutaneous injection of 1×10^6 cells in PBS:matrigel (150 μ L). Tumor volumes (V) were calculated after calliper measurement using the following equation: $V = (a^2 \times b)/2$, where a is the width of the tumor and b the length (small and large diameters, respectively). The individual relative tumor volume (RTV) was defined as V_t/V_0 , where V_t is the volume at a given time and V_0 at the start of treatment. Animals were entered in *in vivo* studies when their tumor was at least 200 mm³.

(CaNT)

The murine adenocarcinoma NT (CaNT) was implanted subcutaneously onto the right thigh of 6-7 week-old female CBA/Carl mice. Fifty μL of a crude cell suspension, prepared by mechanical dissociation of an excized tumor from a donor animal, was injected. Tumors were selected for imaging when the geometric mean diameter reached 6-8 mm (volumes calculated as above), approximately 3 weeks after implantation (11).

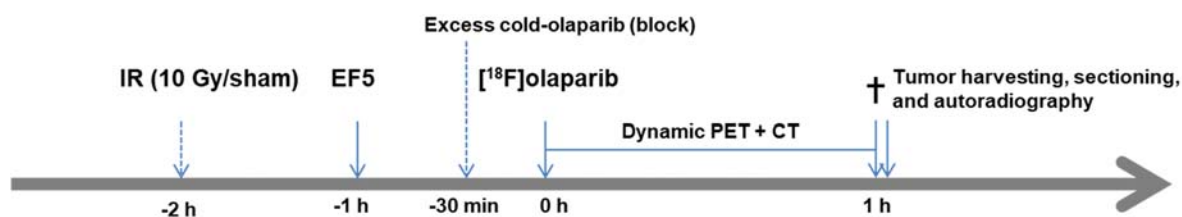
(Irradiation of tumors)

Irradiation of subcutaneous tumor xenografts was performed using a Gulmay 320 kV system (2.0 Gy/min). A dose of 10 Gy was delivered to the tumor using 300 kV X-rays (Gulmay 320kV irradiator; 2 Gy/min). The radiation set-up allowed irradiation of the right hind quarter, including the tumor and right leg, only. Control mice were anesthetized and sham-irradiated for the same length of time. Irradiation was performed 2 hours prior to administration of ^{18}F olaparib (see figure 3a, here repeated for clarity).

6. PET/CT Imaging

(^{18}F -olaparib PET imaging)

Two hours prior to PET/CT imaging, animals were exposed to X-irradiation of the tumor (10 Gy or sham) (see schedule below). Radiation was delivered using a Gulmay 320 kV X-irradiator; 2.0 Gy/min. Anesthesia was maintained at 2.5 % isoflurane throughout the duration of the irradiation, and animals were allowed to recover. To study the relationship of PARP-1 expression, ^{18}F -olaparib uptake and hypoxia, the same animals were administered EF5 (0.6 μg in 200 μL 0.9% saline) intraperitoneally, one hour prior to PET/CT imaging. Some animals were administered an excess of cold, unlabelled olaparib (0.5 mg in 250 ml 10%DMSO (v/v) in PBS), intravenously, 30 minutes prior to administration of ^{18}F -olaparib. Naïve CBA/Carl mice, not bearing tumors, were not irradiated, nor was EF5 administered.



Dynamic PET/CT images were acquired using a VECTOr⁴CT integrated PET/CT system. Mice were anesthetized by 4% isoflurane gas (0.5 L/min O_2) and placed on a custom-built imaging cradle in a prone position. Animals were intravenously injected with ^{18}F -olaparib or (3-5 MBq, 8-11 GBq/ μmol , through a

tail vein catheter, and dynamic imaging was performed over 45-60 min after radiolabeled compound administration. PET acquisition (150 s per frame, using list mode acquisition) using an ultra-high resolution rat/mouse 1.8 mm collimator, followed by a cone-beam CT scan (55 kV, 0.19 mA) for anatomical reference and attenuation correction. Anesthesia was maintained at 2.5 % isoflurane throughout the duration of the image acquisition. PET images were reconstructed using U-SPECT-Rec3.22 software (MILabs, Utrecht, The Netherlands), applying a pixel-based algorithm with 8 subsets, 6 iterations and 0.8 mm voxel size for ^{18}F (energy window settings 477.9-584.1 keV).

(image analysis)

Reconstructed images were viewed and analyzed using PMOD v.3.37 (PMOD Technologies, Zurich, Switzerland). The radioactivity in each volume of interest was calculated as percent injected dose per cubic cm (%ID/mL).

7. *Ex vivo* biodistribution

After PET/CT image acquisition, animals were euthanized by cervical dislocation and selected organs, tissues and blood were removed. The amount of radioactivity in each organ was measured using a 2480 WIZARD² gamma counter (PerkinElmer). Counts per minute were converted into MBq using a calibration curve generated from known standards. Values were decay-corrected to the time of injection, and the percentage of the injected dose per gram (%ID/g) of each tissue was calculated.

8. *Ex vivo* analysis

(Autoradiography)

After imaging and automated gamma counting, selected tissues from mice were flash-frozen with dry ice. If required, samples were stored at -80°C overnight. Frozen tissue was sectioned (8 µm) using an OTF5000 cryotome (Bright Instruments Ltd). Tissue sections were thaw-mounted onto Superfrost PLUS glass microscope slides (Menzel-Glaser, Thermo Scientific) and allowed to dry at room temperature. The slides were then exposed to a storage phosphor screen (PerkinElmer, Super Resolution, 12.5 x 25.2 cm) in a standard X-ray cassette for 15 h at 4°C or -20°C. The phosphor screen was then imaged using a Cyclone[®] Plus Storage Phosphor System (PerkinElmer) and images were analyzed with OptiQuant 5.0 (PerkinElmer) and ImageJ (NIH).

(Immunohistochemistry)

PARP-1 staining:

PSN-1 xenografts harvested from mice were flash frozen and 8 μ m sections were prepared using a cryostat. Sections were stored at -80°C until use. Slides were allowed to reach room temperature (10 minutes), then washed briefly in phosphate-buffered saline (PBS) pH7.4. The slides were fixed in 4% formaldehyde/PBS for 10 min, then washed three times in PBS for 5 min. Sections were permeabilized in 0.5% Triton X100 (Sigma) for 10 min, washed, and non-specific binding was blocked by incubation of the slides in 2% BSA/PBS for 1 h. Slides were briefly allowed to dry and each section was isolated using a PAP pen (Sigma). To each appropriate section approximately 100 μ l primary anti-PARP-1 polyclonal antibody (ProteinTech 13371-AP-1) diluted 1:250 in 2% BSA/PBS, or just 2% BSA/PBS, was applied, and incubated in a humid chamber overnight at 4°C. The slides were washed three times in PBS for 5 min, and the secondary goat-anti-rabbit IgG-488 antibody (Life Technologies Alexa Fluor, 1:500 dilution in 2% BSA/PBS), was applied and incubated for 1 h. The slides were then washed in PBS, excess fluid removed, mounted using Vectashield containing DAPI (Vector Laboratories). Slides were stored at 4°C in the dark. Images were acquired using a Leica SP8 confocal fluorescent microscope.

EF5 staining:

Tumor hypoxia was confirmed by immunohistological staining for EF5 (2-(2-nitro-1H-imidazol-1-yl)-N-(2,2,3,3,3-pentafluoropropyl)-acetamide). For EF5 studies, mice were administered with 10 mM EF5 in 0.9% saline i.v. 2 h prior to tumor excision (EF5 was obtained from Dr. Cameron Koch, University of Pennsylvania (12)). To determine the correlation between ¹⁸F-olaparib uptake and hypoxia, tumor slices were analyzed by both autoradiography and EF5 IHC (13) (11) (14). Object-based overlap between both modalities was determined by first co-registering autoradiography and fluorescence microscopy images using a rigid transformation. Then, Manders' overlap coefficients (M1) were calculated using the JACoP plug-in for Image J (methods of Manders for spatial intensity correlation analysis with Costes method for automatic thresholding).

9. Statistical methods

All statistical analyses and nonlinear regression were performed using GraphPad Prism (GraphPad Software, San Diego, CA, USA). Data were tested for normality and analyzed either by the unpaired, two-tailed Student's t-test where appropriate, or 1-way analysis of variance (ANOVA) for multiple

comparisons, with Dunnet's post-tests to calculate significance of differences between groups. All data were obtained at least in triplicate and results reported as mean \pm standard deviation, unless stated otherwise.

10. Supplemental tables: biodistribution data

Supplemental Table 4: *Ex vivo* biodistribution ^{18}F -olaparib in naïve CBA/Carl mice.

	%ID/g		
Blood	0.11	0.11	0.14
Heart	0.19	0.17	0.34
Lung	0.29	0.19	0.34
Liver	2.55	4.02	5.27
Spleen	2.09	1.91	3.68
Stomach	0.46	0.26	0.58
Large intestine	0.92	1.64	2.99
Small intestine	7.75	10.33	17.40
Pancreas	0.91	0.70	1.30
Kidney	0.59	0.60	1.01
Muscle	0.20	0.14	0.34
Skin	0.16	0.10	0.27
Fat	0.05	0.03	0.26

Supplemental Table 5: *Ex vivo* biodistribution ^{18}F -olaparib in PSN-1 xenograft bearing mice.

	^{18}F -olaparib						^{18}F -olaparib + IR (10 Gy)			^{18}F -olaparib + block			
Blood	0.41	0.73	0.57	0.24	0.21	0.19	0.63	0.83	1.17	2.12	2.29	2.51	1.06
Tumor	1.94	4.07	4.20	3.27	2.43	3.07	6.43	3.03	6.59	1.68	0.92	1.09	1.09
Heart	3.18	2.05	1.74	1.58	0.85	1.07	3.14	2.49	2.88	1.98	1.59	1.51	0.78
Lung	4.68	3.51	3.18	2.15	1.45	1.69	3.94	4.47	4.47	1.61	1.40	1.32	0.74
Liver	26.2	34.6	27.0	21.0	13.5	18.0	25.1	33.8	45.7	29.1	32.9	22.4	23.1
Spleen	17.5	13.7	11.3	14.0	7.36	8.01	45.0	20.5	14.3	1.62	1.46	1.24	0.69
Stomach	2.59	3.53	1.81	1.80	0.55	0.60	4.15	0.92	0.87	1.44	0.79	0.46	0.21
Large intestine	12.6	30.5	80.8	27.0	28.9	6.61	27.5	28.9	16.2	20.1	13.3	61.4	12.7
Small intestine	54.5	58.1	30.6	31.9	18.6	26.6	65.1	113	95.2	89.9	77.2	96.4	132
Pancreas	8.49	9.38	7.25	5.52	2.78	4.24	13.6	10.3	11.4	1.92	2.29	1.91	1.79
Kidney	10.5	7.95	6.02	7.04	3.41	3.66	10.0	9.25	10.6	13.1	5.09	3.98	2.44
Muscle	1.60	1.40	1.45	1.12	0.70	0.73	3.71	2.01	1.76	1.58	1.08	1.18	0.65
Bone	3.38	4.54	2.71	1.88	1.26	1.50	9.12	4.13	3.81	1.06	0.78	0.80	0.46
Skin	1.50	1.75	2.06	1.25	0.87	1.14	2.10	2.38	2.66	1.65	1.09	1.10	0.66
Fat	0.97	0.82	0.68	0.45	0.44	0.37	0.66	1.41	0.82	0.53	0.62	0.35	0.19

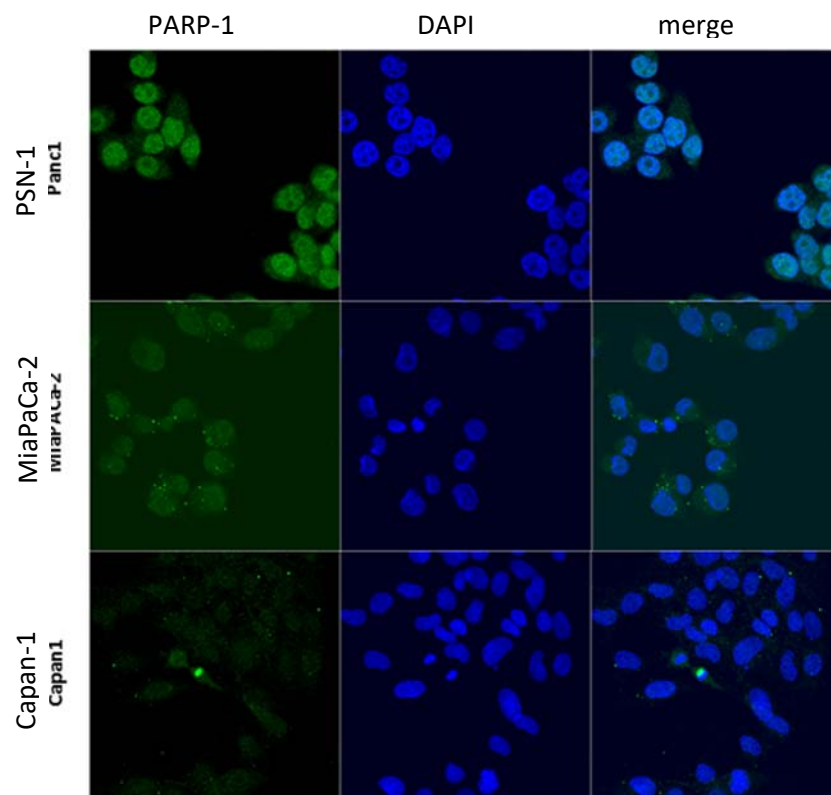
Supplemental Table 6: *Ex vivo* biodistribution ^{18}F -olaparib in Capan-1 xenograft bearing mice.

	^{18}F -olaparib				^{18}F -olaparib + IR (10 Gy)			^{18}F -olaparib + block		
Blood	0.30	0.23	0.31	0.72	0.86	0.43	1.16	0.25	0.27	0.56
Tumor	2.48	3.21	2.94	1.73	1.85	1.70	2.48	1.27	1.04	0.69
Heart	1.75	0.87	1.81	2.24	0.92	0.48	0.80	0.53	1.62	1.83
Lung	2.60	1.49	2.66	3.97	0.83	0.60	0.85	0.90	2.04	1.86
Liver	11.78	5.79	10.32	22.63	9.16	5.93	6.67	3.62	6.88	9.79
Spleen	9.84	6.13	8.40	15.10	0.77	0.73	0.82	2.80	7.93	6.43
Stomach	1.55	0.63	1.14	3.42	0.38	0.36	0.64	0.30	0.49	0.94
Large intestine	4.99	4.50	4.14	8.14	5.21	3.30	5.86	2.91	4.06	5.00
Small Intestine	12.27	17.29	11.58	13.70	15.58	9.80	19.97	0.45	11.70	46.04
Pancreas	9.32	8.12	7.87	13.16	1.89	1.59	1.84	4.56	10.82	10.22
Kidney	4.32	2.05	4.91	5.22	4.66	1.03	3.67	1.26	3.32	4.16
Muscle	0.65	0.45	0.63	1.44	0.63	0.29	0.48	0.28	0.65	0.88
Bone	1.46	0.98	1.26	3.08	0.31	0.16	0.19	0.47	1.27	2.17
Skin	0.02	0.55	0.77	1.54	0.67	0.23	0.33	0.14	0.46	1.16
Fat	0.46	0.19	0.27	0.69	0.24	0.13	0.19	0.22	0.77	0.36
Brain	0.82	0.03	0.03	0.10	0.06	0.03	0.03	0.03	0.03	0.04
Caecum	5.11	4.35	3.31	24.11	7.58	4.46	5.92	9.13	4.00	5.07
Gallbladder	81.02	24.53	34.02	446.94	68.68	31.81	36.90	105.86	35.11	88.82

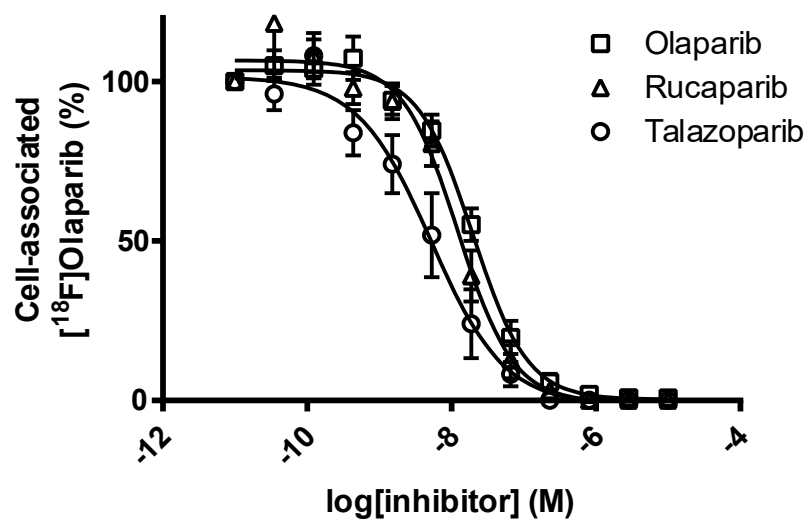
Supplemental Table 7: *Ex vivo* biodistribution ^{18}F -olaparib in CaNT allograft bearing CBA/Carl mice.

	^{18}F -olaparib		^{18}F -olaparib + IR (10 Gy)		^{18}F -olaparib + block
Blood	1.78	8.00	9.79	3.12	4.00
Tumor	1.48	2.83	1.43	1.92	0.98
Heart	7.34	0.00	8.74	7.03	2.51
Lung	12.5	9.73	10.9	9.61	2.29
Liver	84.6	110	93.2	100	74.3
Spleen	43.3	47.0	69.0	58.3	2.41
Stomach	6.17	12.8	9.40	4.20	4.09
Large intestine	24.0	47.8	60.1	47.0	61.2
Small intestine	200	279	455	190	603
Pancreas	15.1	20.8	29.5	23.6	3.41
Kidney	23.9	21.0	24.5	19.0	8.45
Muscle	5.84	4.63	5.45	5.31	2.65
Bone	11.7	10.2	15.7	11.5	5.18
Skin	3.82	4.65	5.02	5.12	1.16
Fat	7.19	1.12	2.52	2.34	1.57
Brain	0.29	0.23	0.20	0.25	0.22
Caecum	32.5	56.2	42.9	44.6	101
Gallbladder	953	126	155	57.3	194

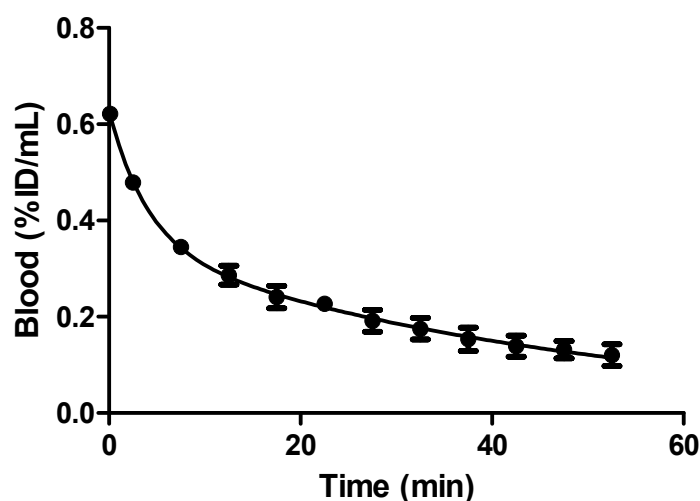
11. Supplemental Results



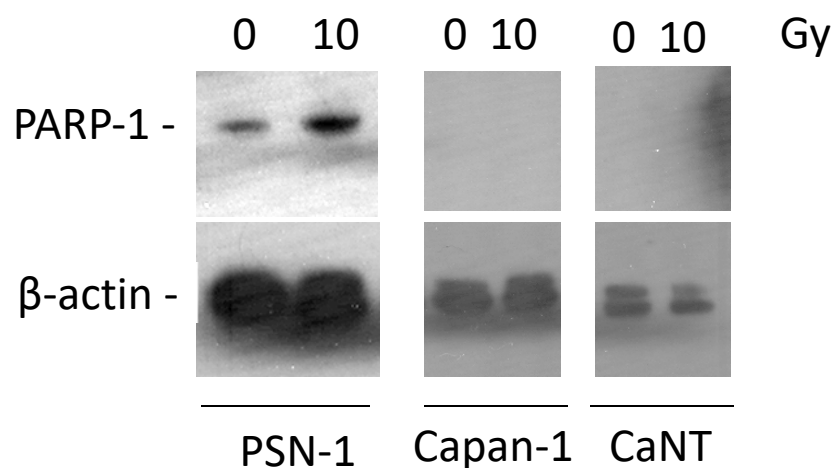
Supplemental Fig 8: Immunocytochemistry of PARP-1 in a selection of PDAC cell lines.



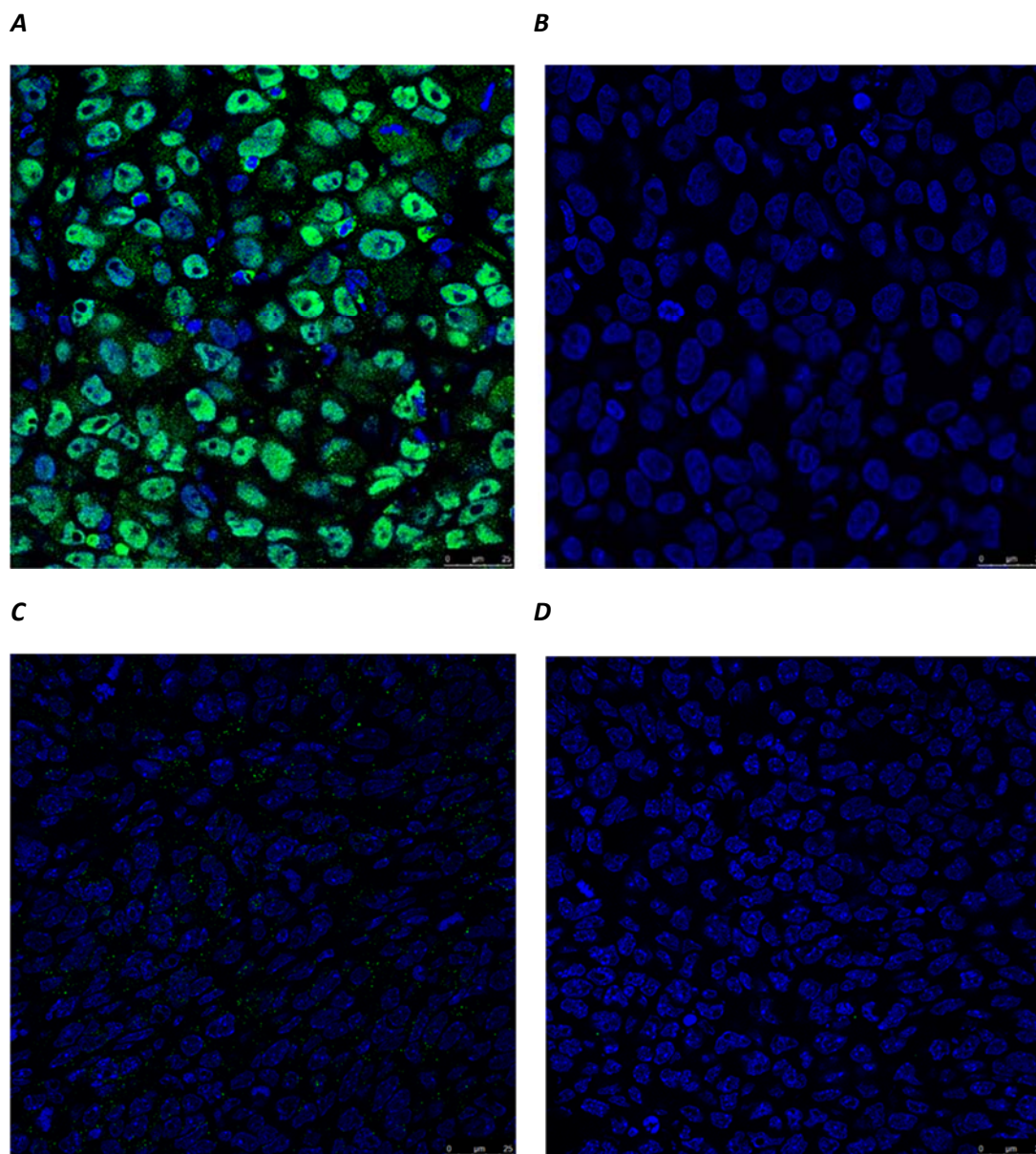
Supplemental Fig 9: Displacement of ^{18}F -olaparib uptake in PSN-1 cells by a selection of several PARP inhibitors.



Supplemental Fig 10: Concentration of ^{18}F -olaparib in blood of naïve CBA/Carl mice.

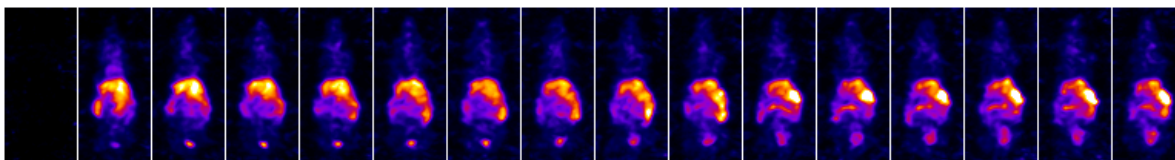


Supplemental Fig 11: Western blot of xenograft tumor tissue from PSN-1, Capan-1, and CaNT tumors, after irradiation (10 Gy) or sham-irradiation (0 Gy). Xenografts from randomly selected animals were analyzed.

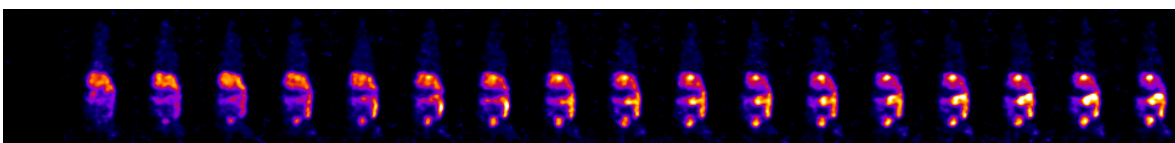


Supplemental Fig 12: Immunohistochemistry staining for PARP-1 on xenograft tumor tissue from PSN-1 (A), CaNT tumors (C). Controls using only secondary antibody showed minimal non-specific staining (B, D).

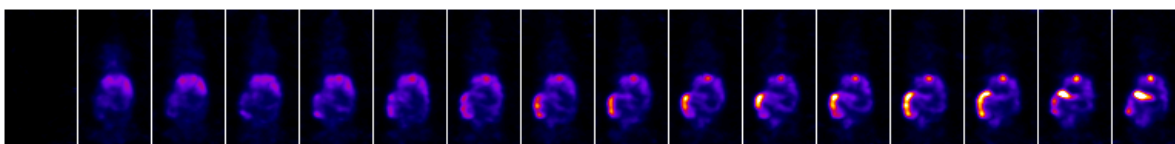
A



^{18}F -olaparib

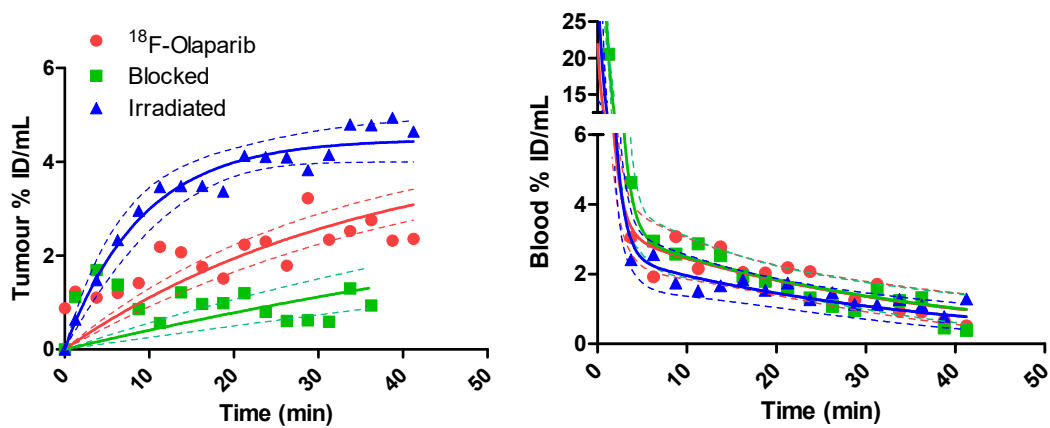


+ IR

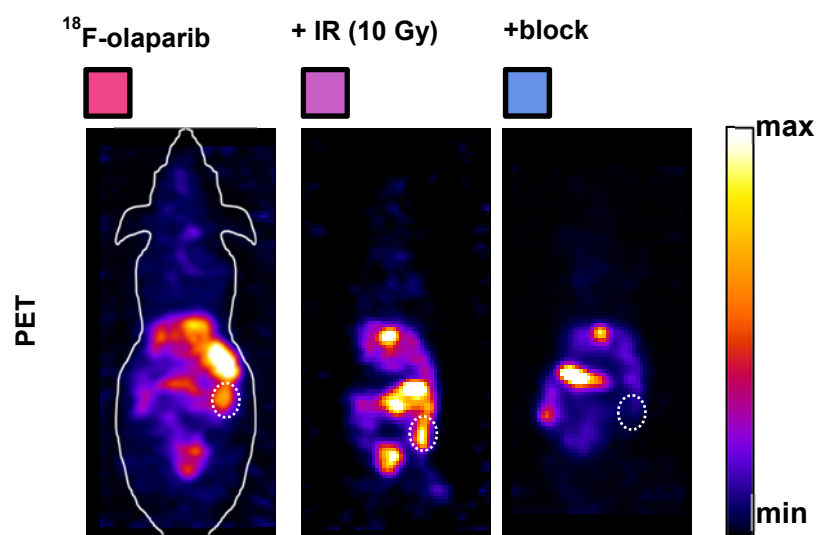


blocked

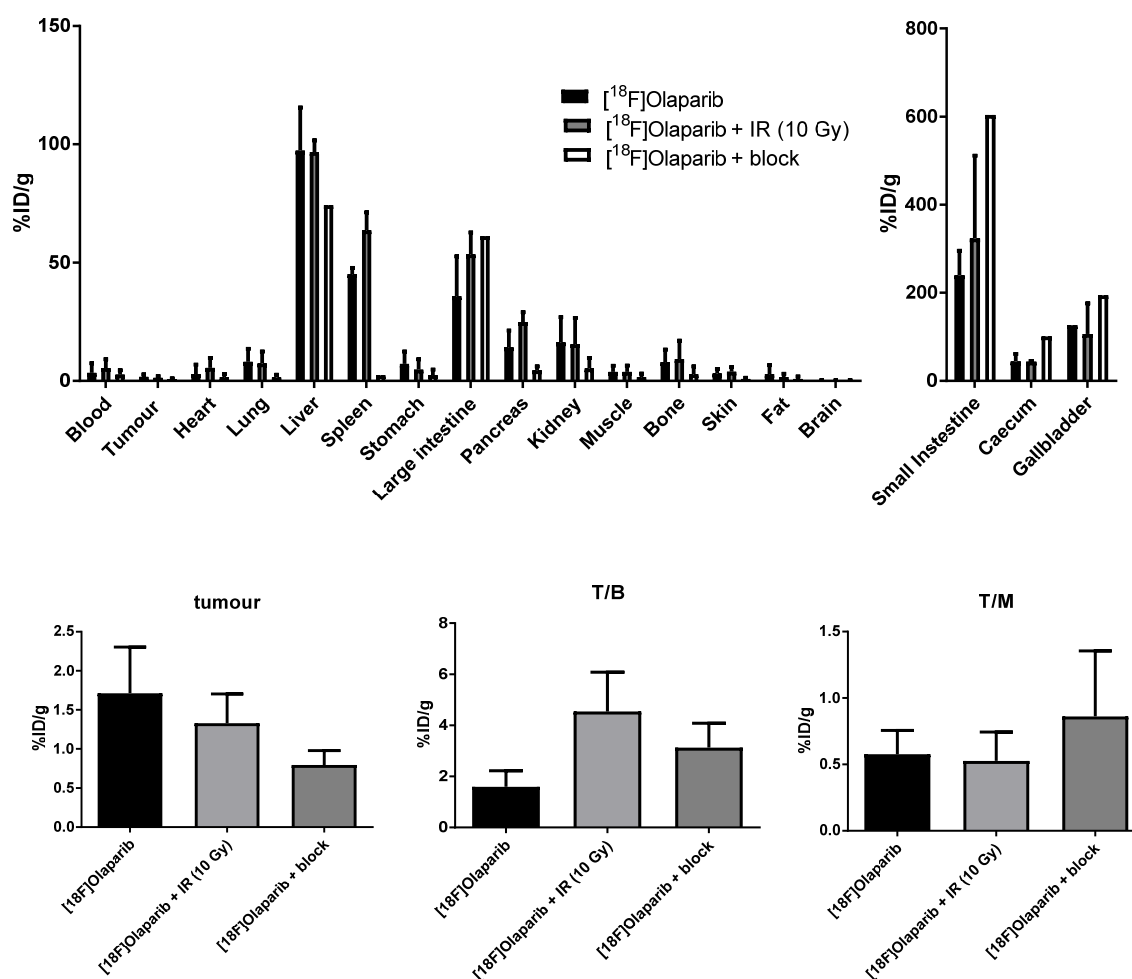
B



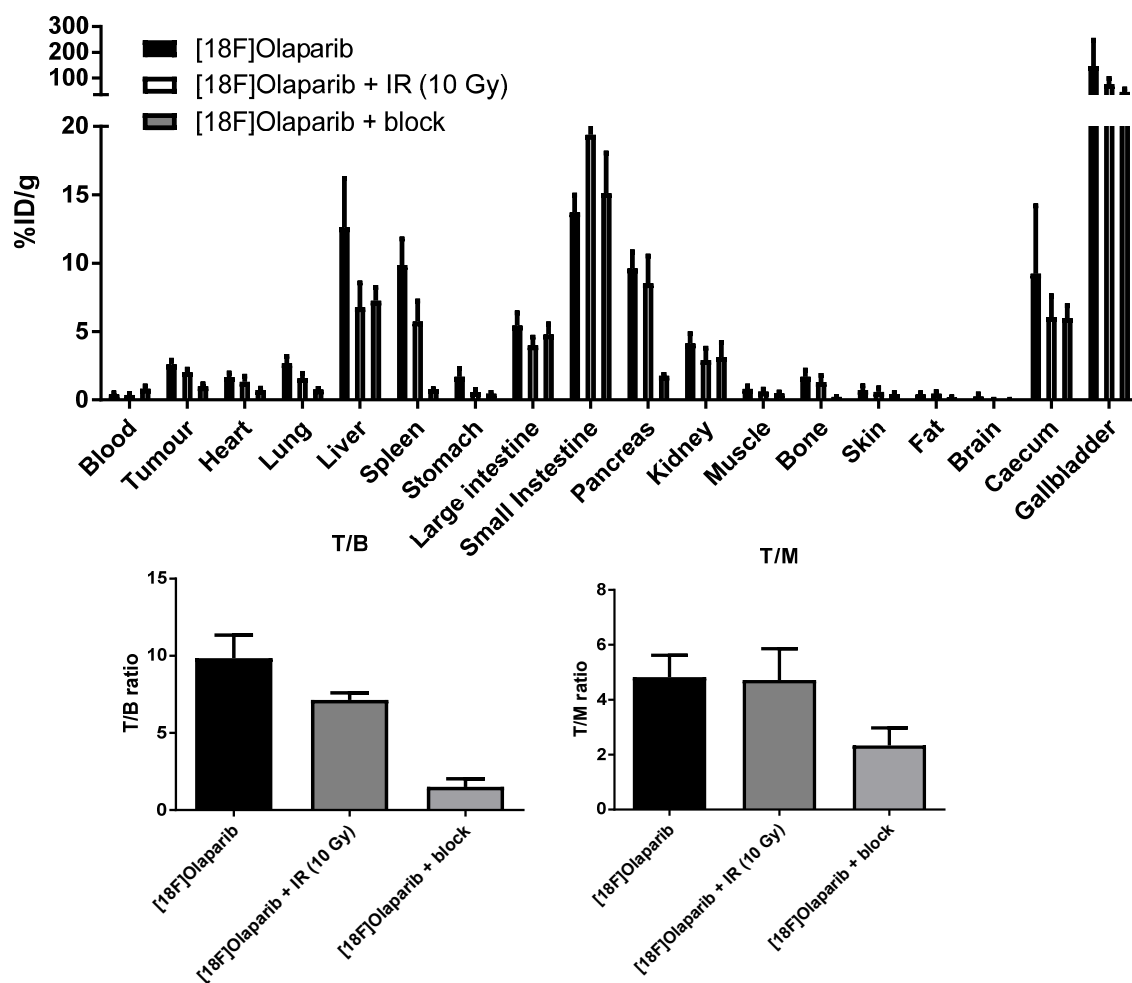
C



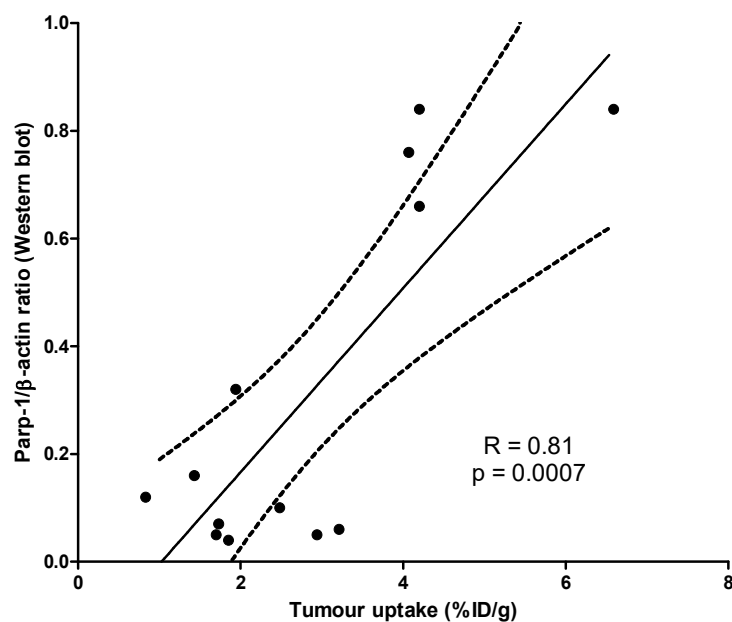
Supplemental Fig 13: (A) Representative dynamic PET images after intravenous bolus injection of [^{18}F]olaparib in PSN-1 tumor-bearing mice. Images are presented as coronal Maximum Intensity Projections, representing the same animals and using the same color scale as in Figure 5. (B) Image quantification of A. (C) Maximum intensity projections of the same animals, using the same color scale. Dashed circles indicate the position of the xenograft tumor.



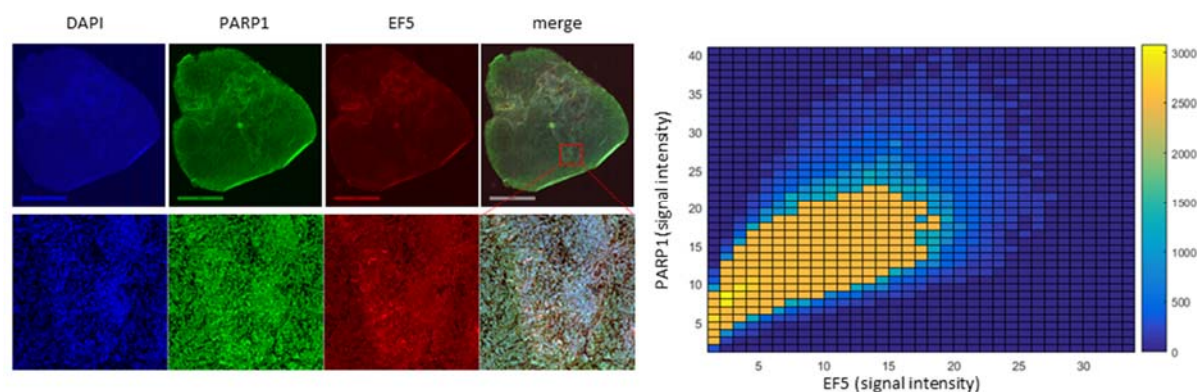
Supplemental Fig 14: Ex vivo biodistribution of ^{18}F -olaparib in CaNT tumor-bearing mice, 1 h after intravenous injection.



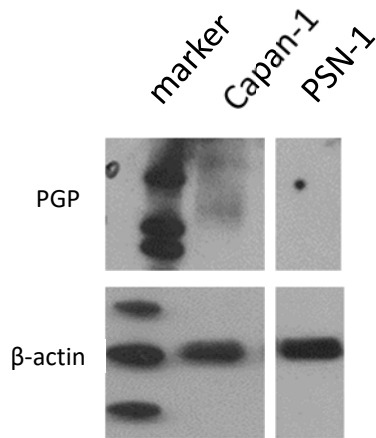
Supplemental Fig 15: Ex vivo biodistribution of ^{18}F -olaparib in Capan-1 tumor-bearing mice, 1 h after intravenous injection.



Supplemental Fig 16: Correlation of tumor uptake determined by ex vivo biodistribution and PARP-1 expression measure via Western blot



Supplemental Fig 17: Representative section from a naive PSN-1 xenograft tumor, stained for PARP-1 and EF5, including a representative high-resolution detail, and a cytofluorogram comparing PARP-1 versus EF5 signal intensity in the high-resolution image.



Supplemental Fig 18: PGP pump expression in the cell lines used in this study.

REFERENCES for supplemental material

1. Pangborn AB, Giardello MA, Grubbs RH, Rosen RK, Timmers FJ. Safe and convenient procedure for solvent purification. *Organometallics*. 1996;15:1518-1520.
2. Menear KA, Adcock C, Boulter R, et al. 4-[3-(4-cyclopropanecarbonylpiperazine-1-carbonyl)-4-fluorobenzyl]-2H-phthalazin-1-one: a novel bioavailable inhibitor of poly(ADP-ribose) polymerase-1. *J Med Chem*. 2008;51:6581-6591.
3. Ravat P, Borozdina Y, Ito Y, Enkelmann V, Baumgarten M. Crystal Engineering of Tolane Bridged Nitronyl Nitroxide Biradicals: Candidates for Quantum Magnets. *Cryst Growth Des*. 2014;14:5840-5846.
4. Outerbridge VM, Landge SM, Tamaki H, Török B. Microwave-Promoted Solid-Acid Catalyzed One-Pot Synthesis of Phthalazinones. *Synthesis*. 2009;11:1801-1806.
5. Nezhawy AOH, Gaballah ST, Radwan MAA. Studying the reactivity of (phthalazin-1(2H)-on-2-yl)methyl trichloroacetimidate towards different C- and O-nucleophiles. *Tetrahedron Letters*. 2009;50:6646-6650.
6. Tredwell M, Preshlock SM, Taylor NJ, et al. A general copper-mediated nucleophilic ^{18}F fluorination of arenes. *Angew Chem Int Ed Engl*. 2014;53:7751-7755.
7. Taylor NJ, Emer E, Preshlock S, et al. Derisking the Cu-Mediated ^{18}F -Fluorination of Heterocyclic Positron Emission Tomography Radioligands. *J Am Chem Soc*. 2017;139:8267-8276.
8. Cornelissen B, Hu M, McLarty K, Costantini D, Reilly RM. Cellular penetration and nuclear importation properties of ^{111}In -labeled and ^{123}I -labeled HIV-1 tat peptide immunoconjugates in BT-474 human breast cancer cells. *Nucl Med Biol*. 2007;34:37-46.
9. Thurber GM, Reiner T, Yang KS, Kohler RH, Weissleder R. Effect of small-molecule modification on single-cell pharmacokinetics of PARP inhibitors. *Mol Cancer Ther*. 2014;13:986-995.
10. Reiner T, Lacy J, Keliher EJ, et al. Imaging therapeutic PARP inhibition in vivo through bioorthogonally developed companion imaging agents. *Neoplasia*. 2012;14:169-177.
11. Kersemans V, Cornelissen B, Hueting R, et al. Hypoxia imaging using PET and SPECT: the effects of anesthetic and carrier gas on $[\text{Cu}]$ -ATSM, $[\text{Tc}]$ -HL91 and $[\text{F}]$ -FMISO tumor hypoxia accumulation. *PLoS One*. 2011;6:e25911.

- 12.** Koch CJ. <http://www.hypoxia-imaging.org/v2/methods/ef5manual.htm>. Accessed 21/01/2011, 2011.
- 13.** Lee J, Siemann DW, Koch CJ, Lord EM. Direct relationship between radiobiological hypoxia in tumors and monoclonal antibody detection of EF5 cellular adducts. *Int J Cancer*. 1996;67:372-378.
- 14.** Hueting R, Kersemans V, Cornelissen B, et al. A comparison of the behavior of ^{64}Cu -acetate and ^{64}Cu -ATSM in vitro and in vivo. *J Nucl Med*. 2014;55:128-134.



The Journal of
NUCLEAR MEDICINE

PET imaging of PARP expression using [^{18}F]olaparib

Thomas Wilson, Mary-Ann Xavier, James Knight, Stefan Verhoog, Julia Baguña Torres, Michael Mosley, Samantha Hopkins, Sheena Wallington, Danny Allen, Veerle Kersemans, Rebekka Hueting, Sean Smart, Veronique Gouverneur and Bart Cornelissen

J Nucl Med.

Published online: November 2, 2018.

Doi: 10.2967/jnumed.118.213223

This article and updated information are available at:

<http://jnm.snmjournals.org/content/early/2018/11/01/jnumed.118.213223>

Information about reproducing figures, tables, or other portions of this article can be found online at:

<http://jnm.snmjournals.org/site/misc/permission.xhtml>


Information about subscriptions to JNM can be found at:

<http://jnm.snmjournals.org/site/subscriptions/online.xhtml>

JNM ahead of print articles have been peer reviewed and accepted for publication in *JNM*. They have not been copyedited, nor have they appeared in a print or online issue of the journal. Once the accepted manuscripts appear in the *JNM* ahead of print area, they will be prepared for print and online publication, which includes copyediting, typesetting, proofreading, and author review. This process may lead to differences between the accepted version of the manuscript and the final, published version.

The Journal of Nuclear Medicine is published monthly.
SNMMI | Society of Nuclear Medicine and Molecular Imaging
1850 Samuel Morse Drive, Reston, VA 20190.
(Print ISSN: 0161-5505, Online ISSN: 2159-662X)

© Copyright 2018 SNMMI; all rights reserved.

 SOCIETY OF
NUCLEAR MEDICINE
AND MOLECULAR IMAGING